

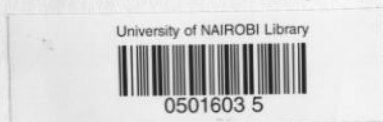
Fabrication and Characterization of $\text{In}(\text{OH})_x\text{S}_y$ Modified Highly Structured $\text{TiO}_2/\text{Pb}(\text{OH})_x\text{S}_y/\text{PEDOT:PSS}$ eta Solar Cell, and Study of its Transport Mechanisms.

Robinson Juma Musembi B.Sc (Nairobi), M.Sc (Nairobi)

Prof. Bernard O. Aduda

Department of Physics, University of Nairobi, Kenya

A thesis submitted in fulfillment of the requirements for the degree of Doctor of Philosophy (Physics) of the University of Nairobi



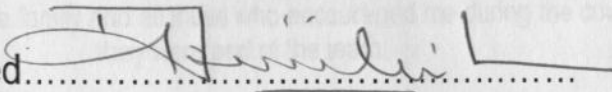
Department of Physics, University of Nairobi

September, 2009

UNIVERSITY OF NAIROBI
LIBRARY

Declaration

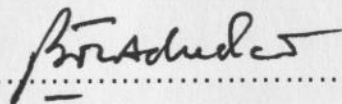
This Thesis is my own work and has not been examined or submitted for examination in any other University

Signed.....

Musembi, Robinson Juma: Reg. No. 180/8695/2005

Dated..... 01/09/2009.....

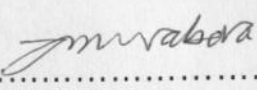
This thesis has been submitted for examination with our approval as supervisors

Signed: Supervisor.....

Prof. Bernard O. Aduda

Department of Physics, University of Nairobi, Kenya

Dated... 7/9/2009.....

Signed: Supervisor.....

Dr. Julius M. Mwabora

Department of Physics, University of Nairobi, Kenya

Dated..... 01/09/2009.....

Acknowledgments

I am grateful to my supervisors Prof. Bernard O. Aduda and Dr. Julius Mwabora for their guidance and patience in the course of doing this work. I also wish to acknowledge my supervisors at Hermoltz – Zentrum Berlin für Materialien und Energie, Lise Meitner Campus, Solarenergieforschung (formerly Hahn Meitner Institute), Dr. Thomas Dittrich and Dr. Konstantinos Fostiropoulos for their guidance in research work and for accepting me to work in eta and organic solar cells groups, respectively. Gratefully acknowledged are discussions by: Dr. Eng. Reiner Klenk in the area of series and shunt resistance, Dr. Marin Rusu for research and discussions in transport mechanisms, Dr. Maria del Rocio Cabenza of CIEMAT for training me in chemical bath deposition and characterization of solar cells, Dr. Abdelhalk Belaidi for discussions in solar cells characterizations and scanning electron microscopy of various thin films, Dr. Marcus Bär for discussions and analysis in X-ray photoelectron spectroscopy (XPS) and X-ray Auger electron spectroscopy (XAES), Ms Sieber for making cross-sectional SEM and energy dispersive X-ray (EDX) mapping of the eta solar cell. Greatly thanked are participants in the entire heterogeneous materials group SE2 for organizing many presentations through FH Runde, these discussions made this work rich in ideas. The overall department SE2 leader Prof. Dr. Martha Christina Lux-Steiner is thanked for accepting me to work in eta and organic materials research groups, and accepting to grant me financial aid through the Institute.

The following institutions are gratefully acknowledged: The University of Nairobi for tuition waiver, job opportunity while studying, financial aid in form of return air ticket, Nairobi – Berlin – Nairobi, and also for providing opportunity to do the research work. International Programmes in Physical Sciences (IPPS), through Uppsalla University, Sweden, for financial aid during the research work. Deutscher Akademischer Austauschdienst (DAAD), i.e. Germany Academic Exchange Service; for financing exchange programme between University of Nairobi and Free University, Berlin Germany and in-country partial scholarship. Bundes Ministerium für Bildung und Forschung (Ministry of Education and Research of Federal Republic of Germany) is thanked for providing one year scholarship at Hahn Meitner Institute.

Members of the Condensed Matter Research Group (University of Nairobi), eta group and organic materials research group (Hermoltz – Zentrum Berlin für Materialien und Energie, Lise Meitner Campus, Solarenergieforschung) are acknowledged for useful discussions during numerous group meetings, brewed coffee and sweet cakes, sometimes ciabatas and the warm friendship they provided were key to success of this work.

Abstract

An highly structured $\text{SnO}_2\text{:F/TiO}_2\text{/In(OH)}_x\text{S}_y\text{/Pb(OH)}_x\text{S}_y\text{/PEDOT:PSS/Au}$ eta solar cell based on the dye sensitized solar cell device concept, has been developed and investigated using various techniques. In this device, fluorine doped tin oxide coated glass ($\text{SnO}_2\text{:F}$) has been used as the substrate material, TiO_2 and PEDOT:PSS serves as the wide band gap n- and p- type electron and hole conductors, respectively, $\text{In(OH)}_x\text{S}_y$ is used as the buffer layer, while $\text{Pb(OH)}_x\text{S}_y$ together with the buffer layer provides a good interface for light photon absorption. The back contact of the solar cell is Au, while the front contact is provided by $\text{SnO}_2\text{:F}$ coating on the substrate. Other devices with simplified structures for photovoltaic application have also been fabricated. The thin film layers of TiO_2 , $\text{In(OH)}_x\text{S}_y$, and $\text{Pb(OH)}_x\text{S}_y$ have been characterized by surface photovoltage spectroscopy (SPV), X-ray photo- and Auger- electron spectroscopy (XPS, XAES), scanning electron spectroscopy (SEM), and energy dispersive X-ray spectroscopy (EDX) mapping.

The $\text{In(OH)}_x\text{S}_y$ modified eta solar cell and the devices with simplified architecture were analysed at room temperature by J – U characterization and the following values were recorded:

$\text{SnO}_2\text{:F/TiO}_2\text{/In(OH)}_x\text{S}_y\text{/Pb(OH)}_x\text{S}_y\text{/PEDOT:PSS/Au}$ ($J_{sc} = 7.4 \text{ mA/cm}^2$, $U_{oc} = 281 \text{ mV}$, $FF = 0.40$, $\eta = 0.83\%$), $\text{SnO}_2\text{:F/In(OH)}_x\text{S}_y\text{/Pb(OH)}_x\text{S}_y\text{/PEDOT:PSS/Au}$ ($J_{sc} = 4.95 \text{ mA/cm}^2$, $U_{oc} = 314 \text{ mV}$, $FF = 0.40$, $\eta = 0.61\%$), $\text{SnO}_2\text{:F/TiO}_2\text{/In(OH)}_x\text{S}_y\text{/Pb(OH)}_x\text{S}_y\text{/Au}$ ($J_{sc} = 6.16 \text{ mA/cm}^2$, $U_{oc} = 344 \text{ mV}$, $FF = 0.44$, $\eta = 0.94\%$), $\text{SnO}_2\text{:F/In(OH)}_x\text{S}_y\text{/Pb(OH)}_x\text{S}_y\text{/Au}$ ($J_{sc} = 5.33 \text{ mA/cm}^2$, $U_{oc} = 297 \text{ mV}$, $FF = 0.41$, $\eta = 0.65\%$). Light soaking has been found to improve photovoltaic parameters of eta solar cell and those of devices with reduced number of layers. The conversion efficiency and short circuit current density have been found to increase with light soaking duration by a factor of about 1.6 – 2.7 and 2.1 – 3, respectively. Different layer materials have been found to play different roles, TiO_2 has been found to improve the photoelectrical properties of the solar cell, $\text{In(OH)}_x\text{S}_y$ has been found to act as recombination barrier and also it forms good interface with $\text{In(OH)}_x\text{S}_y\text{/Pb(OH)}_x\text{S}_y$ making it possible for the solar cell to function, while PEDOT:PSS serves as the protective layer of the $\text{Pb(OH)}_x\text{S}_y$ against photo-degradation and diffusion of Au back contact atoms into the bulk of the solar cell structure which shunts the device.

Furthermore, current transport mechanisms studies of the highly structured eta solar cell have also been carried out by intensity and temperature dependent JU – T characterization method. The solar cell has been characterized in the temperature range of 200 – 320 K at illumination intensities ranging from 0.05

mW/cm² to 100 mW/cm². The diode ideality factor under illumination has been found to vary between $1.2 \leq A \leq 1.6$, whereas in the dark it was found to be between $6.9 \leq A \leq 10.1$. The eta solar cell has been found to undergo thermally activated recombination when under illumination, while tunneling enhanced recombination dominates the current when the solar cell is in the dark. The solar cell conversion efficiency has been found to show logarithmic dependence on illumination intensity in the temperature range investigated achieving its maximum at 45 mW/cm². Lastly, series resistance of the device has been found to decrease with increasing temperature, this behaviour has been attributed to the number of available charge carriers due to the effect of thermally activated recombination process.

Table of Contents

List of Symbols

List of Abbreviations

List of Figures

List of Tables

1	CHAPTER 1: Introduction	1
1.1	Introduction	1
1.2	Statement of the problem	2
1.3	Significance of the study	3
1.4	Objectives of this work	5
1.5	Thesis structure	5
2	CHAPTER 2: Literature Review	6
2.1	Introduction	6
2.2	Substrate silicon types for eta solar cells	7
2.3	Absorber materials for eta solar cells	8
2.4	Recombination barrier, the buffer or tunneling layer	9
2.5	Eta solar cells a review	10
3	CHAPTER 3: Theory	15
3.1	Photovoltaic solar cell	15
3.1.1	Ideal solar cell	15
3.1.2	Non-ideal solar cell	19
3.2	Transport mechanism theory	22
3.3	Quantum efficiency	27

Table of Contents

List of Content	Page
Declaration	i
Dedications	ii
Acknowledgements	iii
Abstract	iv
Table of Contents	vi
List of Symbols	ix
List of Abbreviations	xi
List of Figures	xiii
List of Tables	xviii
1. CHAPTER 1: Introduction	1
1.1. Introduction	1
1.2. Statement of the problem	3
1.3. Significance of the study	4
1.4. Objectives of this work	5
1.5. Thesis structure	5
2. CHATER 2: Literature Review	6
2.1. Introduction	6
2.2. Substrate window layer for eta solar cells	7
2.3. Absorber materials for eta solar cells	8
2.4. Recombination barrier, the buffer or tunneling layer	9
2.5. Eta solar cells a review	10
3. CHAPTER 3: Theory	15
3.1. Photovoltaic solar cell	15
3.1.1. Ideal solar cell	15
3.1.2. Non ideal solar cell	19
3.2. Transport mechanism theory	22
3.3. Quantum efficiency	27

4. CHAPTER 4: Experimental Procedures	29
4.1. Introduction	29
4.2. Samples preparation	29
4.2.1. Titanium dioxide (TiO ₂)	30
4.2.2. Indium hydroxy sulphide (In(OH) _x S _y)	32
4.2.3. Lead hydroxy sulphide (Pb(OH) _x S _y)	33
4.2.4. Poly(3,4-ethylenedioxythiophene) polystyrene sulfonate (PEDOT:PSS)	34
4.2.5. Front and back contacts of the solar cell	35
4.3. Characterization of the thin films	35
4.3.1. Surface photovoltage (SPV) spectroscopy	36
4.3.2. Scanning electron microscopy (SEM)	37
4.3.3. Energy dispersive X-ray (EDX) spectroscopy	38
4.3.4. X-ray photoelectron spectroscopy (XPS) and X-ray Auger electron spectroscopy (XAES)	38
4.3.5. Optical transmittance and reflectance	38
4.4. Characterization of the solar cell	39
4.4.1. Room temperature current – voltage (J – U) characterization	39
4.4.2. Intensity and temperature dependent current – voltage (JU - T) characterization	40
4.4.3. External quantum efficiency (EQE)	41
5. CHAPTER 5: Results and Discussions	43
5.1. Introduction	43
5.2. Thin films characteristics	43
5.2.1. Surface morphology of titanium dioxide (TiO ₂)	43
5.2.2. Surface morphology of Indium hydroxy sulfide (In(OH) _x S _y)	46
5.2.3. Surface morphology of lead hydroxy sulfide (Pb(OH) _x S _y)	49
5.2.4. Poly(3,4 ethylenedioxythiophene) doped with polystyrene sulfonic acid	50
5.2.5. Stoichiometry of lead hydroxy sulphide (Pb(OH) _x S _y)	51
5.2.6. Surface photovoltage spectroscopy (SPV) analysis	54
5.2.7. Band gap (E _g) and exponential tail state (E _t) energy analysis	56
5.2.8. Band gap optimization of the buffer layer	58
5.2.9. Effect of annealing In(OH) _x S _y thin film	60
5.2.10. Effect of In(OH) _x S _y layer thickness	62
5.3. Characterization of the eta solar cell	64
5.3.1. SnO ₂ :F/TiO ₂ /Au device characteristic	64
5.3.2. ETA solar cell device, SnO ₂ :F/TiO ₂ /Pb(OH) _x S _y /PEDOT:PSS/Au	65
5.3.3. Effect of In(OH) _x S _y buffer layer on ETA solar cell device	67
5.3.4. Structural analysis of eta solar cell	71
5.3.5. Effect of thickness of various layers on the device performance	74
5.3.6. The role of component materials in the eta solar cell heterostructure	77
5.3.6.1. J-U characteristics of SnO ₂ :F/TiO ₂ /In(OH) _x S _y /Pb(OH) _x S _y /Au device	77

5.3.6.2.	J-U characteristics of SnO ₂ :F/In(OH) _x S _y /Pb(OH) _x S _y /PEDOT:PSS/Au	78
5.3.6.3.	J-U characteristics of SnO ₂ :F/In(OH) _x S _y /Pb(OH) _x S _y /Au device	80
5.4.	Effects of light soaking on eta solar cell	82
5.4.1.	SnO ₂ :F/TiO ₂ /In(OH) _x S _y /Pb(OH) _x S _y /PEDOT:PSS/Au performance	82
5.4.2.	SnO ₂ :F/In(OH) _x S _y /Pb(OH) _x S _y /PEDOT:PSS/Au performance	84
5.4.3.	SnO ₂ :F/TiO ₂ /In(OH) _x S _y /Pb(OH) _x S _y /Au performance	85
5.4.4.	SnO ₂ :F/In(OH) _x S _y /Pb(OH) _x S _y /Au performance	85
5.4.5.	Degradation study of SnO ₂ :F/In(OH) _x S _y /Pb(OH) _x S _y /PEDOT:PSS/Au device	87
5.5.	JU-T characterization of eta solar cell	89
5.5.1.	Intensity dependency characterization	90
5.5.2.	Temperature dependency characterization	93
5.5.3.	Transport mechanism of eta solar cell	95
5.5.4.	Temperature dependency of series resistance R _s	100
6.	CHAPTER 6: Conclusion and suggestions for further work	102
6.1.	Conclusions	102
6.2.	Suggestions for further work	104
7.	References	106
8.	Appendix	116

List of Symbols

A	area
A_i	ideality factor
D_h	hole diffusion coefficient
D_e	electron diffusion coefficient
E_{CB}	conduction band energy
eV	electron volt
E_{VB}	valence band energy
E_g	band gap energy
E_t	tail state energy below the band gap
h	Planck's constant
I_d	current through the diode
I_{ph}	photon generated current
J_h	hole current density
J_{dark}	current density measured in the dark
J_e	electron current density
J_{light}	current density measured under illumination
J_o	reverse saturation current density
J_{oo}	temperature dependent prefactor
J_{ph}	photocurrent density
J_{sc}	short circuit current density
L_h	holes diffusion length
L_e	electron diffusion length
N_a	concentration of acceptor
N_d	concentration of donors
S_n	interface recombination for electrons
S_p	interface recombination for holes
U_a	applied voltage
U_{bi}	built in voltage
U_{oc}	open circuit voltage

n_n	majority carrier density for electrons
p_p	majority carrier density for holes
K	degree Kelvin
R_s	series resistance
R_{sh}	shunt resistance (parallel resistance)
T	temperature
J	current density
U	voltage
k	Boltzmann constant
n	electron carrier density
p	hole carrier density
q	Symbol of elementary charge
ν	frequency
μ_h	hole mobilities
μ_e	electron mobility
τ_h	hole lifetime
τ_e	electron lifetime
λ	wavelength
ξ	electric field

List of abbreviations

Al_2O_3	aluminum oxide
Au	gold
CBD	chemical bath deposition
CdS	cadmium sulphide
CdTe	cadmium telluride
CPD	contact potential difference
CuInS_2	copper indium disulphide
cm	centimeter
Eff	Efficiency
EQE	external quantum efficiency
ERDA	elastic recoil detection and analysis
eta	extremely thin absorber
FF	Fill factor
hrs	hours
HOMO	highest occupied molecular orbital
ILGAR	ion layer gas reaction and absorption
$\text{In(OH)}_x\text{S}_y$	indium hydroxyl sulphide
mA	milliampere
MgO	magnesium oxide
mV	millivolt
mW	milliwatt
nm	nanometer
$\text{Pb(OH)}_x\text{S}_y$	lead hydroxyl sulphide
PEDOT	poly(3,4-ethylenedioxythiophene)
PSS	polystyrene sulfonate
SCR	space charge region
SEM	scanning electron microscopy
SILAR	successive ion layer absorption and reaction
$\text{SnO}_2\text{:F}$	fluorine doped tin oxide

SPV	surface photovoltage
TiO ₂	titanium dioxide
XAES	X-ray auger electron spectroscopy
XPS	X-ray photoelectron spectroscopy
ZnO	Zinc oxide
ZrO ₂	Zirconium dioxide
μm	micrometer

Figure 3.1	Downward band structure of cadmium telluride (CdTe) thin film (Kobayashi et al., 2001)
Figure 3.2	Energy band diagram of a p-n junction of two semiconductors at equilibrium. E_g is the band gap, E_c is the conduction band, E_v is the valence band, E_f is the Fermi level energy, E_{f0} is the built-in voltage.
Figure 3.3	I-V characteristics for a solar cell in the dark and under illumination.
Figure 3.4	Equivalent circuit for non-ideal single diode solar cell. I_0 is the current through the diode, I_{ph} is current generated due to energy transfer of the light photons $E = h\nu$, U_m and I_m are the measured voltage and current, respectively.
Figure 3.5	Semi-logarithmic plot (dark current density (mA/cm ²)) of the dark current as function of applied voltage U (V/cm).
Figure 3.6	Band diagram of the proposed CdTe solar cell studied in this work. Shown are the main recombination mechanisms occurring in depletion and space charge region (SCR).
Figure 3.7	Quantum yield plot as a function of temperature. Extrapolation used in calculating activation energy is also shown where it is the plot of equation 3.25.
Figure 3.8	Typical J-V plot of external quantum efficiency performance of a solar cell operated at AM1.5.
Figure 4.1	Etch solar cell structure fabricated in this work showing stacked thin film layers.
Figure 4.2	Etch process chamber used in fabricating TiO ₂ nanorods. Shown are the precursor container, microwave heater, manifold source and substrate holder with a heater.
Figure 4.3	Etch process chamber used in depositing In(OH) ₃ , Sn, and Pb(OH) ₂ , respectively.
Figure 4.4	Micrograph of the etch process for coating samples, the 4 steps represents one cycle.
Figure 4.5	Etch process chamber along the top part of the vacuum coating system used in depositing front window layers.
Figure 4.6	Photograph of the detection section of the surface photovoltage spectroscopy setup used for characterizing samples, and let state energy below the band gap.
Figure 4.7	Block diagram of the current-voltage characterization set up.

List of Figures

- Figure 2.1:** Scanning electron micrograph of columnar zinc oxide (ZnO) thin film (Könenkamp, *et al.*, 2002).
- Figure 3.1:** Semiconductor energy band diagram showing: (A) intrinsic semiconductor, (B) n - type semiconductor, and (C) p - type semiconductor.
- Figure 3.2:** Band diagram of a p - n junction of two asymmetrically doped semiconductors at equilibrium. E_{VB} , E_{CB} and E_F , describe valence band, conduction band and Fermi level energy respectively and U_{bi} is the built-in voltage.
- Figure 3.3:** J - U characteristics for a solar cell in the dark and under illumination.
- Figure 3.4:** Equivalent circuit for non - ideal single diode solar cell, I_d is the current through the diode; I_{ph} is current generated due to energy transfer of the light photons $E = h\nu$. U_m and I_m are the measured voltage and current, respectively.
- Figure 3.5:** Semi logarithmic plot of current density (mW/cm^2) of the dark current as function of applied voltage U (volts).
- Figure 3.6:** Band diagram of the proposed eta solar cell studied in this work. Shown are the main recombination mechanism locations for interface and space charge region (SCR).
- Figure 3.7:** Open circuit plot as a function of temperature. Extrapolation used in calculating activation energy is also shown, where H is the plot of equation 3.26.
- Figure 3.8:** Typical diagram of external quantum efficiency performance of a solar cell operated at AM1.5.
- Figure 4.1:** Eta solar cell structure fabricated in this work showing stalked thin film layers
- Figure 4.2:** Spray pyrolysis system used in fabricating TiO_2 samples. Shown are the precursor container, rubberband heater, humidity source and substrate holder with a heater.
- Figure 4.3:** Set up for chemical bath deposition used in depositing $In(OH)_xS_y$ and $Pb(OH)_xS_y$, respectively.
- Figure 4.4:** Illustration of SILAR technique for coating samples; the 4 steps represents one cycle.
- Figure 4.5:** Block diagram showing the top part of the vacuum coating system used in depositing front and back contact.
- Figure 4.6:** The samples' measurement section of the surface photovoltage spectroscopy setup used for determining band gap and tail state energy below the band gap.
- Figure 4.7:** Block diagram of the current - voltage characterization set up.

- Figure 4.8:** External quantum efficiency (EQE) set up used in characterizing the solar cells.
- Figure 5.1:** Scanning electron micrograph of TiO_2 deposited by spray pyrolysis, magnified at $\times 30,000$. The arrows show the TiO_2 coating and the micrometer (μm) sized pores.
- Figure 5.2:** Scanning electron micrograph of spray pyrolysis deposited TiO_2 magnified at $\times 10,000$. The arrows points at the compact layer in contact with $\text{SnO}_2:\text{F}$ coating on glass (Belaidi, 2004).
- Figure 5.3:** Scanning electron micrograph of commercial sol-gel deposited TiO_2 magnified at $\times 60,000$. Deposition was done at Sg - Lux GmbH, Berlin, Germany, (Sg - Lux, 2003).
- Figure 5.4:** Scanning electron micrograph of sol-gel deposited compact TiO_2 magnified at $\times 200,000$. The arrows points at TiO_2 compact thin film coating and glass substrate. The $\text{SnO}_2:\text{F}$ coating between TiO_2 and glass is not clearly discernable.
- Figure 5.5:** Scanning electron micrograph for as deposited CBD- $\text{In}(\text{OH})_x\text{S}_y$ and magnified at $\times 100,000$, arrow shows typical cluster of $\text{In}(\text{OH})_x\text{S}_y$ for a sample deposited on TiO_2 coated substrate in one cycle.
- Figure 5.6:** Scanning electron micrograph for as deposited CBD- $\text{In}(\text{OH})_x\text{S}_y$ and magnified at $\times 100,000$. The sample was deposited on TiO_2 coated glass substrate in three cycles. Arrow A shows spherical growth while B points at linear growth.
- Figure 5.7:** Scanning electrom micrograph of CBD - $\text{In}(\text{OH})_x\text{S}_y$ thin film magnified at $\times 100,000$. The arrows show the compact layer growth.
- Figure 5.8:** Scanning electron micrograph for CBD - lead hydroxy sulphide deposited on TiO_2 magnified at 30,000. The arrows points at TiO_2 porous matrix and typical $\text{Pb}(\text{OH})_x\text{S}_y$ clusters.
- Figure 5.9:** Chemical structure of poly(3,4-ethylenedioxythiophene) doped with polystyrene sulfonic acid (PEDOT:PSS).
- Figure 5.10:** X-ray photoelectron and X-ray Auger electron survey spectra's for two samples of the type (a) $\text{In}(\text{OH})_x\text{S}_y/\text{SnO}_2:\text{F}/\text{glass}$, and (b) $\text{Pb}(\text{OH})_x\text{S}_y/\text{In}(\text{OH})_x\text{S}_y/\text{SnO}_2:\text{F}/\text{glass}$ substrate.
- Figure 5.11:** X-ray photoelectron and X-ray induced Auger electron spectroscopies for $\text{Pb}(\text{OH})_x\text{S}_y/\text{In}(\text{OH})_x\text{S}_y/\text{SnO}_2:\text{F}$ sample excited with (a) Pb NOO (b) Pb $4f_{7/2}$ (b) and O 1s Auger signals from Mg K_α source.
- Figure 5.12:** Surface photovoltage spectroscopy for different multilayered samples, (a) $\text{TiO}_2/\text{In}(\text{OH})_x\text{S}_y$, (b) $\text{TiO}_2/\text{Pb}(\text{OH})_x\text{S}_y$ and (c) $\text{TiO}_2/\text{In}(\text{OH})_x\text{S}_y/\text{Pb}(\text{OH})_x\text{S}_y$, the filled circles depict the in-phase component while the unfilled circles show the 90 phase shifted signal.

- Figure 5.13:** Surface photovoltage spectroscopy amplitude for $\text{Pb(OH)}_x\text{S}_y$ prepared of $\text{In(OH)}_x\text{S}_y$ (filled triangles) and TiO_2 (open triangles), $\text{In(OH)}_x\text{S}_y$ as prepared (unfilled circles) and annealed sample (filled circles) and TiO_2 (squares).
- Figure 5.14:** Optical transmittance of as prepared $\text{In(OH)}_x\text{S}_y$ (not annealed) and $\text{In(OH)}_x\text{S}_y$ annealed in argon atmosphere for 30 minutes at 300 °C.
- Figure 5.15:** Surface photovoltage spectroscopy measurements for $\text{In(OH)}_x\text{S}_y$ deposited at different pH values.
- Figure 5.16:** Derived E_g as a function of pH value of $\text{In(OH)}_x\text{S}_y$ SPV analysis shown in figure 5.15. The question marks depict the likely $\text{In(OH)}_x\text{S}_y$ phase in either of the sections.
- Figure 5.17:** Influence of temperature on $\text{In(OH)}_x\text{S}_y$ annealed in argon atmosphere at different temperature levels (100 °C - 500 °C). SPV measurements were done after annealing the sample at the temperatures shown, after each measurement the sample was annealed at higher temperature.
- Figure 5.18:** Surface photovoltage spectroscopy analysis of $\text{In(OH)}_x\text{S}_y$ thin film of different thicknesses depending on the number of dips in the chemical bath solution.
- Figure 5.19:** Structure of the Schottky diode type of device used for testing rectification of TiO_2 .
- Figure 5.20:** Rectification characteristics of $\text{SnO}_2\text{:F/TiO}_2\text{/Au}$ Schottky diode type of device
- Figure 5.21:** Initial eta solar cell proposed in this work, n- type material is TiO_2 , p- type material is PEDOT:PSS and the absorber material is $\text{Pb(OH)}_x\text{S}_y$.
- Figure 5.22:** J - U characteristics for $\text{SnO}_2\text{:F/TiO}_2\text{/Pb(OH)}_x\text{S}_y\text{/PEDOT:PSS/Au}$, eta solar cell under illumination and in the dark.
- Figure 5.23:** Modified eta solar cell structure, $\text{In(OH)}_x\text{S}_y$ has been used as a buffer layer at the TiO_2 and $\text{Pb(OH)}_x\text{S}_y$ interface.
- Figure 5.24:** J - U characteristics for $\text{SnO}_2\text{:F/TiO}_2\text{/In(OH)}_x\text{S}_y\text{/Pb(OH)}_x\text{S}_y\text{/PEDOT:PSS/Au}$, eta solar cell with as-prepared $\text{In(OH)}_x\text{S}_y$ as a buffer layer.
- Figure 5.25:** J - U characteristics for $\text{SnO}_2\text{:F/TiO}_2\text{/In(OH)}_x\text{S}_y\text{/Pb(OH)}_x\text{S}_y\text{/PEDOT:PSS/Au}$, eta solar cell with annealed $\text{In(OH)}_x\text{S}_y$ buffer layer giving the best conversion efficiency.
- Figure 5.26:** External quantum efficiency (EQE) performance for $\text{SnO}_2\text{:F/TiO}_2\text{/In(OH)}_x\text{S}_y\text{/Pb(OH)}_x\text{S}_y\text{/Au}$ eta solar cell measured from 350 nm to 900 nm. Inset is the calculated J_{sc} value.
- Figure 5.27:** Statistics of 89 solar cells, plotted solar cell parameters are U_{oc} , FF and η as function of short circuit current density.

- Figure 5.28:** Cross-sectional structure of the eta solar cell of the type $\text{SnO}_2:\text{F}/\text{TiO}_2/\text{In}(\text{OH})_x\text{S}_y/\text{Pb}(\text{OH})_x\text{S}_y/\text{PEDOT:PSS}/\text{Au}$.
- Figure 5.29:** Energy dispersive X-ray mapping of the elemental composition in material of various layers used in fabricating eta solar cell, Au is element gold in Au back contact, Sn is tin in $\text{SnO}_2:\text{F}$ layer, C is carbon in PEDOT:PSS, Ti is element titanium in TiO_2 , Pb is lead in $\text{Pb}(\text{OH})_x\text{S}_y$, and In is the element indium in $\text{In}(\text{OH})_x\text{S}_y$.
- Figure 5.30:** Statistics of 15 cells showing performance trend of eta solar cell when the layer thickness is coated at the number of cycles shown in parentheses. Dash-dot line H marks through parameters of one of the cells.
- Figure 5.31:** Statistics of 25 cells showing performance trend of different eta solar cells when the layer thickness is coated the number of cycles shown in parentheses.
- Figure 5.32:** Statistics of 27 cells showing performance trend of eta solar cell when the layer thickness is coated the number of cycles shown in parentheses.
- Figure 5.33:** Statistics of 18 cells showing performance trend of eta solar cell when the layer thickness is coated the number of cycles shown in parentheses.
- Figure 5.34:** Simplified architecture solar cell structure of the type $\text{SnO}_2:\text{F}/\text{TiO}_2/\text{In}(\text{OH})_x\text{S}_y/\text{In}(\text{OH})_x\text{S}_y/\text{Au}$, this device has PEDOT:PSS layer eliminated.
- Figure 5.35:** J - U characteristics for $\text{SnO}_2:\text{F}/\text{TiO}_2/\text{In}(\text{OH})_x\text{S}_y/\text{Pb}(\text{OH})_x\text{S}_y/\text{Au}$ solar cell structure shown in figure 5.34.
- Figure 5.36:** Simplified architecture solar cell structure of the type $\text{SnO}_2:\text{F}/\text{In}(\text{OH})_x\text{S}_y/\text{In}(\text{OH})_x\text{S}_y/\text{PEDOT:PSS}/\text{Au}$, the device has TiO_2 layer eliminated.
- Figure 5.37:** J - U characteristics of $\text{SnO}_2:\text{F}/\text{In}(\text{OH})_x\text{S}_y/\text{Pb}(\text{OH})_x\text{S}_y/\text{PEDOT:PSS}/\text{Au}$ solar cell structure shown in figure 5.36.
- Figure 5.38:** Simplified architecture solar cell structure of the type $\text{SnO}_2:\text{F}/\text{In}(\text{OH})_x\text{S}_y/\text{Pb}(\text{OH})_x\text{S}_y/\text{Au}$, the device has TiO_2 and PEDOT:PSS layers eliminated.
- Figure 5.39:** J - U characteristics of $\text{SnO}_2:\text{F}/\text{In}(\text{OH})_x\text{S}_y/\text{Pb}(\text{OH})_x\text{S}_y/\text{Au}$ solar cell structure shown in figure 5.38.
- Figure 5.40:** Light soaking characteristics for $\text{SnO}_2:\text{F}/\text{TiO}_2/\text{In}(\text{OH})_x\text{S}_y/\text{Pb}(\text{OH})_x\text{S}_y/\text{PEDOT:PSS}/\text{Au}$ eta solar cell, U_{oc} , FF and η are plotted as function of light soaking duration.
- Figure 5.41:** Light soaking characteristics for $\text{SnO}_2:\text{F}/\text{TiO}_2/\text{In}(\text{OH})_x\text{S}_y/\text{Pb}(\text{OH})_x\text{S}_y/\text{PEDOT:PSS}/\text{Au}$ of one week old eta solar cell, U_{oc} , FF and η are plotted as function of light soaking duration.
- Figure 5.42:** Light soaking characteristics for $\text{SnO}_2:\text{F}/\text{In}(\text{OH})_x\text{S}_y/\text{Pb}(\text{OH})_x\text{S}_y/\text{PEDOT:PSS}/\text{Au}$ solar cell, U_{oc} , FF and η are plotted as function of light soaking duration.

- Figure 5.43:** Light soaking characteristics for $\text{SnO}_2:\text{F}/\text{TiO}_2/\text{In}(\text{OH})_x\text{S}_y/\text{Pb}(\text{OH})_x\text{S}_y/\text{Au}$ solar cell, U_{oc} , FF and η are plotted as function of light soaking duration.
- Figure 5.44:** Light soaking characteristics for $\text{SnO}_2:\text{F}/\text{In}(\text{OH})_x\text{S}_y/\text{Pb}(\text{OH})_x\text{S}_y/\text{Au}$ solar cell, U_{oc} , FF and η are plotted as function of light soaking duration.
- Figure 5.45:** External Quantum efficiency characteristics for $\text{SnO}_2:\text{F}/\text{In}(\text{OH})_x\text{S}_y/\text{Pb}(\text{OH})_x\text{S}_y/\text{PEDOT}:\text{PSS}/\text{Au}$ solar cell device. EQE spectrums shown were used in monitoring degradation after light soaking.
- Figure 5.46:** Current - voltage characterization in the dark and under illumination at different temperatures in the range 200 - 320 K in steps of 20 K from one curve to the other.
- Figure 5.47:** Open circuit voltage (U_{oc}) as a function of illumination intensity and at different temperature. The data is plotted at temperature intervals of 20 K.
- Figure 5.48:** Temperature dependence of fill factor as a function of illumination intensity. Measurements are done from 200 K - 320 K at intervals of 20 K.
- Figure 5.49:** Temperature dependency of conversion efficiency as a function of illumination intensity. Measurements were done from 200 K - 320 K at intervals of 20 K.
- Figure 5.50:** Illumination intensity dependent open circuit voltage as a function of temperature. Measurements were done from $I = 0.05 \text{ mW}/\text{cm}^2$ to $100 \text{ mW}/\text{cm}^2$.
- Figure 5.51:** Illumination dependent fill factor of the eta solar cells as a function of temperature. Measurements were done from $I = 0.05$ to $100 \text{ mW}/\text{cm}^2$.
- Figure 5.52:** Illumination dependence of conversion efficiency of the eta solar cells as a function of temperature. Measurements were done from $I = 0.05$ to $100 \text{ mW}/\text{cm}^2$.
- Figure 5.53:** Temperature dependence of the diode ideality factor as extracted from dark $JU - T$ curves and $J_{sc}U_{oc} - T$ curves as shown in figure 5.46.
- Figure 5.54:** Temperature dependent reverse saturation current density as a function of inverse temperature as extracted from dark and illuminated $JU - T$ characteristics in figure 5.46.
- Figure 5.55:** Arrhenius plot of the saturation current density J_0 corrected by diode ideality factor A_i with the data extracted from illuminated characteristics as extracted from figure 5.46.
- Figure 5.56:** Activation energy of recombination derived from open circuit voltage U_{oc} as a function of temperature.
- Figure 5.57:** Proposed energy band diagram for the eta solar cell of the structure $\text{SnO}_2:\text{F}/\text{TiO}_2/\text{In}(\text{OH})_x\text{S}_y/\text{Pb}(\text{OH})_x\text{S}_y/\text{PEDOT}:\text{PSS}/\text{Au}$.
- Figure 5.58:** Temperature dependency of series resistance R_s of the eta solar cell.

List of Tables

- Table 3.1:** Summary of recombination mechanisms possible in the eta solar cell. Shown are the activation energy of reverse saturation current density, open circuit voltage extrapolation values to $T = 0$ K, and temperature dependence of ideality factor. (Schuller, 2002; Reiss, 2002; Fuertes-Marron, 2003).
- Table 4.1:** Tabulated format of the procedure followed in performing intensity and temperature dependent $JU - T$ characterization. Inner numbers shown in dark cells show the count.
- Table 5.1:** Typical solar cell parameters for different solar cells used in analysing performance trend.
- Table 5.2:** Photovoltaic parameters for eta solar cell and those for devices with simplified structures for explaining specific roles of the component layers.
- Table 5.3:** Changes in photovoltaic parameters of eta solar cell and those of simplified devices.
- Table 5.4:** Electronic parameters of the eta solar cell component materials.

CHAPTER 1

Introduction

1.1 Introduction

In the 21st century, environmental destruction and global warming are some of the gravest issues which are threatening the continued existence of both flora and fauna on planet Earth. Unfortunately, the present-day energy supplies which account for approximately 87% of the total supplies (solid fuels = 100,395 PJ; liquid fuels = 147,480 PJ; natural gas = 95,543 PJ; hydro electric = 24,792 PJ; and nuclear = 25,564 PJ, Total supplies = 393,773 PJ: all units in PJ = peta joules; the list excludes biomass energy and other sources like wind and solar energy) are principally responsible for the anthropogenic greenhouse effects, acid rain, and other multifarious negative impacts on health and the environment. There is a need for greener (environmentally friendly source) and renewable sources of energy to supplement the current mainly fossil fuel such as natural gas, petroleum, hard and brown coal, if the global warming effects are to be kept within tolerable limits (Granqvist, 1991; Schmela, 2003; Quasching, 2005).

The main source of renewable energy is the sun with energy reaching the earth surface annually being approximately about $3.9 \times 10^{24} \text{ J} = 1.08 \times 10^{18} \text{ kWh}$. This is about 10 thousand times more than the contemporary annual energy demand and much more than all available energy reserves on earth. There are two methods on how this enormous energy can be transformed into useful energy: (i) use of technological systems for direct solar energy conversion, that is, by converting incoming solar radiation directly into usable energy, examples of such technologies are: solar thermal power plants, photolysis systems for fuel production, solar collector for water heating, passive solar heating systems, and photovoltaic solar cells for electricity generation, and (ii) use of technological systems for indirect methods of solar energy conversion, examples are: wind power for wind turbine electricity generators, river water which after the process of evaporation and condensation into rainfall can be utilized later as hydroelectric power and geothermal energy, and lastly, plant growth for biofuels energy, which mainly includes biodiesel, bioethanol, biomass and biogas(Quasching, 2005).

The work reported in this thesis is on photovoltaic solar cell technologies which utilise direct solar energy conversion. Photovoltaic is a term applied to conversion of solar energy into usable electrical energy which may be utilized immediately or stored. Photovoltaic solar cell is considered a major candidate for obtaining

energy from the sun, and three reasons can be put forward for the general worldwide interest and research investment in this area: (i) Its long term energy potential is enormous and the scientific community have estimated renewable energy sources to grow from the current 12.7% to 20% by 2020 and going by the current trend the projections show it will reach 50% by 2050 if global warning threats are to be kept at bay and within the tolerable limits. The growing worldwide demand for electrical energy will be accompanied by a geographical shift since the largest growth rate will be located in developing countries. Demographers have estimated that, in not so distant future, 40% of the world population will be living in villages of developing countries where decentralized electricity generation is necessary, and stand alone systems will be the most ideal (Overstraeten and Mertens, 1986; Green, 1992), (ii) Investments in photovoltaics will help reduce poverty in developing countries and lessen the probability that armed conflicts will arise over the access to the oil resources concentrated in a few regions of the world (Schmela, 2003; Overstraeten and Mertens, 1986). (iii) Photovoltaics make use of semiconductors and, from the viewpoint of materials and processing technology is related to microelectronics hence investment in photovoltaics is also support to microelectronics industry (Overstraeten and Mertens, 1986; Sze, 1997; Quasching, 2005).

The modern age of solar cell technology dawned in 1954 when Chapin, Fuller and Pearson working at Bell Telephone Laboratories developed the first working p – n junction type of solar cell using silicon (Chapin, *et. al.*, 1954). At present, practical and reasonably priced monocrystalline, polycrystalline and amorphous silicon solar modules with efficiencies between 7% - 21% are already available in the market. However, these types of solar cells are minority carrier type of devices and the cell design requires high purity materials making these devices expensive for large scale utility supply (Chapin, *et. al.*, 1954; Overstraeten and Merten, 1986; Green, 1992).

Dye sensitized solar cell (DSSC) device invented by Brian O'Regan and Michael Grätzel at *Ecole Polytechnique Federale de Lausanne*, Switzerland, in the 1990s (O'Regan and Grätzel, 1991) is one of the most promising type of cheap alternative device to the expensive silicon solar cells. The dye sensitized solar cell is a majority carrier type of device made up of mainly nanoporous titanium dioxide ($np - TiO_2$) thin film which is covered with dye monolayer and then a liquid electrolyte is applied, the front electrode is provided by the $SnO_2:F$ glass substrate while the counter electrode is made from platinum coated glass. When light photon impinging on the solar cell through the TiO_2 window layer, charge separation occurs and it is transported by diffusion giving electrons charge into the pigment soaked nanoparticles and the holes

into the electrolyte. Recent results on these type of devices have shown conversion efficiency of about 11.1% (Chiba, *et. al.*, 2006) which is still half that of crystalline silicon. Although DSSCs are low cost in production, a number of challenges have to be overcome before these devices can serve as cheap alternative sources of energy. The main drawback is traced to encapsulation of the liquid electrolyte which is causing a serious technological problem, evaporation of the liquid electrolyte due to imperfect sealing of the solar cell and degradation of the components (dye absorber material and liquid electrolyte) especially if there is ingestion of water moisture and oxygen in the DSSC solar cell structure.

To overcome these limitations, studies to find an alternative replacement for the liquid redox electrolyte in the dye sensitized solar cell are in progress, with other options including: (i) polymer alternative materials (Matsumoto, *et. al.*, 1996; Murakoshi, *et. al.*, 1998; Yanagida, *et. al.*, 1999), (ii) a mixture of three solid salts as solvent free alternative which so far has realised 8.2% conversion efficiency (Bai, *et. al.*, 2008) and lastly, (iii) inorganic semiconductors as solid state sensitizer (Siebentritt, *et. al.*, 1997; Kaiser, *et. al.*, 2001; Bayon, *et. al.*, 2005, 2006; Oja, *et. al.*, 2006; Gavrilov, *et. al.*, 2006). This thesis focuses on the research work done on the latter. A solid state type of device based on the novel extremely thin absorber (eta) solar cell concept where $Pb(OH)_xS_y$ absorber is proposed as an alternative sensitizer for a solar cell device developed on highly structured $SnO_2:F/TiO_2/In(OH)_xS_y/Pb(OH)_xS_y/PEDOT:PSS/Au$ structure. In this solar cell device $SnO_2:F$ is the transparent conducting oxide (TCO) used both as the substrate material as well as front contact of the solar cell, TiO_2 is the highly structured window layer and n- type semiconductor, $In(OH)_xS_y$ is the buffer layer, PEDOT:PSS and Au/ C are the hole conductor and solar cell back contact, respectively.

1.2 Statement of the problem

Eta solar cell is a novel concept envisaged to yield high conversion efficiency using inexpensive materials and production methods at ultra low cost scale. Eta solar cell is a majority carrier device which does not need highly purified materials unlike silicon solar cell. The idea of making a solar cell with extremely thin absorber was based on the fact that the photo – excited charge carriers have to be transported across the absorber to the contacting n- and p- type wide band gap semiconductor materials, a vastly reduced local absorber thickness will result in considerable collection probability of charge carriers.

Solar cell device based on this concept using $Pb(OH)_xS_y$ absorber with an engineered band gap and then sandwiched between highly structured n- type TiO_2 micro-porous semiconductor and p- type organic semiconductor of PEDOT:PSS has never been fabricated. Furthermore, study on generation and recombination mechanism as well as the effects of light soaking in eta solar cell devices have also never been analysed ever since the inception of the idea of eta device in the 1990's by Professor Könenkamp's group (Siebentritt, *et. al.*, 1997) working at Hahn Meitner Institute.

1.3 Significance of the study

The novel eta solar cell is based on the dye sensitized solar cell concept, so far efficiency of 11.1% has been reported on the latter (Bai, *et. al.*, 2008) making these type of solar cells potential candidates for alternative low cost source of energy as compared to silicon based solar cells. The silicon raw materials are badly needed in microelectronics industry and the extra demand makes silicon based solar cell devices unaffordable to those living under US \$ 1 a day in the developing world where stand alone systems are popular.

Eta solar cell was developed as an alternative solvent free device to overcome encapsulation problems being encountered in DSSC, furthermore the low cost techniques used in developing eta solar cell devices such as chemical bath deposition, successive ionic layer absorption and reaction (SILAR) or sol-gel technique do not require huge capital base to set up and are cheap to scale up for large scale production of solar modules which can be used in standalone system or large solar farms for utility supply in national grid.

This study is important since it forms basis for: (i) understanding fundamental technologies in solar cell fabrication and characterization which is important for knowledge base and capacity building in area of photovoltaics, (ii) possibility of developing new materials through interfacial diffusion when materials are deposited by either chemical bath deposition or SILAR technique, and (iii) fabrication of medium sized tandem solar cell through stacking a number of layers as the proposed structure of the eta solar cell discussed in section 1.1.

1.4 Objectives of this work

The aim of this work is to fabricate and characterize a hybrid eta solar cell device of the structure $\text{SnO}_2\text{:F}/\text{TiO}_2/\text{In}(\text{OH})_x\text{S}_y/\text{Pb}(\text{OH})_x\text{S}_y/\text{PEDOT:PSS}/\text{Au}$.

The objectives in this study are:

1. Morphological characterization of TiO_2 , $\text{In}(\text{OH})_x\text{S}_y$, $\text{Pb}(\text{OH})_x\text{S}_y$ and PEDOT:PSS by scanning electron microscopy (SEM).
2. Structural characterization of TiO_2 , $\text{In}(\text{OH})_x\text{S}_y$, and $\text{Pb}(\text{OH})_x\text{S}_y$ by X-ray photoelectron spectroscopy (XPS), X-ray Auger electron spectroscopy (XAES) and Energy dispersive x-ray spectroscopy (EDX) mapping.
3. Optical spectroscopy characterization of TiO_2 , $\text{Pb}(\text{OH})_x\text{S}_y$, $\text{In}(\text{OH})_x\text{S}_y$ and PEDOT:PSS.
4. Electrical and optoelectrical characterization of the solar cell and component thin films, specifically:
 - a. Current – voltage characterization of the eta solar cell;
 - b. External quantum efficiency of the eta solar cell;
 - c. Determination of the solar cell parasitic resistance (series and parallel);
 - d. Transport mechanism of the eta solar cell;
 - e. Surface photovoltage characteristics of TiO_2 , $\text{In}(\text{OH})_x\text{S}_y$, and $\text{Pb}(\text{OH})_x\text{S}_y$.

1.5 Thesis structure

This work is divided into six chapters. Chapter 1 is the introduction, where the main theme of the work is introduced, the statement of the problem is stated and the objectives are laid down. In chapter 2, previous studies prior and during the course of doing our work are reviewed and summary of the discussion is made and critiqued to bring out the knowledge gap being filled by this work. Though this work is experimental, chapter 3 discusses theory on which calculations giving numerical results are based, while chapter 4 discusses experimental procedures followed in the course of doing this work, how the experiments were set up and how the results were arrived at are discussed in this chapter. Chapter 5 is discussion of the results and deductions based on the theory and literature review and other existing authorities. In chapter 6, conclusion is made based on our deductions after performing various experiments and testing numerous samples, and lastly suggestions are made for further work since research work can never be done exhaustively.

CHAPTER 2

Literature review

2.1 Introduction

Design concepts for photovoltaic devices which are expected to yield high conversion efficiency using low cost production methods and inexpensive materials have been proposed over the years. Some of the tested fundamental technologies include the following: (i) a dye sensitized electrochemical solar cell (DSSC), (O'Regan and Grätzel, 1991), (ii) a two photon absorption solar cell (Luque and Marti, 1997), (iii) a solid state analogue of DSSC, (Matsumoto, *et al.*, 1996; Murakoshi, *et al.*, 1998; Tennakone, *et al.*, 1998; Bai, *et al.*, 2008), and (iv) lastly the novel extremely thin absorber (eta) concept developed a few years ago by Prof. Rolf Könenkamp's group (Siebentritt, *et al.*, 1997).

The eta design concept is a new all solid state photovoltaic device which has attracted a lot of attention (Siebentritt, *et al.*, 1997; Kaiser, *et al.*, 2001; Ernst, *et al.*, 2001; Könenkamp, *et al.*, 2002; Bayon, *et al.*, 2005; 2006; Oja, *et al.*, 2006; Gavrilov, *et al.*, 2006). Eta solar cell is modeled on some features of dye sensitized solar cell (nanostructured configuration, separation of light absorption from charge transport, majority carrier device) and some classical photovoltaic devices (all solid state, inorganic materials), (Larramona, *et al.*, 2006). In eta solar cell, unlike in DSSC where a monolayer of molecular dye is used as light absorbing medium, an extremely thin layer of inorganic solid state material (for example, chemical bath deposited PbS of band gap 0.8 eV (Bayon, *et al.*, 2005; 2006), CdTe of band gap 1.5 eV (Levy-Clement, *et al.*, 2002), CuInS₂ of band gap 1.2 eV (Kaiser, *et al.*, 2001)) is used as a sensitizer instead. The thin absorber material is normally sandwiched between two wide band gap semiconductors, one n-type and the other p-type. The main advantage of this type of device is that, charge transport distance after the electron - hole pair separation within the absorber is strongly reduced, and since eta cell is a majority carrier type of device, the stringent requirements are relaxed for the electronic quality of the absorber material (Ernst, *et al.*, 2001; Belaidi, *et al.*, 2003). Additionally, these types of solar cells are fabricated on highly structured substrate window layer which can substantially reduce the transport path for the excited charge carriers in the absorber, and at the same time, increase the optical path for the photon absorption. Both the optical (enlarged surface area) and electrical (short diffusion length) properties of eta solar cell are advantageous for photovoltaic applications. For optical effects, the eta solar cell should have a structure

with typical length scale in the range of solar light wavelength, for the reduction of the electronic path, a deep structuring in the 50 – 300 nm length scale is desirable (Könenkamp, *et. al.*, 2002).

2.2 Substrate window layer for eta solar cells

One crucial aspect for the fabrication of eta solar cell is on the preparation of suitable substrates. The desirable window layer material is wide band gap semiconductor with typical bandgap $E_g > 3.0$ eV (Ernst, *et. al.*, 2003; Bayon, *et. al.*, 2005; 2006; Grätzel, 2001) for both superstrate/ substrate structured solar cells. Könenkamp *et. al.*, (2002) have reported on preparation and characterization of nanostructured semiconductor layers with different geometries. The type of thin films studied by Könenkamp, *et. al.*, (2002) consisted of large band gap semiconductors which are suitable as contacting substrate material. Two commonly used substrate materials in eta solar cells are micro- / nano- porous structured TiO_2 (Kaiser, *et. al.*, 2001; Ernst, *et. al.*, 2001; Bayon, *et. al.*, 2005; 2006) and columnar ZnO (Levy-Clement, *et. al.*, 2005; Krunk, *et. al.*, 2008). TiO_2 layers normally used have an open micro - porous/ nanoporous morphology. The TiO_2 thin films with open micro - porous structure is mainly deposited by either sol – gel or spray pyrolysis technique (Kaiser, *et. al.*, 2001; Ernst, *et. al.*, 2001), while for nanostructured morphology are mainly deposited by doctor blade, sol – gel or rf sputtering techniques (Kaiser, *et. al.*, 2001). On the other hand, the ZnO with columnar microstructure is coated using electrodeposition technique, typical shape is as shown in figure 2.1 (Könenkamp, 2002; Levy – Clement, *et. al.*, 2005; Zhang, *et. al.*, 2004). Another method for depositing nanorods/ nanowires structured ZnO is by spray pyrolysis (Krunk, *et. al.*, 2008).

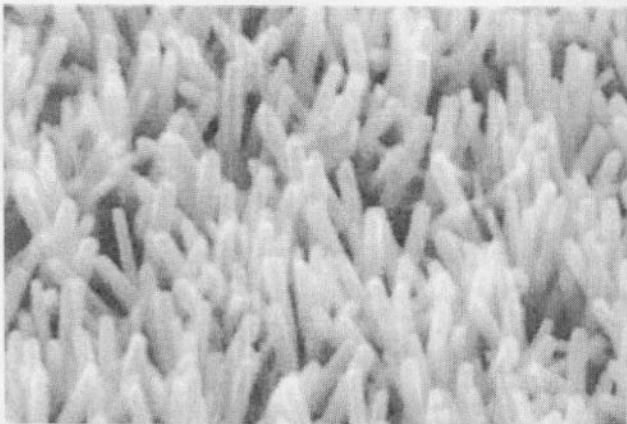


Figure 2.1: Scanning electron micrograph of columnar zinc oxide (ZnO) thin film (Könenkamp, *et. al.*, 2002).

2.3 Absorber materials for eta solar cells

The band gap of the absorber material for the eta solar cell typically ranges between $0.8 \text{ eV} < E_g < 1.8 \text{ eV}$ (Kaiser, *et. al.*, 2001; Ernst, *et. al.*, 2001, Bayon, *et. al.*, 2005; 2006). The absorber layer of the eta solar cell, unlike that of the dye sensitized solar cell, is a solid state semiconductor material which is used as a sensitizer (Siebentritt, *et. al.*, 1997; Kaiser, *et. al.*, 2001; Lenzmann, *et. al.*, 2004). The eta layer separates the light photon absorption process from charge transportation, unlike in the case of classical solar cell where the two processes are not separated. Several semiconductor materials have been used as extremely thin absorber films for the eta solar cell, for example: PbS – Q dots (Q – dots: quantum dots) (Bayon, *et. al.*, 2005;2006), CuInS_2 (Belaidi, *et. al.*, 2003), PbS (Bayon, *et. al.*, 2005; 2006), $\text{Pb(OH)}_x\text{S}_y$ (Gavrilov, *et. al.*, 2006; Oja, *et. al.*, 2006), and $\text{In(OH)}_x\text{S}_y$ (Lenzmann, *et. al.*, 2004). However, the materials that have shown the best results so far in terms of conversion efficiency are the cadmium derivatives compounds of CdTe (Belaidi, *et. al.*, 2003) and CdSe (Levy-Clement, *et. al.*, 2005). A comparative study of different extremely thin absorbers used in eta solar cell with reference to CdTe absorber was reported by Belaidi, *et. al.*,(2003). The device studied by Belaidi, *et. al.*,(2003) had an open circuit potential, $U = 0.67 \text{ V}$ and short circuit current density, $J = 9 \text{ mA/cm}^2$. The $J - U$ characteristics of the type of solar cell investigated by Belaidi, *et. al.*, (2003) however, showed very low fill factor which was attributed to the large band gap offset between the TiO_2/CdTe heteronjunction. In their study (Belaidi, *et. al.*, 2003) efforts to alloy the CdTe absorber using mercury in order to reduce the bandgap offset, did not improve the fill factor for $\text{TiO}_2/\text{CdHgTe}$ device, though higher quantum efficiency was obtained with increasing Hg concentration nonetheless.

Different deposition techniques have been employed in coating the eta film with the most common being chemical bath deposition (CBD). The CBD has been used in coating CdS (Larramona, *et. al.*, 2006) and PbS (Bayon, *et. al.*, 2005; 2006). Other techniques used are Successive Ion Layer Absorption and Reaction (SILAR). SILAR is most appropriate for ultra low cost deposition method; materials like PbS – Q dots (Bayon, *et. al.*, 2006) and $\text{Pb(OH)}_x\text{S}_y$ (Oja, *et. al.*, 2006; Gavrilov, *et. al.*, 2006) have been coated using this technique. A closely related deposition procedure to SILAR, called Ion Layer Gas Absorption and Reaction (ILGAR) has also been used mainly for depositing CuInS_2 for eta solar cell (Kaiser, *et. al.*, 2001). Depending on availability and suitability of deposition method, vapour phase epitaxy for depositing CdTe (Levy-Clement, *et. al.*, 2002) and electrodeposition method have been used widely; the latter has been reported by Belaidi, *et. al.*, (2003) and Ernst, *et. al.*, (2003), for depositing CdTe absorber.

2.4 Recombination barrier, the buffer or tunneling layer.

The idea in eta solar cell concept to design the device by sandwiching an extremely thin absorber material between two transparent n- type and p- type layers was envisaged as a way of reducing bulk recombination in the absorber material, since the separated light absorption and charge carrier processes are within the proximity of the absorber, p- type and n- type materials, respectively (Lenzmann, *et. al.*, 2004; Ernst, *et. al.*, 2000; Kaiser, *et. al.*, 2001). However, whilst spontaneous decay of the charge carrier within the absorber can be efficiently suppressed, the enlarged interface of the n- type and p- type materials may lead to considerable increase in interface recombination probabilities, which can be mitigated by surface passivation using the right tailoring material (Lenzmann, *et. al.*, 2004). The performance of both the dye sensitized solar cell and solid state sensitized solar cell improves significantly when a very thin insulating tunnel barrier material for example MgO, Al₂O₃, ZnO, TiO₂, ZrO₂, Y₂O₃ (Grasso and Burgelman, 2004) etc, or non – insulating buffer layer material, examples of such materials are CdS (Larramona, *et. al.*, 2006), In₂S₃ (O'Hayre, *et. al.*, 2007), In(OH)_xS_y (Bayon, *et. al.*, 2005; 2006) etc, is introduced at the active interface (between the window layer and absorber material) of the solar cell.

In 2003, Wienke *et. al.*, (2003) reported on a semiconductor fabricated using In(OH)_xS_y as a suitable recombination barrier in TiO₂/inorganic absorber heteronjunction. The introduction of In(OH)_xS_y in a solid state TiO₂/In(OH)_xS_y/CuInS₂/Au solar cell was observed by Wienke, *et. al.*, (2003) to lead to a considerable delay in electron recombination, which was deduced from the following methods (i) increased contact potential difference (Δ CPD) value and slower decay of the Δ CPD signal. (ii) Improved current density as a function of voltage (J - U) characteristics for solar cells with In(OH)_xS_y buffer layer as compared to solar cells which had TiO₂/CuInS₂/Au structure (Wienke, *et. al.*, 2003). In(OH)_xS_y has also been utilized as a buffer for the novel eta solar cells as described by Bayon *et. al.*, (2005; 2006) and Oja *et. al.*, (2006).

Lenzmann, *et. al.*, (2004) reported that In(OH)_xS_y, In₂S₃, and ultrathin Al₂O₃, are suitable materials as recombination barrier for solar cells with TiO₂/CuInS₂ structure, and related extremely thin absorber concept devices. In their work Lenzmann, *et. al.*, (2004), demonstrated that inserting a buffer layer or tunneling barrier in a solar cell structure of the type TiO₂/Al₂O₃/CuInS₂, TiO₂/In₂S₃/CuInS₂ or TiO₂/In(OH)_xS_y, makes the device display marked improvements in its characteristic photovoltaic parameters. The improvements observed were attributed to efficient suppression of the interface

recombination which (Lenzmann, *et. al.*,2004) was believed to be the limiting factor for the photovoltaic performance of the $\text{TiO}_2/\text{CuInS}_2$ solar cell.

A similar concept has also been applied to solid state type dye sensitized solar cells consisting of n- type TiO_2 and p- type CuI , with a monolayer of ruthenium bipyridyl dye molecules placed at the interface (Tennakone *et. al.*, 1998; Kumara, *et. al.*, 2002; Zhang, *et. al.*, 2004). The device studied by Zhang, *et. al.*,(2004) having $\text{TiO}_2/\text{Al}_2\text{O}_3/\text{dye}/\text{CuI}$ was observed to have low conversion efficiency when Al_2O_3 blocking layer is not deposited. The low conversion efficiency was ascribed to interfacial charge recombination in solid state DSSC which consists of reduction of the oxidized dye by an electron from TiO_2 before hole injection into CuI . Deposition of a 0.19 nm thick Al_2O_3 layer lead to improved performance of the device with electron lifetime decay increasing by a factor of 1.5 times, while conversion efficiency improved by a factor of 1.27 and 1.34 when the solar cell was subjected to $31.4 \text{ mW}/\text{cm}^2$ and $89 \text{ mW}/\text{cm}^2$ of simulated sunlight, respectively (Zhang, *et. al.*, 2004).

An insightful theoretical treatise by Grasso and Bergelman, (2004) describes the mechanism that might be responsible for the reported improvements in solar cell characteristics especially in $\text{TiO}_2/\text{CuInS}_2$ based nanostructured eta solar cells. In the work by Grasso and Bergelman (2004), mechanisms to improve open circuit voltage (U_{oc}) without compromising short circuit current density (J_{sc}) are discussed with reference to intermediate tunnel barrier of either Al_2O_3 , MgO or conducting buffer layer of CdS . In reference to study done by Grasso and Bergelman, (2004), the following procedures should be adopted in order to realise meaningful improvements (i) use of a buffer layer material which introduces an energy barrier that is higher for dark current than for light current, (ii) use of a buffer layer material that may reduce interface states density at either side of the intermediate layers, that is, between absorber and n- type and p- type semiconductor, respectively, and (iii) reduction of the effect of interface states by tailoring materials to achieve more favourable position of the Fermi levels at the recombination, and chemical and electrostatic interactions at the interfaces.

2.5 Eta solar cells a review

Since the first solar cell based on the novel eta concept was reported in late 1990s by Prof. Rolf Könenkamps' group (Sibentritt, *et. al.*, 1997), these devices have remained of very low conversion efficiency with the highest ever reported being 2.3% (Levy-Clement, *et. al.*, 2005). Few trials have been

done on eta solar cell despite the fact that theoretically they were envisaged to overcome the limitations of the efficiency predicted to be larger than 10% (Taretto and Rau, 2005; Oja, *et. al.*, 2006) and instability of dye sensitized solar cell. The reason for slow growth in eta solar cell research, in our opinion, is partly because it was a European Union funded project with eta fellows drawn from few institutions which included: Energy Research Centre of the Netherlands - Coordinator (ECN), Hahn Meitner Institute (HMI), Tallin Technical University (TTU), Uppsala University, Delft University of Technology, Weizmann Institute of Science, and University of Gent. Eta research continues as separate institutional funded project, with few researchers working in the area who were not formerly eta project fellows. Another reason for this slow growth is the issue of stringent thickness requirement of the absorber material. The thickness of the absorber materials was proposed to be between 10 – 50 nm range, and with most deposition techniques it is not easy to grow thin films in this regime without formation of discontinuous island clusters, thus forcing the thickness of the absorber material to exceed the defining range.

The continued study in these types of devices as alternative photovoltaic systems and for solar cell materials is significant from both the fundamental (understanding on how these devices work) and technological perspective. Studies done so far have shown that the n- type choice of materials are TiO_2 and ZnO , while the p- type choice are inorganic materials such as CuInS_2 , CuI , CuSCN and organic materials like PEDOT:PSS and OMetad (Bayon, *et. al.* 2005; 2006). The absorber material has been predominantly PbS (Bayon, *et. al.*, 2005; 2006), CdTe , CdHgTe , CuInS_2 , $\text{Pb(OH)}_x\text{S}_y$ (Oja, *et. al.*, 2006) and a-Si (Siebentritt, *et. al.*, 1997), while material of choice for buffer layer has been $\text{In(OH)}_x\text{S}_y$ (Bayon, *et. al.*, 2005; 2006; Oja, *et. al.*, 2006; Gavrillov, *et. al.*, 2006), In_2S_3 , Al_2O_3 (Lenzmann, *et. al.*, 2004; Zhang, *et. al.*, 2004), ZrO , Y_2O_3 and CdS (Lenzmann, *et. al.*, 2004). Some of the milestone techniques in eta solar cell studies are now reviewed.

Ernst, *et. al.*, (2001) reported studies on techniques to improve the eta solar cell performance by studying the effects of the front and back contact and modification of TiO_2/CdTe interface using a buffer layer. The device studied comprised n- type porous TiO_2 substrate covered with a CdTe film with local thickness of 150 – 250 nm. The porous TiO_2 layer was coated by spray pyrolysis technique using titanium isopropoxide mixed with 2 – propanol as precursor. The CdTe layer was deposited using the conformal method on the TiO_2 substrate using electrodeposition technique followed by subsequent dipping in saturated CdCl_2 solution in methanol and annealing in air at 450 °C. Three contact modifications were studied by either

depositing 25 nm thick compact TiO₂ front contact prior to deposition of porous TiO₂, or using vacuum deposited Au back contact or conductive pastes containing carbon C, or alternatively use of silver, Ag colloids mixed with small amount of copper. Finally the TiO₂/CdTe junction was modified by inserting CdS buffer layer with local thickness ranging between 5 – 200 nm. The buffer layer was deposited through two methods, either by use of standard chemical bath deposition (CBD) or by use of the novel ion layer gas reaction and absorption technique (ILGAR). Ernst *et. al.*, (2001) obtained under AM 1.5 condition short circuit current density of around 8.7 mA/cm², and an open circuit voltage of 0.67 volts. The shape of the J – U curve displayed a strong voltage dependence of the photocurrent and a low fill factor. The results of quantum efficiency data showed a substantially reduced carrier collection with increasing forward voltage. Their study found that, front and back contact of either Ag, C or Au do not have profound effect on the cell performance while interface passivation seemed to be of importance for the eta solar cell parameters.

Diffusion length of charge carriers within the absorbing materials is one of the factors which limit the conversion efficiency in eta solar cells. Kaiser *et. al.*, (2001) explained the effect of the deposition method and structure of the underlying substrate materials for CuInS₂ (CIS) sensitized eta solar cell. Different TiO₂ substrates prepared by doctor blade and spray pyrolysis techniques were used as n- type wide bandgap semiconductor. The results showed that, for eta solar cell of multilayer p-i-n structure of the type TiO₂/CuInS₂/CuSCN, the nanoporous np-TiO₂ had the advantage of enhanced light path due to surface enlargement and multiple scattering which is more pronounced than in microporous, μp-TiO₂ structure. The reason for this difference was attributed to the effective embedding of CIS within the electric field of the p- and n- type semiconductors when np- structure is used compared to μp- structure. The type of solar cell reported by Kaiser, *et. al.*, (2001) did not use a buffer layer. Unlike the device studied by Kaiser *et. al.*,(2001), a solar cell device using, μp-TiO₂ was demonstrated to work when a CdTe absorber is used, (Ernst, *et. al.*,2003; Belaidi, *et. al.*,2003). Studies by Ernst, *et. al.*,(2003) and Belaidi, *et. al.*,(2003) have made comparison of planar and microporous structured devices, with the latter structure showing superior performance. The device was also modified from the original SnO₂:F/TiO₂/CdTe/Au structure, by alloying CdTe using mercury; the resulting device SnO₂:F/TiO₂/Hg_xCd_{1-x}Te/Au showed adjustment of the interface band offsets at the TiO₂/absorber junction resulting in improved conversion efficiency. A similar idea of modifying CdTe has been pursued by Levy-Clement *et. al.*,(2002), whose study explored the properties of a new composite structure based on CdTe/ZnO. The key feature of this type of device is an extreme surface enlargement by a factor of 100 times or larger, relative to the dense thin films. This feature allows the

reduction of the absorber material thickness by the same order of magnitude, hence making them suitable for application in eta solar cell devices. The work by Levy-Clement *et. al.*, (2002) showed that CdTe/ZnO has similar optical properties comparable to those of bulk CdTe, which possesses strong light trapping properties making it favourable for eta cell application.

The type of solar cell device we studied was based on Larramona, *et. al.*, (2006) recently investigated an eta solar cell device of the type $\text{TiO}_2/\text{CdS}/\text{CuSCN}$ with promising results. The device displayed 100% internal quantum efficiency injection, 1.3% conversion efficiency and U_{oc} and FF of about 0.85 V and 0.65, respectively. The aim of the work done by Larramona, *et. al.*,(2006) was to fabricate eta solar cell with conversion efficiency exceeding 3%, but the nature of the bandgap of the CdS absorber used made it untenable; nonetheless their work contributed fundamental knowledge useful for realising higher conversion efficiencies. The following suggestions were put forward: it is worthwhile investigating the nature of absorber coating and type of nanostructure properties of the substrate window layer, as well as properties of the p- type filler material. Also, in order to obtain more reproducible cell efficiencies, it is advisable to have absorber materials having broad spectrum of light absorption such as those used in classical thin film devices.

Recently, interest in ultra thin eta solar cell at ultra low cost scale has been demonstrated by Gavrilov *et. al.*, (2006), and Oja, *et. al.*, (2006). These new ideas combine the use of inexpensive substrates and materials, non – vacuum based deposition techniques, and low temperature processes as wet chemical treatment, etc. The works of Gavrilov *et. al.*, (2006) and Oja, *et. al.*, (2006), save for the deposition techniques, are similar to the one reported by Bayon, *et. al.*, (2005; 2006). In ultra thin coatings, $\text{In}(\text{OH})_x\text{S}_y/\text{Pb}(\text{OH})_x\text{S}_y$ layers were deposited by SILAR technique unlike the CBD used by Bayon, *et. al.*, (2005; 2006). Gavrilov, *et. al.*, (2006) studied ultra thin SILAR deposited $\text{In}(\text{OH})_x\text{S}_y/\text{Pb}(\text{OH})_x\text{S}_y$ heterostructure, and concluded that, the heterojunction forms a selective surface suitable for fabricating extremely thin absorber solar cell when combined with organic materials. The prospect of fabricating eta solar cell using the selective surface suggested by Gavrilov, *et. al.*,(2006) was pursued further by Oja, *et. al.*, (2006), where they worked on a device consisting of $\text{TiO}_2/\text{In}(\text{OH})_x\text{S}_y/\text{Pb}(\text{OH})_x\text{S}_y/\text{PEDOT:PSS}/\text{Au}$, utilizing an ultra thin SILAR deposited heterojunction. In the work of Oja, *et. al.*,(2006), the question of the specific role of $\text{In}(\text{OH})_x\text{S}_y/\text{Pb}(\text{OH})_x\text{S}_y$ remained elusive despite the observation from quantum efficiency measurement scanned (180 nm – 900 nm), $\text{Pb}(\text{OH})_x\text{S}_y$ seemed to have no significant contribution. The most encouraging fact about the ultra thin concept for eta solar cell is that efficiency of 3 – 5% seems

feasible, though Gavrilov, *et. al.*, (2006) and Oja, *et. al.*, (2006) only reported efficiency of approximately 1%.

Theory

In this work, we proposed to study a solar cell device using the following multilayer structure: $\text{SnO}_2:\text{F}/\text{TiO}_2/\text{In}(\text{OH})_x\text{S}_y/\text{Pb}(\text{OH})_x\text{S}_y/\text{PEDOT}:\text{PSS}/\text{Au}$. The type of solar cell device we studied was based on the novel eta concept. In our device, $\text{Pb}(\text{OH})_x\text{S}_y$ was used as the eta material sandwiched between an inorganic n- type semiconductor and organic p- type semiconductor, with $\text{In}(\text{OH})_x\text{S}_y$ as a buffer layer. As revealed in the literature, the type of solar cell had not been previously investigated. The $\text{Pb}(\text{OH})_x\text{S}_y$ was engineered to widen its band gap from its bulk material band gap of $E_g = 0.4 \text{ eV}$ to approximately 1 eV, consequently making it possible to maximize its absorption capabilities in solar spectrum for use as light photon absorber. Furthermore transport mechanism has also not been studied before in solar cell devices based on the novel eta concept despite the widely investigated photovoltaic properties of these types of devices (Ernst, *et. al.*, 2001; Kaiser, *et. al.*, 2001; Lenzenmann, *et. al.*, 2002; Levy – Clement, *et. al.*, 2005).

(eta material, is known as electrochemical material (Nelson, 1980; Grazia, 2001)

In doing this work, we filled a knowledge gap by availing crucial fundamental knowledge on an engineered bandgap $\text{Pb}(\text{OH})_x\text{S}_y$ thin film grown by chemical bath deposition technique to be used in fabrication of solar cells based on eta concept, and also reported for the first time transport mechanisms studies in eta solar cell devices, as well as the effects of light soaking.

carrier in the study of semiconductors is the Fermi level and level of the available electron energy level at low temperature. The position of the Fermi level relative to the conduction band is fundamental in determining the electrical properties of a semiconductor. In an intrinsic semiconductor, the Fermi level is symmetrically between the conduction band and the valence band. The process of doping a semiconductor alters the position of the Fermi level, such that, in an n-type semiconductor, it is adjusted upward near the conduction band, while in a p-type semiconductor, it is shifted towards the valence band, as is illustrated in figure 3.1 (Nelson, 2003)

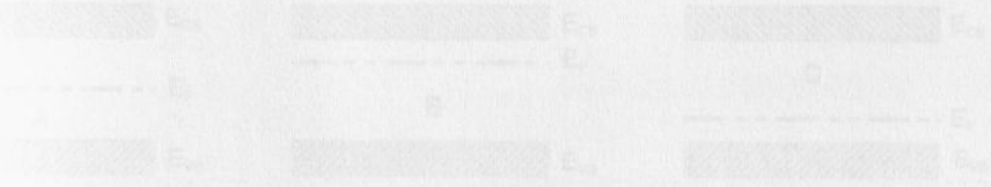


Figure 3.1 Semiconductor energy band diagram showing (A) intrinsic semiconductor, (B) n-type semiconductor and (C) p-type semiconductor.

CHAPTER 3

Theory

3.1 Photovoltaic solar cell

The mostly commonly known photovoltaic solar cells are derived from a p – n junction formed by bringing two asymmetrically doped semiconductors together. A semiconductor doped with donor impurities has an increased number of electrons and it is known as n – type semiconductor, while that which is doped with acceptor impurities has an increased number of holes and it is known as p – type semiconductor. When two asymmetrically doped semiconductors of the same material are brought into contact to form a p – n junction, this is usually known as p – n homojunction, while if two asymmetrically doped semiconductor of different semiconductor materials are brought into contact to form a p – n junction, this is usually referred to as p – n heterojunction. A solid state solar cell made from any of the two procedures is known as p – n homojunction/ or heterojunction solar cell, respectively. Another type of solar cell, whose active interface contains a liquid material, is known as electrochemical solar cell (Cooke, 1990; Grätzel, 2001).

3.1.1 Ideal solar cell

A semiconductor is characterized by energy bandgap E_g , the energy difference between conduction band, E_{CB} and valence band, E_{VB} . An important parameter in the study of semiconductors is the Fermi level energy E_F , the top most of the available electron energy level at low temperature. The position of the Fermi level in relation to the conduction band is fundamental in determining the electrical properties of a semiconductor. In an intrinsic semiconductor, the Fermi level is symmetrically between the conduction band and valence band. The process of doping a semiconductor alters the position of the Fermi level, such that, in an n – type semiconductor, it is adjusted upward near the conduction band, while in a p – type semiconductor, it is shifted towards the valence band, as is illustrated in figure 3.1 (Nelson, 2003)

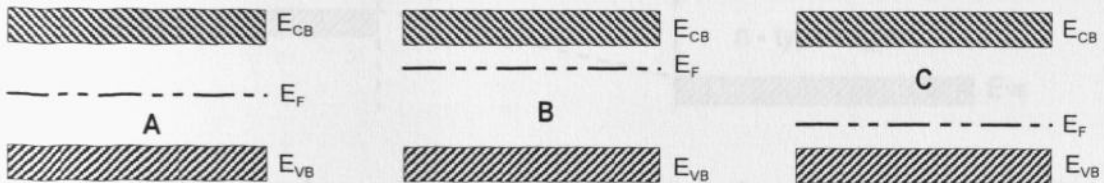


Figure 3.1: Semiconductor energy band diagram showing (A) intrinsic semiconductor, (B) n - type semiconductor, and (C) p - type semiconductor.

When n – type and p – type semiconductors are brought into contact to form a p – n junction, under equilibrium condition the Fermi level of the two semiconductors aligns to the same level as is shown in figure 3.2. At the p – n junction, the existence of different charge carrier density gradient leads to diffusion currents to flow. Electrons diffuse from n – side to p – side; also, holes diffuse from p – side to n – side. The remaining charge carriers lead to build up of electric fields (potential gradient) at the interface which leads to generation of drift currents. The drift currents flow in the opposite direction to the diffusion current. The electron and hole current densities can each have a drift component and diffusion component. The combined current densities are described by the following equations (Farhrenbruch and Bube, 1983; Kazmerski, 1997; Cooke, 1990; Groetzberger, *et. al.*,2003)

$$J_e = qn\mu_e\xi + qD_e \frac{dn}{dx} \text{ A/m}^2 \tag{3.1}$$

$$J_h = qp\mu_h\xi - qD_h \frac{dp}{dx} \text{ A/m}^2 \tag{3.2}$$

where e and h denote the electrons and holes, respectively, q is quantity for elementary charge, n and p are the electron and hole charge carrier density, respectively, ξ depicts the electric field, $\mu_{e,h}$ are the electron and hole motilities, respectively, while, $D_{e,h}$ describes the electron and hole diffusion coefficients which are defined by $D_{e,h} = \mu_{e,h} kT/q$, where k is the Boltzmann constant and T is the temperature.

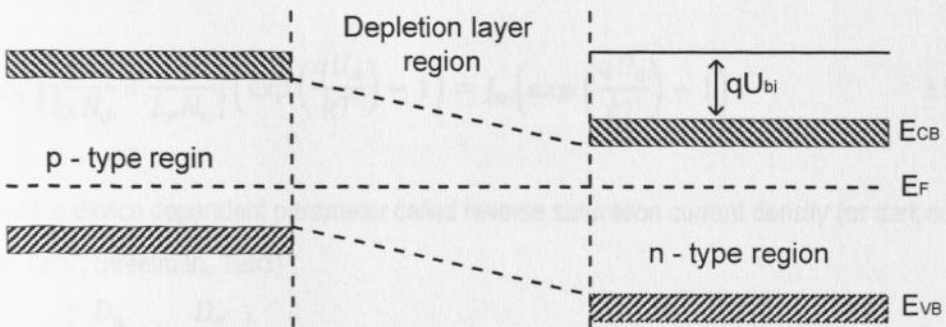


Figure 3.2: Band diagram of a p - n junction of two asymmetrically doped semiconductors at equilibrium. E_{VB}, E_{CB} and E_F, describe valence band, conduction band and Fermi level energy, respectively and U_{bi} is the built-in voltage.

At the junction, the hole current at the edge of n – type region is entirely a diffusion current. Similarly, the electron current injected into the edge of the p – type side is diffusion current. These diffusion currents are respectively given by (Farhrenbruch and Bube, 1983; Cooke, 1990; Green, 1992)

$$J_{hdiff} = \frac{qD_h}{L_h} p_n \left(\exp\left(\frac{qU_a}{kT}\right) - 1 \right) \text{ A/m}^2 \quad 3.3$$

$$J_{ediff} = \frac{qD_e}{L_e} n_p \left(\exp\left(\frac{qU_a}{kT}\right) - 1 \right) \text{ A/m}^2 \quad 3.4$$

where $p_n = n_i^2/n_n = n_i^2/N_d$ and $n_p = n_i^2/p_p = n_i^2/N_a$, and p_n and n_p are the minority carrier densities for holes and electrons, respectively; n_n and p_p are the majority carrier density for electrons and holes, respectively, $D_{e,h}$ defines the carrier diffusion constants for electrons and holes, while N_a and N_d are the concentrations of the acceptor and donor impurities, respectively. The electron and hole diffusion length is defined by $L_{e,h} = \sqrt{D_{e,h}\tau_{e,h}}$, where $\tau_{e,h}$ are the lifetimes for electrons and holes, while U_a is the applied voltage.

Thus the total current density in the diode is given by superposition of equations 3.3 and 3.4 and inserting values of p_n and n_n respectively to give (Nelson, 2003; Streetman, 1993; Sze, 1997):

$$J = qn_i^2 \left[\frac{D_h}{L_h N_d} + \frac{D_e}{L_e N_a} \right] \left(\exp\left(\frac{qU_a}{kT}\right) - 1 \right) = J_o \left(\exp\left(\frac{qU_a}{kT}\right) - 1 \right) \quad 3.5$$

where J_o defines a device dependent parameter called reverse saturation current density (or dark current) given by (Sze, 1997; Streetman, 1993)

$$J_o = qn_i^2 \left[\frac{D_h}{L_h N_d} + \frac{D_e}{L_e N_a} \right] \quad 3.6$$

Thus for an ideal solar cell, the situation when the solar cell is in the dark, and under illumination are described by equations 3.7 and 3.8 and represented graphically as shown in figure 3.3:

$$J_{dark} = J_o \left(\exp \left(\frac{qU_a}{kT} \right) - 1 \right) \quad 3.7$$

$$J_{light} = J_o \left(\exp \left(\frac{qU_a}{kT} \right) - 1 \right) - J_{ph} \quad 3.8$$

where J_{ph} is the photon generated current density (Sze, 1997, Cooke, 1990, Fahrenbruch and Bube, 1983).

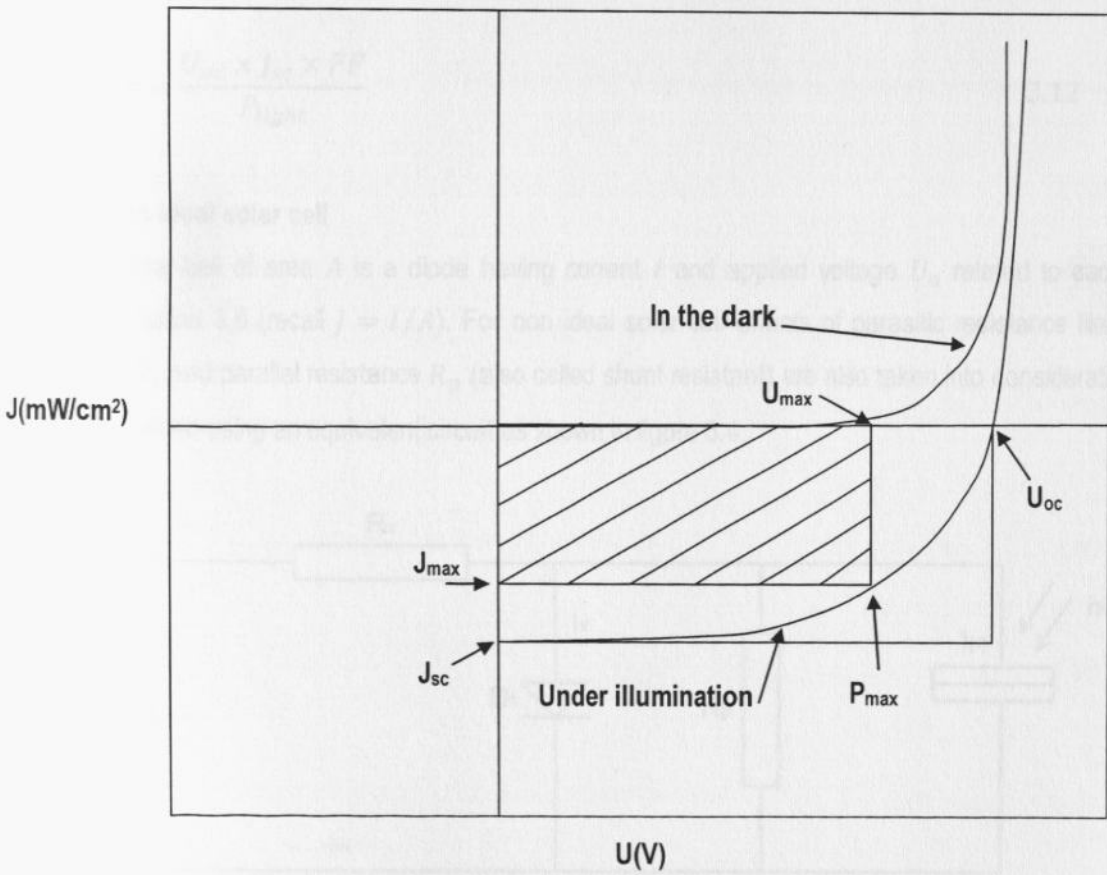


Figure 3.3: J - U characteristics for a solar cell in the dark and under illumination.

Under illumination, other important solar cell parameters can be derived. The open circuit voltage U_{oc} ($U_a = U_{oc}$) defined by $J(U_{oc}) = 0$, can be deduced from equation 3.8 which gives:

$$U_{oc} = \frac{kT}{q} \ln \left(\frac{J_{ph}}{J_0} \right) \quad 3.9$$

The other parameters which can be deduced from figure 3.3 include the maximum power, fill-factor (FF), and operating efficiency (η) of the solar cell under given conditions, for example air mass AM1.5 conditions.

$$P_{max} = U_{max} \times J_{max} \quad 3.10$$

$$FF = \frac{U_{oc} \times J_{sc}}{P_{max}} \quad 3.11$$

$$\eta = \frac{U_{oc} \times J_{sc} \times FF}{P_{light}} \quad 3.12$$

3.1.2 Non ideal solar cell

In a real solar cell of area A is a diode having current I and applied voltage U_a related to each other through equation 3.8 (recall $J = I/A$). For non ideal solar cell effects of parasitic resistance like series resistance R_s and parallel resistance R_p (also called shunt resistant) are also taken into consideration, this can be explained using an equivalent circuit as shown in figure 3.4.

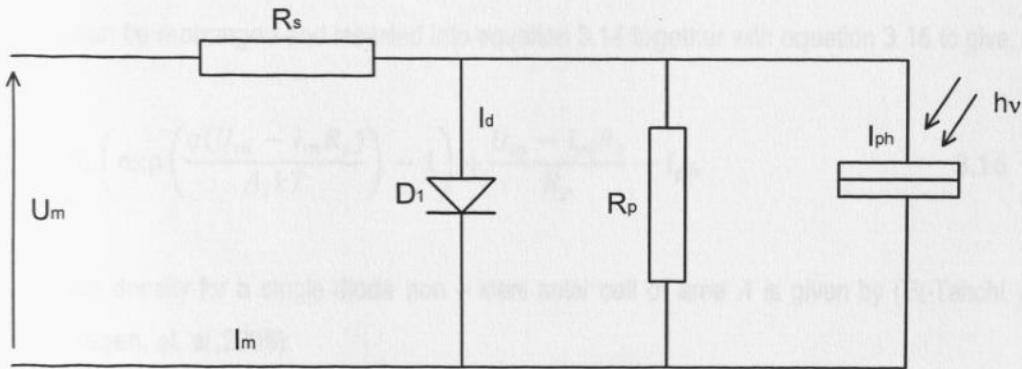


Figure 3.4: Equivalent circuit for non - ideal single diode solar cell, I_d is the current through the diode; I_{ph} is current generated due to energy transfer of the light photons $E = h\nu$. U_m and I_m are the measured voltage and current, respectively.

Figure 3.4 shows a schematic equivalent circuit of non-ideal solar cell with the following parameters shown: measured voltage, U_m , measured current, I_m , current through the diode, I_d , photon generated current, I_{ph} , and the parasitic resistances, R_p and R_s .

Using the equivalent circuit analysis, and applying the Kirchhoff's law the following can be deduced:

$$U_m = U_a + I_m R_s \tag{3.13}$$

$$I_m = I_d + \frac{U_a}{R_p} \tag{3.14}$$

where U_m and I_m are the measured voltage across the solar cell and total measured current, respectively.

Equation 3.8 for a solar cell of area A can be rewritten as follows:

$$I_d = I_o \left(\exp \left(\frac{qU_a}{A_i kT} \right) - 1 \right) - I_{ph} \tag{3.15}$$

where A_i is a correction term called ideality factor.

Equation 3.13 can be rearranged and inserted into equation 3.14 together with equation 3.15 to give:

$$I_m = I_o \left(\exp \left(\frac{q(U_m - I_m R_s)}{A_i kT} \right) - 1 \right) + \frac{U_m - I_m R_s}{R_p} - I_{ph} \tag{3.16}$$

Thus the current density for a single diode non – ideal solar cell of area A is given by (El-Tahchi, et. al., 2000; Verschraegen, et. al.,2005):

$$J_m = J_o \left(\exp \left(\frac{q(U_m - J_m R_s)}{A_i kT} \right) - 1 \right) + \frac{U_m - J_m R_s}{R_p} - J_{ph} \tag{3.17}$$

Figure 3.5 shows semi logarithmic plot of short circuit current density as a function of applied voltage, the diagram is usually used in analysing parasitic resistances of photovoltaic devices. Different regions can be distinguished, as shown marked A, B, C and D.

Region A: this region represents the low range of forward bias. In this region, the electronic transport is controlled by the saturation current and shunt resistance.

Region B: in this region, according to equation 3.17, information on diode ideality factor can be extracted at this bias range since it controls the slope in the linear range.

Region C – D: in this region series resistance becomes dominant and deviation from ideal diode is likely (Fuentes-Marron, 2003; Schilinsky, *et.al.* 2004; Sharma, *et. al.*, 2006).

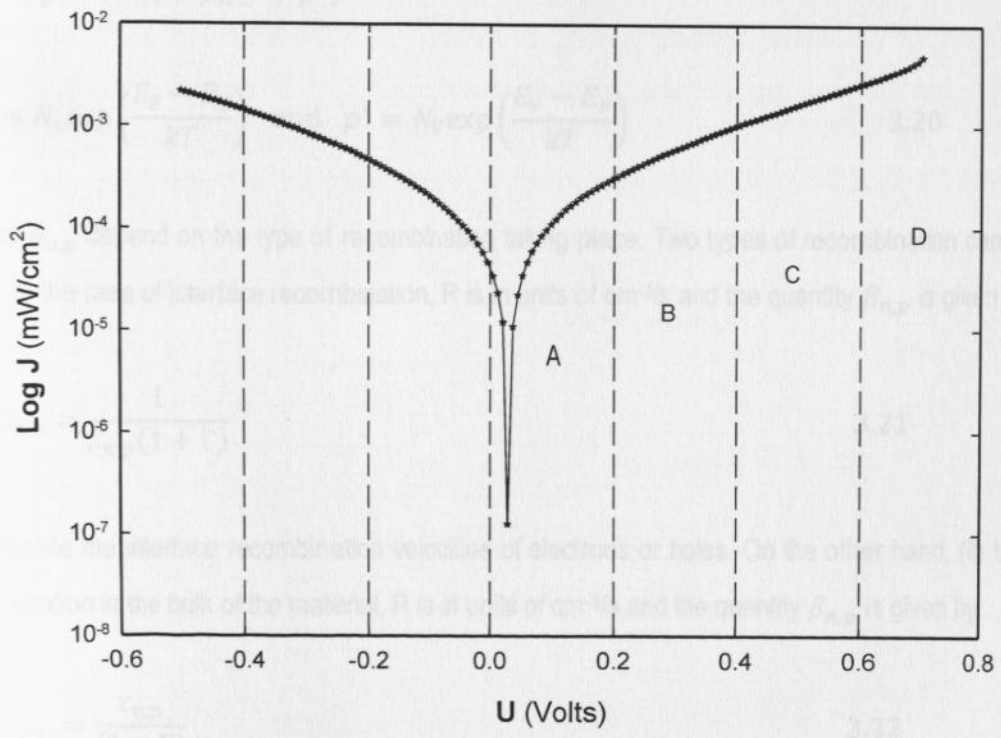


Figure 3.5: Semi logarithmic plot of current density (mW/cm²) of the dark current as function of applied voltage U (volts)

3.2 Transport mechanism theory

Recombination is the loss of an electron or hole through the decay of an electron to a lower energy state. This can be from interband annihilation of an electron - hole pair, or it may be from conduction band to trap state or from trap state to valence band, removing only an electron or hole, respectively. In general the total recombination current is expressed by the following equation (Nelson, 2003):

$$J = q \int R dx \quad 3.18$$

where R is the electron - hole pair recombination rate, and is given by the generalized analytical expression as derived by Hurkx *et. al.*,(1992), Rau *et. al.*, (2000)

$$R = \frac{n_i^2 e^{\frac{qU}{kT}} - n_i^2}{\beta_p(n + n^*) + \beta_n(p + p^*)} \quad 3.19$$

where

$$n^* = N_c \exp\left(\frac{E_F - E_C}{kT}\right) \quad \text{and} \quad p^* = N_v \exp\left(\frac{E_V - E_F}{kT}\right) \quad 3.20$$

The quantities $\beta_{n,p}$ depend on the type of recombination taking place. Two types of recombination can be described: (i) In the case of interface recombination, R is in units of cm^{-2}/s and the quantity $\beta_{n,p}$ is given by:

$$\beta_{n,p} = \frac{1}{S_{n,p}(1 + \Gamma)} \quad 3.21$$

where $S_{n,p}$ denote the interface recombination velocities of electrons or holes. On the other hand, (ii) trap states recombination in the bulk of the material, R is in units of cm^{-3}/s and the quantity $\beta_{n,p}$ is given by:

$$\beta_{n,p} = \frac{\tau_{n,p}}{(1 + \Gamma)} \quad 3.22$$

where $\tau_{n,p}$ is the electron or hole lifetime. In equations 3.21 and 3.22, Γ is a correction factor describing the enhancement of recombination by thermally assisted tunneling and is given by (Rau, *et. al.*, 2000; Nadenau, *et. al.*, 2000):

$$\Gamma = 2\sqrt{3\pi} \frac{|\xi|}{\xi_{\Gamma}} \exp\left(\frac{|\xi|^2}{\xi_{\Gamma}^2}\right) \quad 3.23$$

In the correction factor Γ , the term ξ_{Γ} is given by (Bayhan, 2006; Rau, *et. al.*, 2000)

$$\xi_{\Gamma} = \frac{2\pi[24m^*(kT)^3]^{1/2}}{qh} \quad 3.24$$

with m^* being the effective tunneling mass, ξ is the local electric field at the location of the trap state while h is the Planck's constant. In the limits $\Gamma \rightarrow 0$ then equation 3.19 describes the classical Shockley – Read – Hall (SRH) recombination rate (Shockley and Read, 1952; Hall, 1952).

The model sketched in figure 3.6 describes the dependence of recombination currents on the density of deep defects in the bulk of the material and on the built-in electrical field at the junction (Kaufmann, 2002; Fritsche, *et. al.*, 2002; Rusu, *et. al.*, 2002).

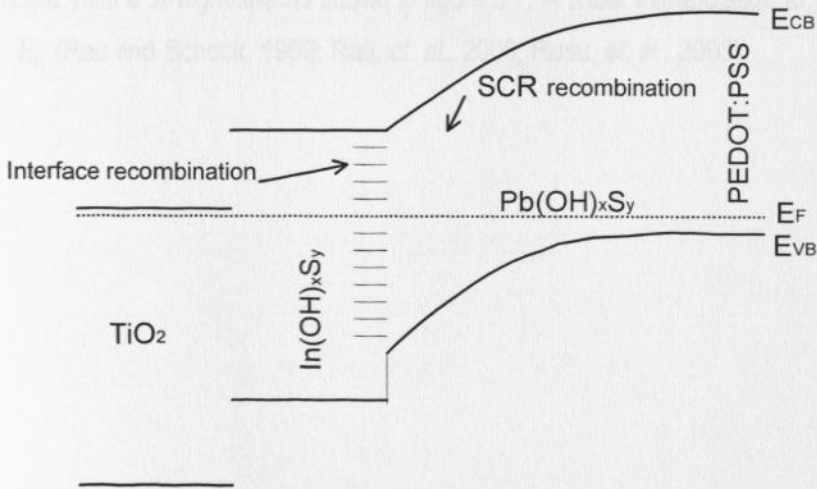


Figure 3.6: Band diagram of the proposed eta solar cell studied in this work. Shown are the main recombination mechanism locations for interface and space charge region (SCR).

The forward recombination current density through recombination centres in the space charge region (SCR) is described by equation 3.25 (Rau, *et. al.*, 2000; Rusu, *et. al.*, 2003; Bayhan and Kavasoğlu, 2005).

$$J = J_o \exp\left(\frac{qU}{A_i kT}\right) = J_{oo} \exp\left(\frac{-E_a}{A_i kT}\right) \exp\left(\frac{qU}{A_i kT}\right) \quad 3.25$$

where A_i is the diode ideality factor, kT/q is the thermal voltage, E_a is the activation energy of the recombination, while J_o and J_{oo} are the diode saturation current density and a weakly temperature dependent prefactor which depends on the transport mechanism (tunneling enhanced or thermally activated recombination mechanisms), respectively (Rau, *et. al.*, 2000; Rusu, *et. al.*, 2003). In view of equation 3.25, the open circuit voltage is given by

$$U_{oc} \approx \frac{A_i kT}{q} \ln\left(\frac{J_{sc}}{J_o}\right) = \frac{E_a}{q} - \frac{A_i kT}{q} \ln\left(\frac{J_{oo}}{J_{sc}}\right) \quad 3.26$$

Equation 3.26 relates open circuit voltage to the activation energy and temperature, therefore, assuming that, A_i , J_{sc} and J_{oo} are independent of temperature, a plot of open circuit voltage, U_{oc} as a function of temperature, T should yield a straight line as shown in figure 3.7. A linear extrapolation to $T = 0$ gives the activation energy, E_a (Rau and Schock, 1999; Rau, *et. al.*, 2000; Rusu, *et. al.*, 2003).

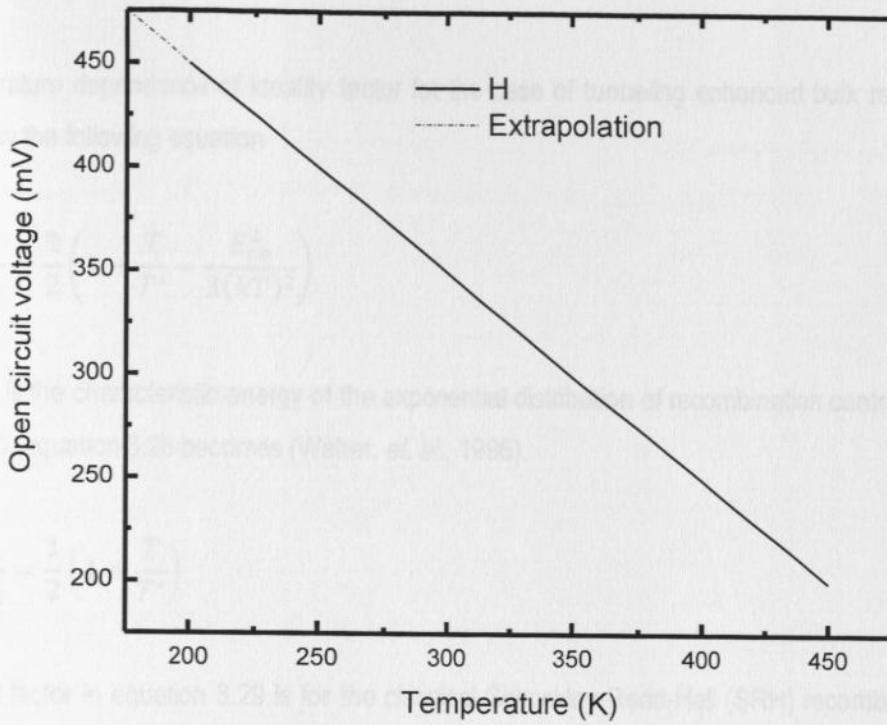


Figure 3.7: Open circuit plot as a function of temperature. Extrapolation used in calculating activation energy is also shown, where H is the plot of equation 3.26.

In eta solar cell, two types of recombination mechanism are possible, tunneling enhanced or thermally activated either at the interface or at the space charge region as already been shown in figure 3.6. When the tunneling process is dominant, equation 3.26 can be reorganised as follows (Rusu, *et. al.*, 2003; Bayhan and Kavasoglu, 2005)

$$\frac{A_i kT}{q} (\ln J_{sc} - \ln J_o) = \frac{E_a}{q} - \frac{A_i kT}{q} (\ln J_{oo} - \ln J_{sc})$$

$$A_i kT \ln J_{sc} - A_i kT \ln J_o = E_a - A_i kT \ln J_{oo} + A_i kT \ln J_{sc}$$

$$A_i \ln J_o = -\frac{E_a}{kT} + A_i \ln J_{oo} \quad 3.27$$

Equation 3.27 predicts that the activation energy E_a of the process can be calculated from the slope of a linear plot of corrected reverse saturation current density $A_i \ln J_o$ as a function of inverse temperature $1/T$.

The temperature dependence of ideality factor for the case of tunneling enhanced bulk recombination is described by the following equation

$$\frac{1}{A_i} = \frac{1}{2} \left(1 + \frac{T}{T^*} - \frac{E_{oo}^2}{3(kT)^2} \right) \quad 3.28$$

where kT^* is the characteristic energy of the exponential distribution of recombination centres. In the limits as $E_{oo} \rightarrow 0$, equation 3.28 becomes (Walter, *et. al.*, 1996).

$$\frac{1}{A_i} = \frac{1}{2} \left(1 + \frac{T}{T^*} \right) \quad 3.29$$

The ideality factor in equation 3.29 is for the classical Shockley-Read-Hall (SRH) recombination through exponential distribution of trap states, whereas, in the limits as $T^* \rightarrow \infty$ equation 3.28 describes the tunneling enhanced recombination via midgap states (Rau, *et. al.*, 2000). On the other hand, the temperature dependence for the tunneling enhanced interface recombination, the diode ideality factor A_i is given by

$$A_i = \frac{E_{oo}}{kT} \coth \left(\frac{E_{oo}}{kT} \right) \quad 3.30$$

A summary of the recombination mechanisms for different scenarios is given in Table 3.1.

Table 3.1: Summary of recombination mechanisms possible in the eta solar cell. Shown are the activation energy of reverse saturation current density, open circuit voltage extrapolation values to $T = 0$ K, and temperature dependence of ideality factor. (Schuller, 2002; Reiss, 2002; Fuertes-Marron, 2003).

Recombination mechanism	Activation energy of J_o	$U_{oc} (T = 0 K)$	Ideality factor, A_i
Bulk	E_g	E_g	1
Thermally activated SCR-single defect level	E_g/A_i	E_g	2
Thermally activated SCR-exponential defect distribution	E_g/A_i	E_g	$\frac{2T^*}{T + T^*}; 1 \leq A_i \leq 2$
Tunneling enhanced SCR	E_g/A_i	E_g	$\frac{1}{2} \left(1 + \frac{T}{T^*} - \frac{E_{oo}^2}{3(kT)^2} \right); A_i \uparrow \text{ as } T \downarrow$
Thermally activated interface	$E_a < E_g$	E_a	$1 + \frac{N_A}{N_D}; 1 \leq A_i \leq 2$
Tunneling enhanced interface	$E_a < E_g$	E_g	$\frac{E_{oo}}{kT} \coth \left(\frac{E_{oo}}{kT} \right); A_i \uparrow \text{ as } T \downarrow$

3.3 Quantum efficiency

The quantum efficiency (QE) is the measure of the number of charge carriers collected by the solar cell to the number of photons of a given wavelength impinging on the solar cell. The QE mainly depends on the following factors: (i) absorption coefficient of the absorber material of the solar cell, (ii) the efficiency of charge separation in the active interface and (iii) the efficiency of charge collection in the device.

The photocurrent generated by a solar cell is given as the probability that an incident photon of wavelength λ will deliver one electron to the external circuit and is described by the following equation (Sze, 1997; Nelson, 2003)

$$J_{sc} = q \int b_s(\lambda) QE(\lambda) d\lambda \quad 3.31$$

where $b_s(\lambda)$ is the incident spectral photon flux density and q is the elementary charge.

The depletion regions width of a solar cell normally changes with applied bias, the quantum efficiency also changes with the built-in voltage across the p – n junction of the device, hence the expression for quantum efficiency when optical losses of the photon flux are put into consideration is given by

$$QE(\lambda, V)_{ext} = \frac{J(\lambda)}{qb_s(\lambda)} \quad 3.32$$

The expression in 3.32 is usually called the external quantum efficiency (EQE). A typical external quantum efficiency diagram is shown in figure 3.8.

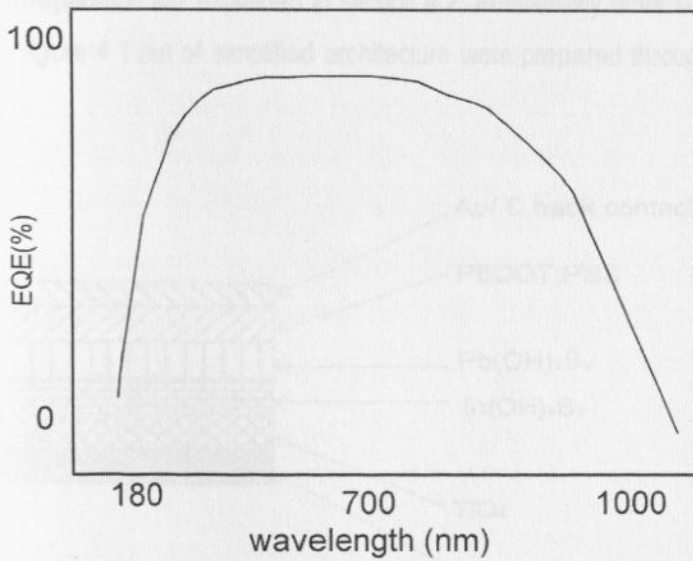


Figure 3.8: Typical diagram of external quantum efficiency performance of a solar cell operated at AM1.5.

CHAPTER 4

Experimental Procedures

4.1 Introduction

The work reported in this thesis, all the samples were prepared on Tech 15 fluorine doped tin oxide glass ($\text{SnO}_2:\text{F}$) with $15 \Omega/\text{cm}^2$ sheet resistance from Pilkington, USA. The other substrates glass used were obtained from Förschungszentrum Jülich GmbH, Germany. Different thin films used in fabricating the sample solar cells were grown following different procedures as explained in section 4.2. The cross sectional structure of the main solar cell is shown in figure 4.1. The solar cells were deposited by staking different thin films as follows: titanium dioxide was first coated on the substrate glass followed by indium hydroxy sulphide thin film, and then a layer of lead hydroxy sulphide was coated on top. Lastly, PEDOT:PSS was deposited and the solar cell was completed by gold back contacts, detailed procedures on each thin film preparation are explained in section 4.2. Additionally other solar cell structures similar to the one shown in figure 4.1 but of simplified architecture were prepared through layer by layer elimination principle.

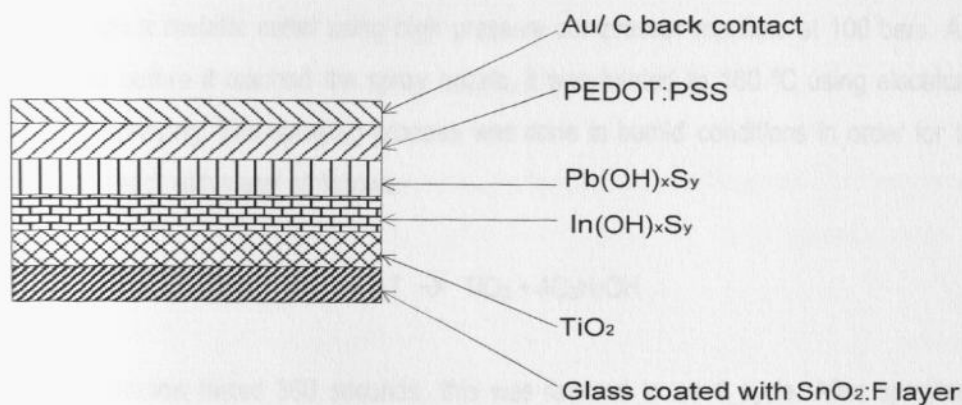


Figure 4.1: Eta solar cell structure fabricated in this work showing stalked thin film layers.

4.2. Samples preparation

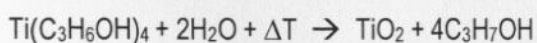
In this section, deposition methods for different layers used in fabricating the eta solar cells are given. Various thin films layers were deposited following diverse procedures and a variety of precursors as explained in the following sub – sections.

4.2.1 Titanium dioxide (TiO₂)

Titanium dioxide thin films used in this work were produced using two different techniques, namely; spray pyrolysis and sol-gel methods. The two methods are explained in the following sub-sections (a) and (b), respectively.

a) Spray pyrolysis

Titanium dioxide thin films coated using spray pyrolysis method were deposited using an automated spray system as shown in figure 4.2. The following procedure was used: 800 µl of tetra-isopropyl orthotitanate (Ti(C₃H₆OH)₄) purchased from Sigma-Adrich™ were mixed with 1 litre of commercial grade solution of isopropanol (CH₃CH(OH)CH₃), obtained from Merck™. The precursor solution was poured into the container of the spray pyrolysis system, labeled precursor as shown in figure 4.2. During the entire duration of spraying process, the precursor solution was kept free from reaction with ambient oxygen by allowing continuous inert argon gas flow into the container (see the argon gas inlet in figure 4.2). The spraying process was controlled by a computerized procedure using a program written in LabVIEW™. The spraying process was preceded by the glass substrate being heated at 450°C for 1800 seconds, and then left to cool down to a controlled temperature maintained at 160°C. The precursor solution was then pumped out of the container through a metallic outlet using high pressure compressor machine at 100 bars. As the solution flowed out, and before it reached the spray nozzle, it was heated to 160 °C using electrical rubberband heater prior to spraying. The spraying process was done in humid conditions in order for tetra-isopropyl orthotitanate to react with water as follows:-



The spraying duration lasted 360 seconds; this was referred to as 1 cycle. After spraying, the coated substrate was then annealed at 450 °C for 1800 seconds in order to remove traces of Ti(OH)₄ and get TiO₂. Different samples of different layer thicknesses were fabricated depending on the number of sprays, whereby 1 spray is equal to 1 cycle of spraying duration of 360 seconds. Samples of 6, 8, 10, 12 and 20 sprays were fabricated. The layer thickness of such samples varied between 2 – 5 µm.

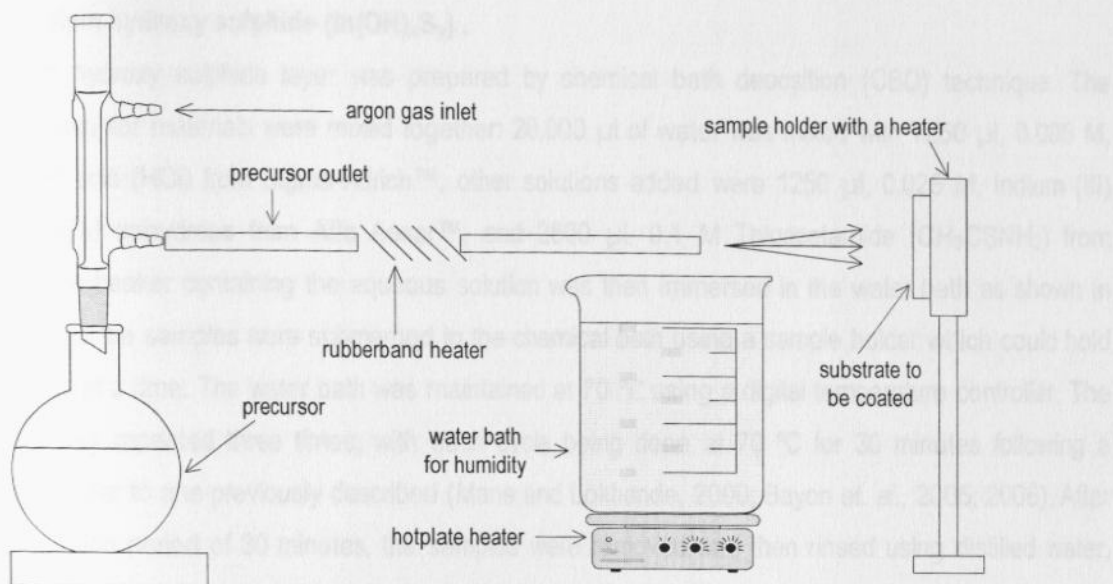


Figure 4.2: Spray pyrolysis system used in fabricating TiO₂ samples. Shown are the precursor container, rubberband heater, humidity source and substrate holder with a heater.

b) Sol-gel technique

Commercially deposited TiO₂ samples were bought ready made from SgLux GmbH. The samples had been coated using sol-gel technique on glass substrates obtained from two different places; a Tech 15 glass coated with fluorine doped tin oxide (SnO₂:F) layer of 15 Ω/cm² sheet resistance from Pilkington, and the other glass also SnO₂:F coated of the same resistance was fabricated at Forschungszentrum Jülich GmbH. The TiO₂ samples were deposited on either 5 × 5, or 10 × 10 cm² sheet of glass.

Other samples prepared through sol-gel technique were compact TiO₂ thin films. The precursors used in preparing the thin films included 15 ml of commercial grade solution of isopropanol (CH₃CH(OH)CH₃) obtained from Merck™, mixed with 800 μl of tetra-isopropyl orthotitanate (Ti(C₃H₆OH)₄) from Sigma-Adrich, the coating was done by dipping the sample in the precursor solution for duration lasting less than 10 seconds.

The samples prepared by either spray pyrolysis, commercially made sol-gel deposited, and the compact layer type were annealed for 30 minutes in air using an oven whose temperature was set at 450 °C and thereafter left to cool down to room temperature before the next procedure could be done.

4.2.2 Indium hydroxy sulphide ($\text{In}(\text{OH})_x\text{S}_y$) .

The indium hydroxy sulphide layer was prepared by chemical bath deposition (CBD) technique. The following precursor materials were mixed together: 20,000 μl of water was mixed with 1250 μl , 0.005 M, hydrochloric acid (HCl) from Sigma-Adrich™, other solutions added were 1250 μl , 0.025 M, Indium (III) chloride (InCl_3) anhydrous from Alfa Aesar™, and 2500 μl , 0.1 M Thioacetamide (CH_3CSNH_2) from Adrich™. The beaker containing the aqueous solution was then immersed in the water bath as shown in figure 4.3, and the samples were submerged in the chemical bath using a sample holder which could hold four samples at a time. The water bath was maintained at 70 °C using a digital temperature controller. The deposition was repeated three times, with each cycle being done at 70 °C for 30 minutes following a procedure similar to one previously described (Mane and Lokhande, 2000; Bayon *et. al.*, 2005; 2006). After every deposition period of 30 minutes, the samples were removed and then rinsed using distilled water, then fresh solution was prepared and the procedure was repeated. The samples thereafter were annealed in argon atmosphere at 300 °C for 30 minutes. After annealing, the samples were left to cool down to room temperature before any other process could be done. The setup used is shown in figure 4.3.

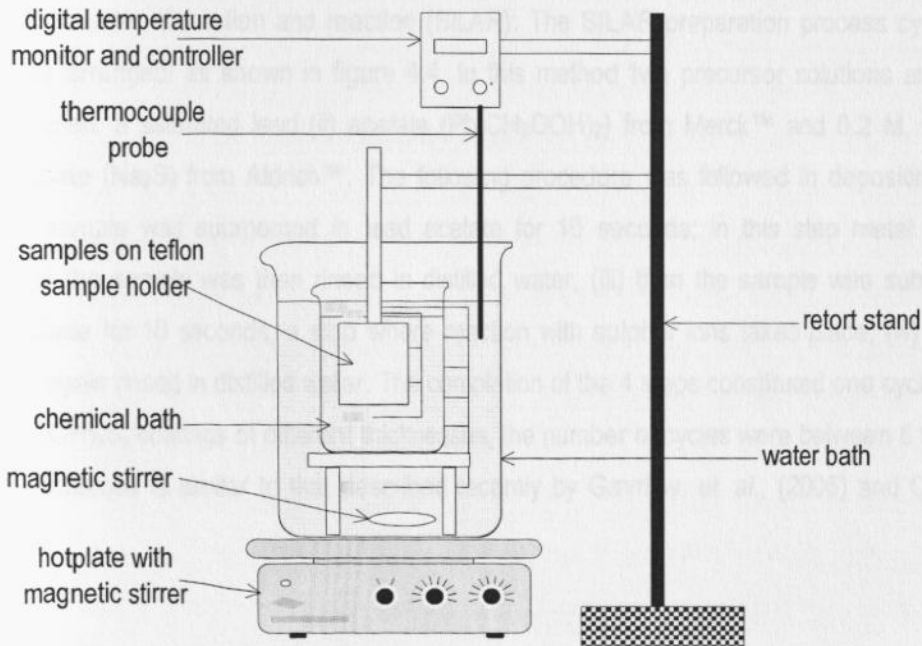


Figure 4.3: Set up for chemical bath deposition used in depositing $\text{In}(\text{OH})_x\text{S}_y$ and $\text{Pb}(\text{OH})_x\text{S}_y$, respectively.

4.2.3 Lead hydroxy sulphide ($\text{Pb}(\text{OH})_x\text{S}_y$)

The lead hydroxy sulphide ($\text{Pb}(\text{OH})_x\text{S}_y$) thin film layers were grown using either of the two methods described below:

- a) Chemical bath deposition (CBD): The setup used was the same as the one used in depositing $\text{In}_x(\text{OH})_y\text{S}_z$ described in section 4.2.2 and shown in figure 4.3. The samples were prepared using aqueous solution containing the following precursors: 2500 μl solution of 0.05 M lead (ii) acetate ($\text{Pb}(\text{CH}_3\text{OOH})_2$) obtained from Merck™ was mixed with, 5000 μl of 0.2 M solution of sodium hydroxide (NaOH) from Merck™, 1250 μl of 0.05 M solution of triethanolamine ($\text{C}_6\text{H}_{15}\text{NO}_3$) from Merck™, and 1250 μl of 0.05 M solution of thiourea (NH_2CSNH_2) from Aldrich™. These solutions were diluted with 15000 μl of distilled water. The beaker containing the aqueous solution was then immersed in the water bath as earlier shown in figure 4.3, thereafter, the samples pasted on Teflon sample holder were submerged in the chemical bath. The chemical bath deposition was done at 40 °C for 10 minutes, following a similar procedure as reported elsewhere (Bayon. *et. al.*, 2005; 2006). After deposition, the samples were then rinsed in distilled water (NB: the molar values given are for the final solution and not the stock solution).
- b) Successive ion layer absorption and reaction (SILAR): The SILAR preparation process cycle was in four steps as arranged/ as shown in figure 4.4. In this method two precursor solutions and distilled water were used: a saturated lead (ii) acetate ($\text{Pb}(\text{CH}_3\text{OOH})_2$) from Merck™ and 0.2 M, solution of sodium sulphate (Na_2S) from Aldrich™. The following procedure was followed in depositing the thin film: (i) the sample was submerged in lead acetate for 10 seconds; in this step metal ions were adsorbed, (ii) the sample was then rinsed in distilled water, (iii) then the sample was submerged in sodium sulphate for 10 seconds, a step where reaction with sulphur ions takes place, (iv) finally the sample was again rinsed in distilled water. The completion of the 4 steps constituted one cycle. In order to obtain $\text{Pb}(\text{OH})_x\text{S}_y$ coatings of different thicknesses, the number of cycles were between 6 to 10. This deposition technique is similar to that described recently by Gavrilov, *et. al.*, (2006) and Oja, *et. al.*, (2006).

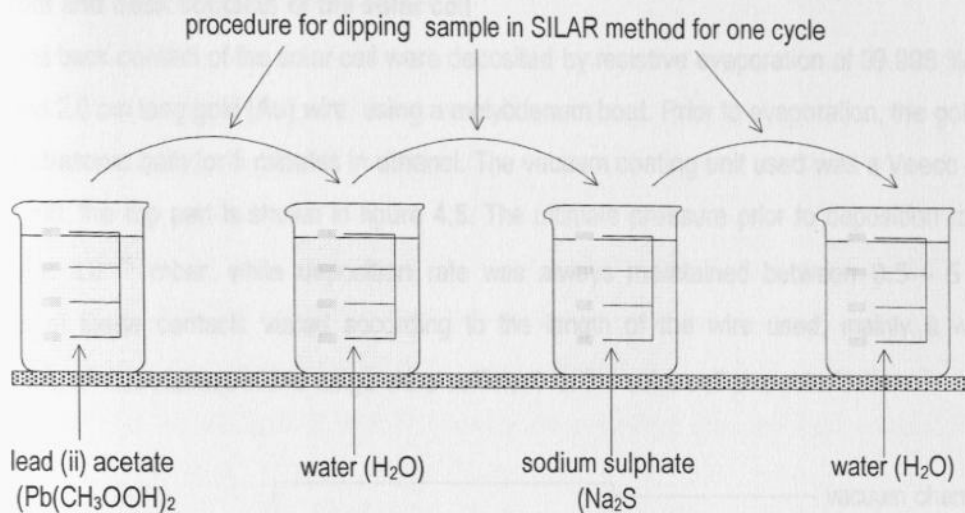


Figure 4.4: Illustration of SILAR technique for coating samples; the 4 steps represents one cycle.

4.2.4 Poly(3,4-ethylenedioxythiophene) polystyrene sulfonate (PEDOT:PSS)

Different types of poly(3,4-ethylenedioxythiophene) polymer doped with polystyrene sulfonate acid (PEDOT: PSS) are commercially available from Bayer™ GmbH. Three types were used during the course of doing this work, that is, PEDOT:PSS Baytron P, PEDOT:PSS Baytron formula, and PEDOT:PSS Baytron PH. Spin coating technique was used in depositing the polymer material. The spin coater used was Astrocel II BLE Delta 10, housed in a movable clean room from MCRT™, GmbH. The sample was prepared by placing it on the spin coater and then the polymer material was applied by special dropper with a filter at the front tip. The filters with 0.45 μm pores were obtained from Millex Millipore, USA. Deposition speeds of the spin coater were preset at different speeds as follows: immediately after starting the spinning process, the spin coater was set to rotate at 100 rpm (revolution per minute) for 5 seconds, then accelerated to 500 rpm for 5 seconds, and thereafter to a speed of 2000 rpm for 60 seconds, then decelerated in two steps by decreasing speed to 500 rpm for 5 seconds and 100 rpm for 3 seconds, respectively before coming to stand still. Prior to spin coating, the PEDOT:PSS material was agitated in an ultrasonic bath for 15 hours continuous, this helped in producing an even coating and clustering of the material was avoided. After coating, the samples were then heated for 7 minutes in air on a hot plate at whose temperature had been set at 80 °C, this helped in drying up the samples after the wet deposition.

4.2.5 Front and back contacts of the solar cell

The front and back contact of the solar cell were deposited by resistive evaporation of 99.998 % purity, 1.5 mm thick and 2.0 cm long gold (Au) wire, using a molybdenum boat. Prior to evaporation, the gold wire was cleaned in ultrasonic bath for 5 minutes in ethanol. The vacuum coating unit used was a Veeco Instrument model EC-200, the top part is shown in figure 4.5. The ultimate pressure prior to deposition ranged from $1.5 - 2.0 \times 10^{-5}$ mbar, while deposition rate was always maintained between $0.5 - 5 \text{ \AA/s}$. The thicknesses of these contacts varied according to the length of the wire used, mainly it was around $0.8 - 1.8 \text{ k\AA}$, all thicknesses in this range were sufficient for the solar cell characterization.

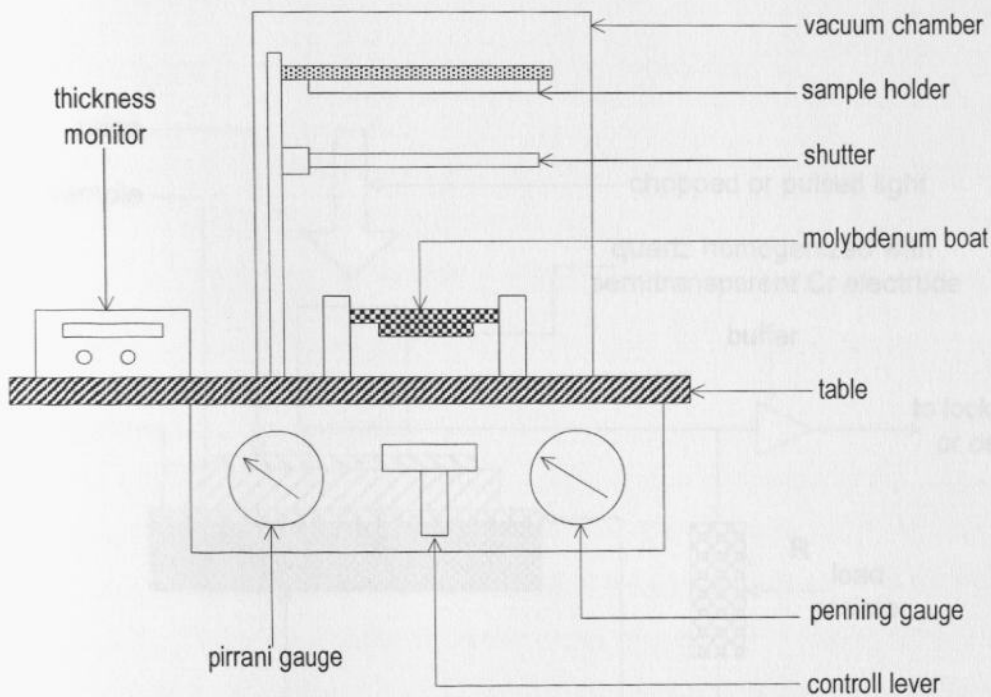


Figure 4.5: Block diagram showing the top part of the vacuum coating system used in depositing front and back contact.

4.3. Characterization of the thin films

The thin films prepared following procedures explained in section 4.2, were characterized using different analysis techniques for: morphological, structural, optical and optoelectrical properties. The methods used are explained in the following sub-sections.

4.3.1 Surface photovoltage (SPV) spectroscopy

Photovoltage spectroscopy measurements were done using a setup consisting of: EG&G Princeton applied research type 5210 lock-in amplifier, Carl-Zeiss monochromator type 408069 (from former Germany DDR), and HMS light beam chopper type 220 for regulating signal frequency with maximum revolution speed of 6000 rpm. The measurement cell shown in figure 4.6, consists of quartz homogenizer coated with semitransparent chrome (Cr) electrode, separated from the sample to be measured by a 50 μm thick mica spacer. The function of the quartz homogenizer is to support the chrome electrode and also prevent shunting due to the un-illuminated areas of the capacitor formed. The surface photovoltage (SPV) signal was measured using oscilloscope or lock-in amplifier as a voltage drop on load resistor R (Duzhko, *et.al.*,2002).

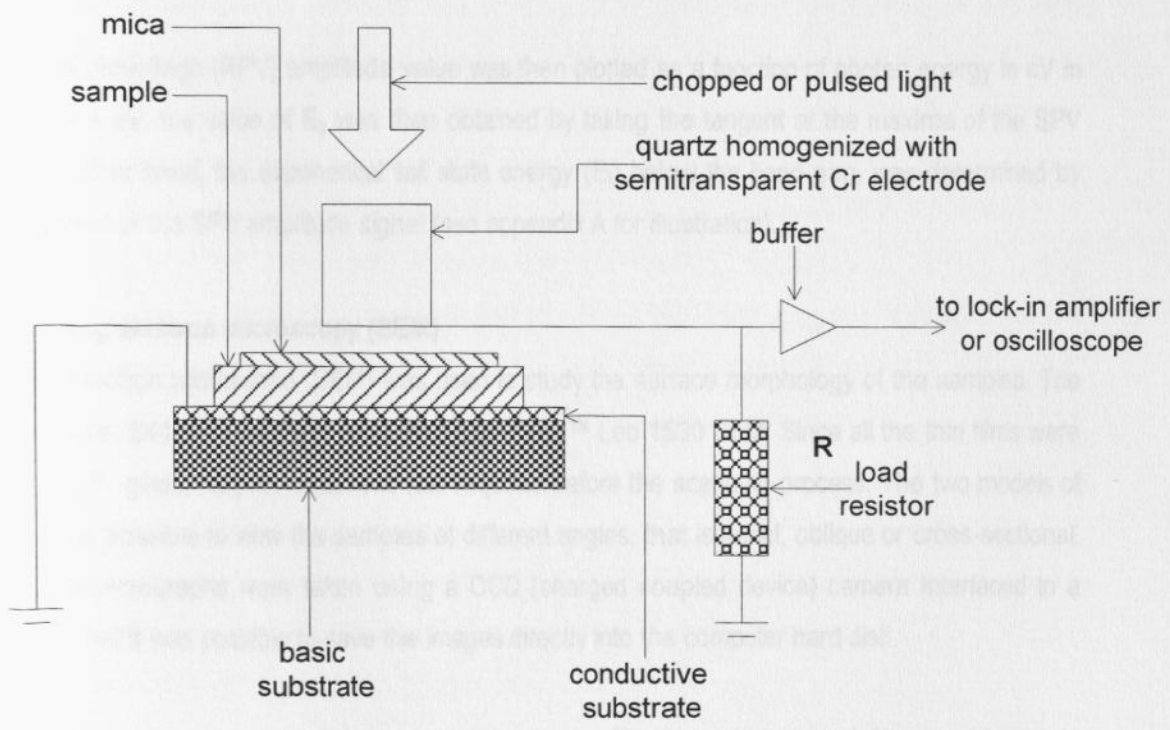


Figure 4.6: The samples' measurement section of the surface photovoltage spectroscopy setup used for determining band gap and tail state energy below the band gap.

In order to allow free flow of charge carriers, all the samples for surface photovoltage spectroscopy measurements were prepared on fluorine doped tin oxide coated glass substrates. The sample to be

measured was mounted on the basic substrate holder and mica was placed on top as shown in figure 4.6. The SPV spectra were mainly measured in the range between 0.4 and 4 eV at chopping frequency of 8 Hz, using a halogen lamp as the light source. The SPV technique was used to determine the band gap (E_g) of the semiconductor materials used in fabricating the eta solar cell. Since the band gap of a semiconductor material is not abrupt, the surface photovoltage method was also used in determining exponential tail state energy (E_t) below the band gap. The two values were determined using the following methods: for the case of the band gap, the square root of the sum of the squares of the in-phase and 90° out - of - phase signal was computed using the following formula:

$$RPV = \sqrt{a^2 + b^2} \quad 4.1$$

where a is the in - phase and b is the 90° out - of - phase signals, respectively.

The resultant photovoltage (RPV) amplitude value was then plotted as a function of photon energy in eV in the range 0.4 – 4 eV, the value of E_g was then obtained by taking the tangent at the maxima of the SPV signal. On the other hand, the exponential tail state energy (E_t) below the band gap, was determined by taking the gradient of the SPV amplitude signal (see appendix A for illustration).

4.3.2 Scanning electron microscopy (SEM)

The Scanning electron microscope (SEM) was used to study the surface morphology of the samples. The models used were: S4100 HITACHI™ SEM, and Carl Zeiss™ Leo 1530 SEM. Since all the thin films were coated on SnO₂:F glass, no prior treatment was required before the scanning process. The two models of SEM used it was possible to view the samples at different angles, that is aerial, oblique or cross-sectional. The SEM photomicrographs were taken using a CCD (charged coupled device) camera interfaced to a computer such that it was possible to save the images directly into the computer hard disk.

Different scanning electron micrographs were taken at magnifications that ranged from × 10,000 to × 200,000, and at various acceleration voltages of the SEM which were mainly from 5000 V to 10,000 V. The thin films analysed using SEM technique were sol – gel and spray pyrolysis deposited titanium dioxide (TiO₂), chemical bath deposited indium hydroxy sulphide (In(OH)_xS_y) and lead hydroxy sulphide (Pb(OH)_xS_y) thin films, respectively.

4.3.3 Energy dispersive X-ray (EDX) spectroscopy

The material composition in the cross sectional layer structure of the completed solar cell was studied using Energy Dispersive X-ray (EDX) mapping. The procedure used in EDX mapping was by exciting particular elemental component in a specific thin film layer, for example, for TiO_2 , the element excited was titanium, for Indium hydroxyl sulphide, it was indium, etc. The energy dispersive X-ray mapping spectroscopy was done using S4100 HITACHI™ SEM. The model of the SEM has an extra accessory for EDX mapping spectroscopy as an auxiliary unit. The mapping were performed for a completed solar cell of the type $\text{SnO}_2:\text{F}/\text{TiO}_2/\text{In}(\text{OH})_x\text{S}_y/\text{Pb}(\text{OH})_x\text{S}_y/\text{PEDOT:PSS}/\text{Au}$.

4.3.4 X-ray photoelectron spectroscopy (XPS) and X-ray Auger electron spectroscopy (XAES)

Structural properties of $\text{Pb}(\text{OH})_x\text{S}_y$ and $\text{In}(\text{OH})_x\text{S}_y$ were studied using X-ray photoelectron spectroscopy (XPS) and X-ray Auger electron spectroscopy (XAES). The samples studied were of the type $\text{In}(\text{OH})_x\text{S}_y/\text{SnO}_2:\text{F}$ and $\text{Pb}(\text{OH})_x\text{S}_y/\text{In}(\text{OH})_x\text{S}_y/\text{SnO}_2:\text{F}$, with the latter sample being meant for $\text{Pb}(\text{OH})_x\text{S}_y$ analysis. The idea of using $\text{In}(\text{OH})_x\text{S}_y$ as substrate under-layer was mainly because it was not possible to deposit $\text{Pb}(\text{OH})_x\text{S}_y$ material on bare $\text{SnO}_2:\text{F}$ coated glass by chemical bath technique. The XPS/XAES spectroscopies were done using VG CLAM4™ X-ray spectrophotometer. The materials composition of the chemical bath deposited thin films were analysed from the resulting spectrums of $\text{Pb}(\text{OH})_x\text{S}_y$ and $\text{In}(\text{OH})_x\text{S}_y$, respectively. Further studies on stoichiometry of $\text{Pb}(\text{OH})_x\text{S}_y$ layer were done by calibrating the spectrometer such that the reference to Cu 3p line, the Au $4f_{7/2}$ line, the Auger electron Cu L_{3MM} line and the Cu $2P_{3/2}$ line appeared at 75.13, 84.00, 334.95 and 932.67 eV, respectively.

4.3.5 Optical transmittance and reflectance

The samples were characterized for optical transmittance and reflectance at room temperature using a Cary 500 UV – VIS – NIR spectrophotometer. The wavelength range scanned was 180 nm – 900 nm coinciding with the peak spectrum used in analyzing the solar cells.

The standards used in calibrating the spectrophotometer were mainly float glass microscope glass slide for the case of transmittance and a barium sulphate coated standard for the case of reflectance measurements.

4.4. Characterization of the solar cell

Different types of solar cells with dissimilar number of layers were analysed using current density – voltage (J – U) characterization at room temperature, and illumination intensity and temperature dependent J – U characteristics. The incident photon contribution was also studied by quantum efficiency measurements. Details of the study are given in the following sub-sections.

4.4.1 Room temperature current – voltage (J - U) characterization

The quality of solar cell is determined by studying its photovoltaic parameters. The current density – voltage (J - U) characterization is the most commonly used tool for analysis of solar cell devices.

The room temperature J – U characterizations were done both in the dark and under illumination using a set up shown in figure 4.7 consisting of: DC source meter type Keithley™ 237 high voltage source unit connected to a Hewlett Packard™ 34401A multimeter. A halogen lamp (General Electric™, 120 V, 300 W, type L268) was used as light source of the calibrated solar simulator (calibration: AM1.5, 100 mW/cm² = 1 sun). The front and back contact used in connecting to the terminals of the solar cell were in four point probe configuration, such that each terminal of the solar cell was connected to two point probes.

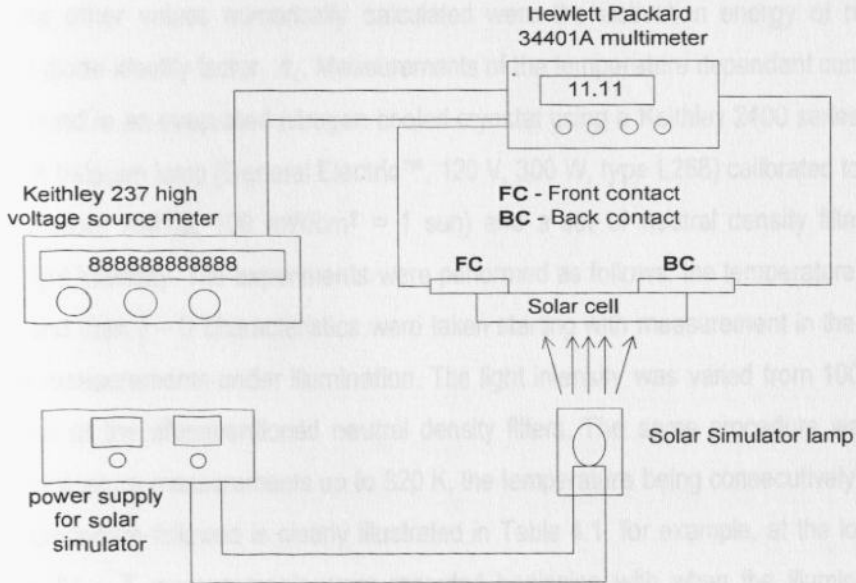


Figure 4.7: Block diagram of the current - voltage characterization set up.

Different p – n junction types of devices have different ways of biasing, in our case, during the characterization process, the solar cell was connected front contact to negative and back contact to positive. Before commencing measurements, a number of values useful for solar cell parameter measurement as well as calculation were keyed in the software used in controlling the set up, these included: start value voltage, end value voltage, number of data points and the area of the solar cell. The solar simulator light was illuminated from below, that is, the glass side of the solar cell in superstrate configuration. The measurements were first done in the dark and then under illumination.

The light soaking analysis was done by first taking J – U characteristics for as - prepared solar cell, and then without disconnecting the front and back contact probes, the solar cell was maintained under illumination from 0 - 180 minutes, with J – U measurements being done at intervals of either 15 minutes or 30 minutes.

4.4.2 Intensity and temperature dependent current – voltage (JU – T) characterization

The current transport mechanism of the solar cell were analysed by intensity and temperature dependent current – voltage (JU - T) characterization. This method helped in understanding the generation and recombination mechanism of the eta solar cell of the structure proposed in this thesis. Apart from solar cell parameters, the other values numerically calculated were the activation energy of reverse saturation current, J_o and diode ideality factor, A_i . Measurements of the temperature dependent current – voltage (JU -T) were performed in an evacuated nitrogen cooled cryostat using a Keithley 2400 series current - voltage source meter. A halogen lamp (General Electric™, 120 V, 300 W, type L268) calibrated to illuminate at 100 mW/cm² (calibration: AM1.5, 100 mW/cm² = 1 sun) and a set of neutral density filters were used for adjusting the light intensity. The experiments were performed as follows: the temperature was first lowered to T = 200 K, and then J – U characteristics were taken starting with measurement in the dark, followed by 12 successive measurements under illumination. The light intensity was varied from 100 mW/cm² to 0.05 mW/cm² by use of the aforementioned neutral density filters. The same procedure was applied for the successive temperature measurements up to 320 K, the temperature being consecutively changed in steps of 10 K. The procedure followed is clearly illustrated in Table 4.1, for example, at the lowest temperature 200 K, twelve JU – T measurements were recorded beginning with when the illumination was at 100 mW/cm², then the light intensity was decreased in the following order to 70 mW/cm², followed by 50, 25, 10, 5, 2.5, 1.0, 0.50, 0.25, 0.1 and lastly 0.05 mW/cm². After that, the temperature was increased to 210 K,

and same procedure repeated for 12 JU – T measurements, in total, 156 JU – T measurements were done for the solar cell, as shown in Table 4.1.

Table 4.1 Tabulated format of the procedure followed in performing intensity and temperature dependent JU – T characterization. Inner numbers shown in dark cells show the count.

		Temperature in degrees Kelvin													
		200	210	220	230	240	250	260	270	280	290	300	310	320	
Light intensity in mW/cm ²	100	1	2	3	4	5	6	7	8	9	10	11	12	13	
	70	2													
	50	3													
	25	4													
	10	5													
	5	6													
	2.5	7													
	1.0	8													
	0.50	9													
	0.25	10													
	0.10	11													
	0.05	12												156	

4.4.3 External quantum efficiency (EQE)

The external quantum efficiency was measured using a setup consisting of: 2 units of EG&G instruments model 7260 DSP Lock-in amplifier, Keithley 438 current amplifier, Keithley 236 source measure unit, and HMS light beam chopper 220 with frequency ability up to 6000 rpm, the setup connection is shown in figure 4.7. The monochromator limitation was to scan the wavelength from 180 nm – 980 nm. The EQE setup is calibrated in such a way that after connecting the front and back contact of the solar cell, measurements can commence without requirement to specify area of the device being analysed. The monochromatic light illuminates the sample from the back (glass side) as shown in figure 4.7.

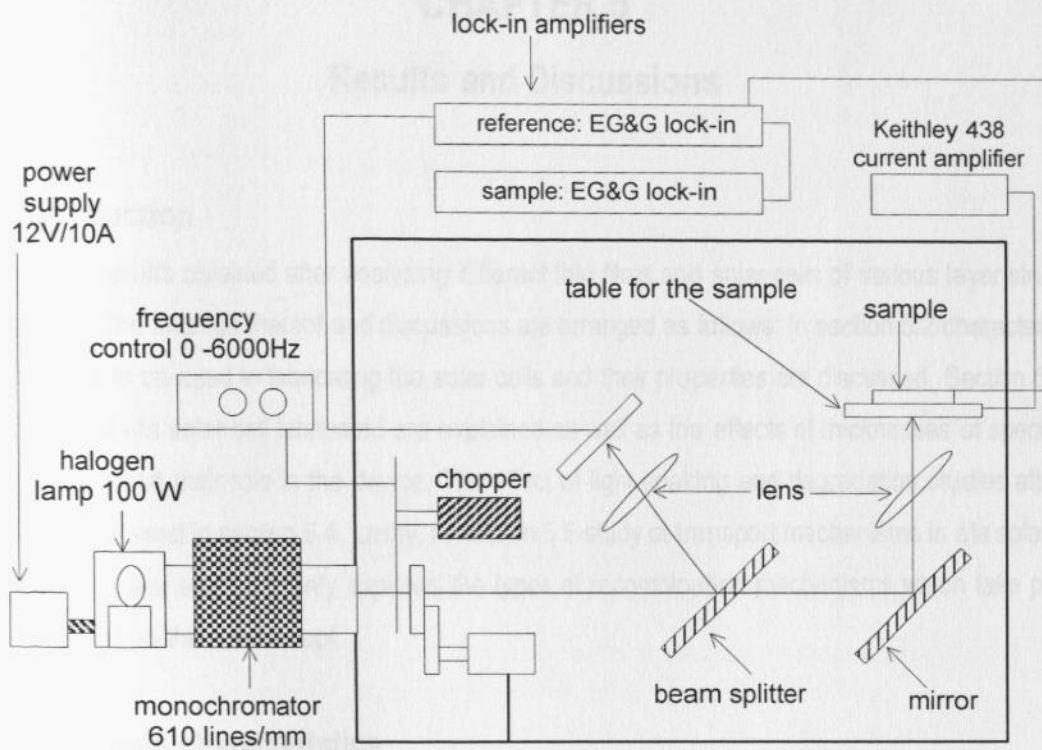


Figure 4.8: External quantum efficiency (EQE) set up used in characterizing the solar cells.

CHAPTER 5

Results and Discussions

5.1 Introduction

In this chapter results obtained after analysing different thin films and solar cells of various layer structures are presented. The findings thereof and discussions are arranged as follows: In section 5.2 characterization of the thin films to be used in fabricating the solar cells and their properties are discussed. Section 5.3, the properties of the eta solar cell fabricated are explained as well as the effects of thicknesses of specific thin film layers used and their role in the device. The effect of light soaking and degradation studies after light soaking are discussed in section 5.4. Lastly, in section 5.5 study of transport mechanisms in eta solar cell is expounded. The last section mainly explores the types of recombination mechanisms which take place in solar cells based on the eta concept.

5.2 Thin films characteristics

Thin films grown using a specific method have unique properties as a result of for example: (i) the intrinsic characteristics of deposition procedure (compare morphology of TiO_2 deposited by spray pyrolysis and sol-gel technique), (ii) properties of the underlying substrate material (effects of epitaxial growth), or (iii) the concentration of the precursor materials used (on the effects of band gap). It is important to understand these distinctive characteristics of the thin films meant for fabricating solar cells since they affect the overall behaviour of the device. It is in this regard the following subsections characteristics of the thin films used in this work are explained.

5.2.1 Surface morphology of titanium dioxide (TiO_2)

Figures 5.1 and 5.2 are photomicrographs showing the surface morphologies of spray pyrolysis deposited titanium dioxide (TiO_2) thin films magnified at $\times 30,000$ and $\times 10,000$, respectively. It is observed that for thin films deposited by spray pyrolysis technique, the top surface has a highly structured microporous and canyon-like structure. The photomicrograph in figure 5.2 taken at an angle reveals that, the thin film grows with a characteristic compact layer at the contact between the film and the fluorine doped tin oxide ($\text{SnO}_2:\text{F}$) coating on the glass substrate, while at the surface it is highly porous.

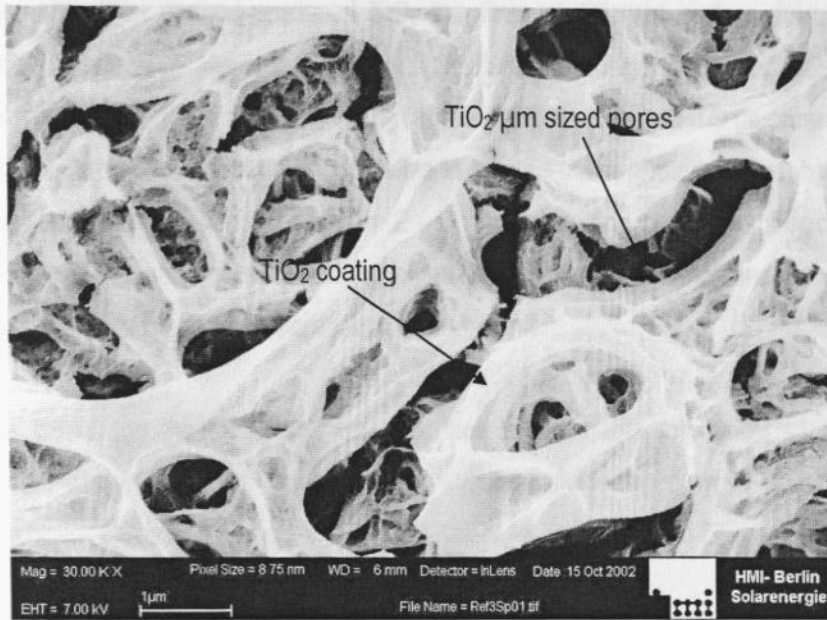


Figure 5.1: Scanning electron micrograph of TiO_2 deposited by spray pyrolysis, magnified at $\times 30,000$. The arrows show the TiO_2 coating and the micrometer (μm) sized pores.

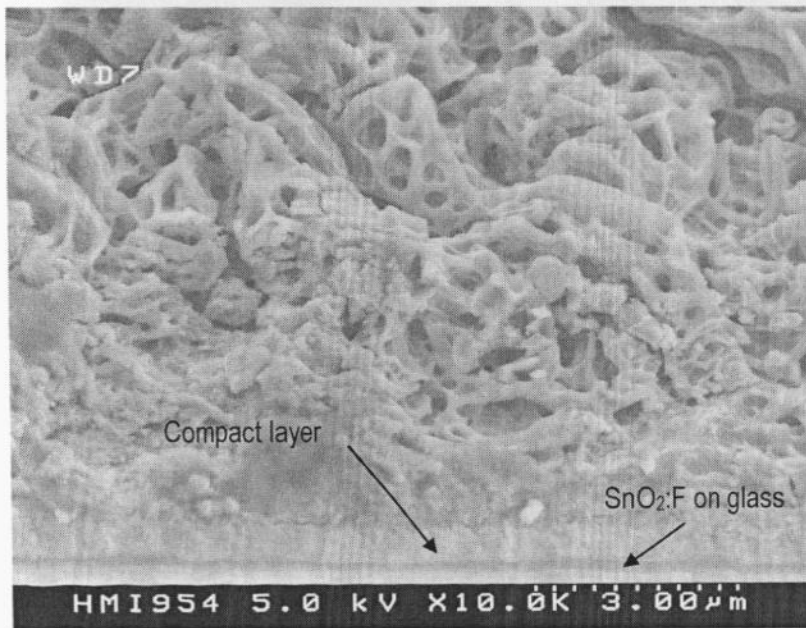


Figure 5.2: Scanning electron micrograph of spray pyrolysis deposited TiO_2 magnified at $\times 10,000$. The arrows point at the compact layer in contact with $\text{SnO}_2:\text{F}$ coating on glass (Belaidi, 2004).

The sol – gel deposition method produced TiO₂ thin films of different surface morphology compared to those deposited by spray pyrolysis as shown in figure 5.3. The sol-gel deposited TiO₂ thin film is a highly structured and cauliflower-like at the surface, but at the interface with the FTO (fluorine doped tin oxide) it is compact and nonporous (compact layer not visible in this top-down photomicrograph). The local thickness of the sol-gel deposited TiO₂ ranged between 2 – 3 μm, depending on the number of coating dips in the solution. The thickness was measured using alpha step thickness monitor and/ or estimated by use of scanning electron microscopy cross-sectional measurements.

In solar cells fabrication the highly structured surface is favourable for optical light trapping due to its inherent porous surface, specular reflectance is substantially reduced while at the same time diffuse reflectance is highly enhanced (Ernst, *et. al.*,2001; Kaiser, *et. al.*,2001; and Levy – Clement, *et. al.*,2002).

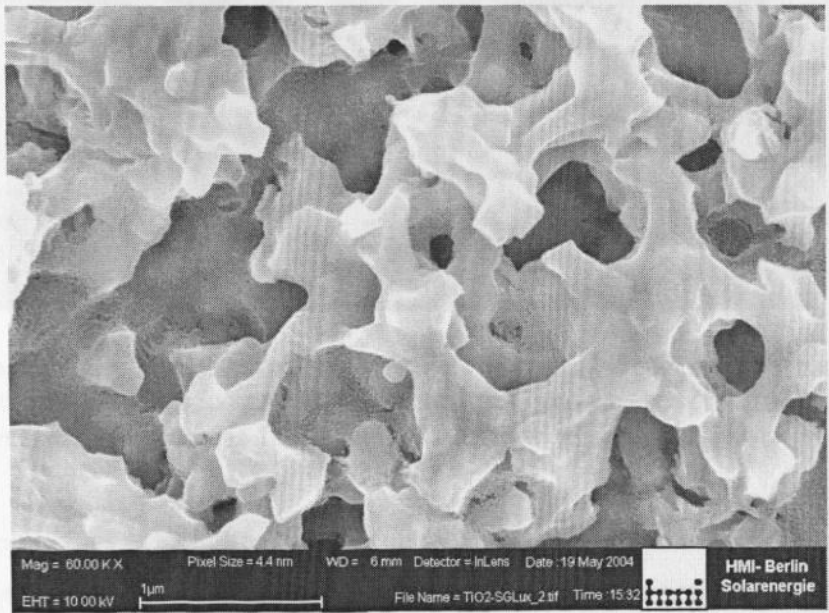


Figure 5.3: Scanning electron micrograph of commercial sol - gel deposited TiO₂ magnified at ×60,000. Deposition was done at Sg - Lux GmbH, Berlin, Germany, (Sg – Lux, 2003).

The highly structured microporous surface is the key feature desirable in eta solar cell since it serves to increase the surface area for light photon harvesting, therefore making it possible to decrease the thickness of the absorber material by the same factor of the surface enlargement.

Figure 5.4 shows a 100 nm thick sol-gel deposited compact TiO_2 thin film magnified at $\times 200,000$. It is observed that, the coating is nonporous and homogeneous; both at the top surface and at the contact with the interface of the FTO. Typical thickness of compact TiO_2 film is $< 1 \mu\text{m}$. Unlike porous TiO_2 the compact layer thin film plays a different role in solar cell fabrication. It acts as blocking layer and therefore improves the rectifying behaviour and overall photovoltaic properties of the solar cell (Peng, et. al., 2004).

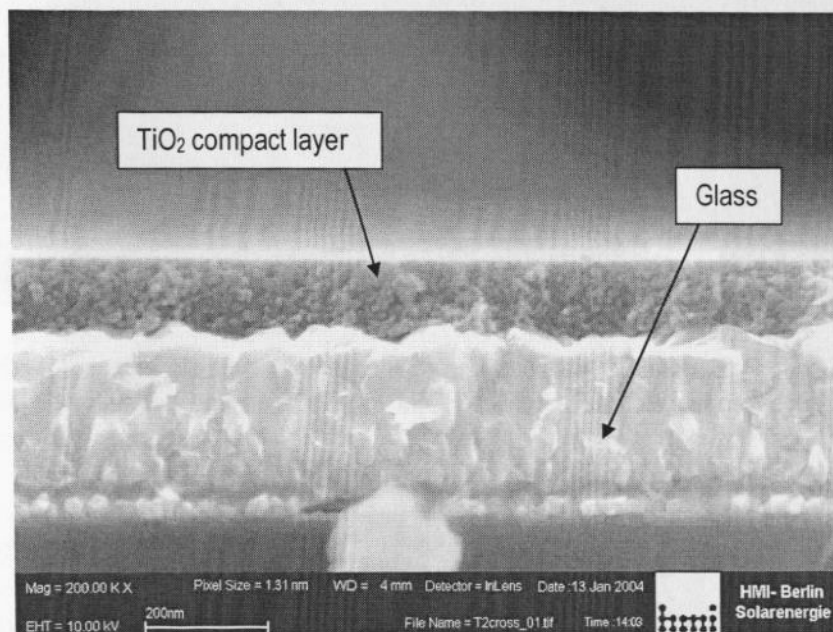


Figure 5.4: Scanning electron micrograph of sol - gel deposited compact TiO_2 magnified at $\times 200,000$. The arrows points at TiO_2 compact thin film coating and glass substrate. The $\text{SnO}_2:\text{F}$ coating between TiO_2 and glass is not clearly discernable.

5.2.2 Surface morphology of Indium hydroxy sulphide ($\text{In}(\text{OH})_x\text{S}_y$)

The photomicrographs in figures 5.5 and 5.6 show morphologies of chemical bath deposited (CBD) - indium hydroxy sulphide thin films. Figure 5.5 is for the case of one cycle coating and is observed to grow in form of spherical cluster islands on titanium dioxide substrate. On further deposition of $\text{In}(\text{OH})_x\text{S}_y$, clusters coalesce together to form linear or spherical growth as shown in figure 5.6. The $\text{In}(\text{OH})_x\text{S}_y$ film deposited in three cycles shows a highly structured surface, which is compact at the interface with the glass substrate,

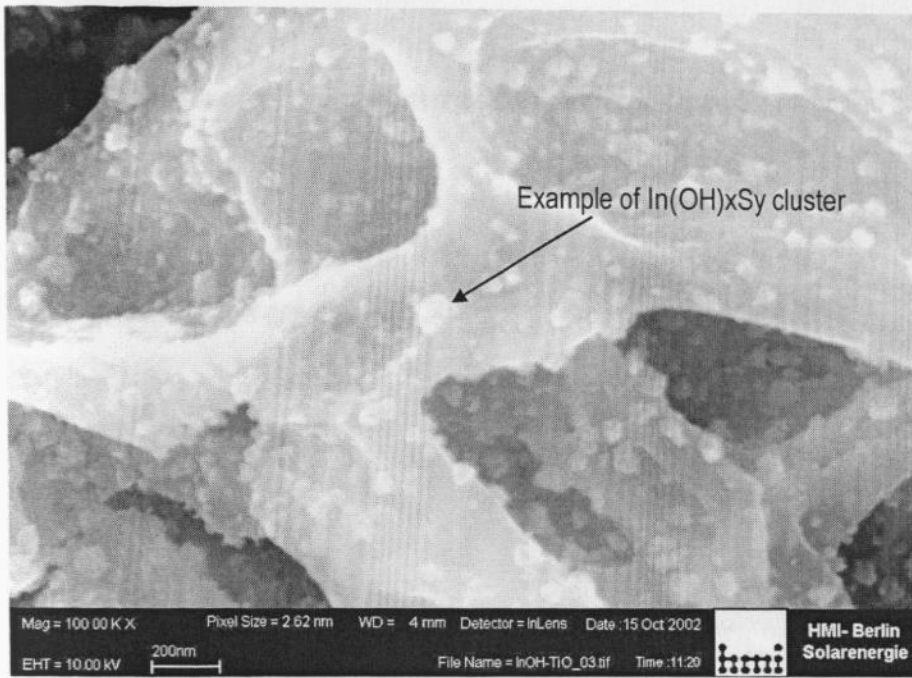


Figure 5.5: Scanning electron micrograph for as deposited CBD- $\text{In(OH)}_x\text{S}_y$ and magnified at $\times 100,000$, arrow shows typical cluster of $\text{In(OH)}_x\text{S}_y$ for a sample deposited on TiO_2 coated substrate in one cycle.

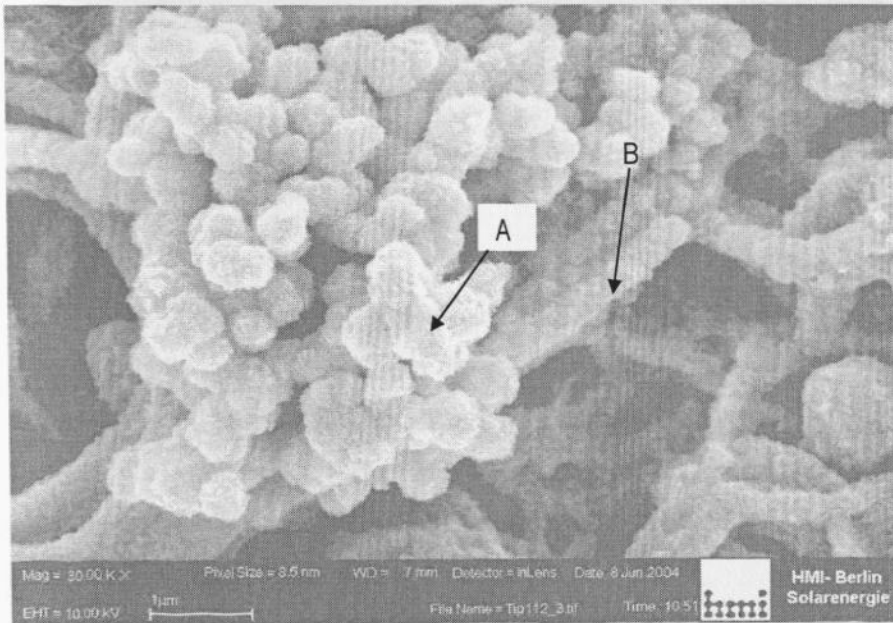


Figure 5.6: Scanning electron micrograph for as deposited CBD- $\text{In(OH)}_x\text{S}_y$ and magnified at $\times 100,000$. The sample was deposited on TiO_2 coated glass substrate in three cycles. Arrow A shows spherical growth while B points at linear growth.

and nanoporous at the top surface, the compact structure is shown in figure 5.7 magnified at $\times 100,000$.

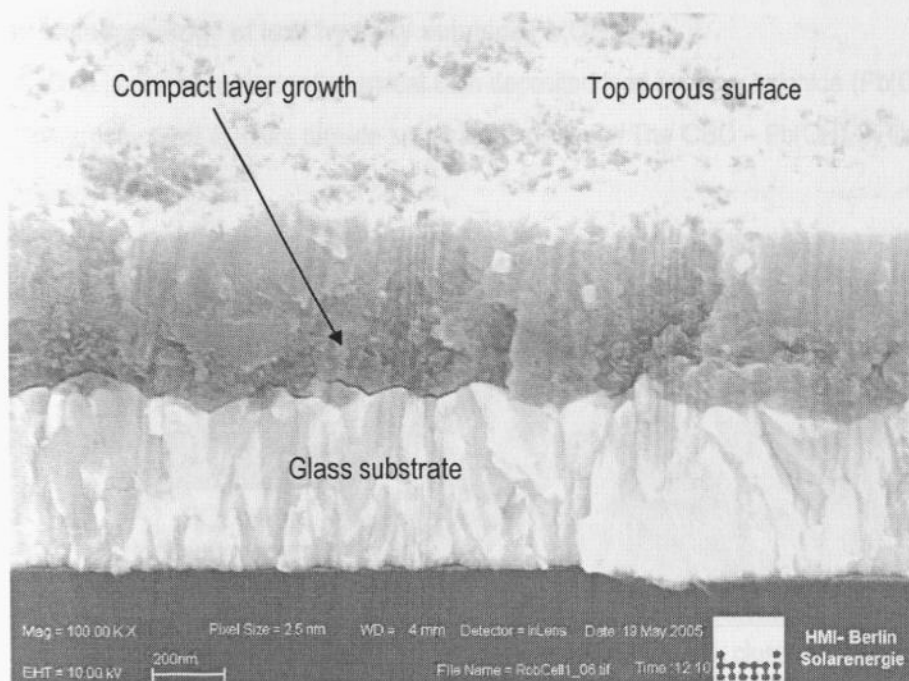


Figure 5.7: Scanning electron micrograph of CBD - $\text{In(OH)}_x\text{S}_y$ thin film magnified at $\times 100,000$. The arrows show the compact layer growth.

The thickness of chemical bath deposited (CBD) - $\text{In(OH)}_x\text{S}_y$ film was estimated to be about 80 nm, for coating deposited in three cycles. There is no distinction in surface structure for as-deposited CBD - $\text{In(OH)}_x\text{S}_y$ film compared to that of the argon atmosphere annealed $\text{In(OH)}_x\text{S}_y$ (thus for the purpose of explanation we use photomicrograph of either of them), the only notable physical difference is change in hue, for as-deposited CBD - $\text{In(OH)}_x\text{S}_y$ film which was bright yellow in colour and then it changed to orange in colour after annealing in inert atmosphere.

The morphological growth of CBD - $\text{In(OH)}_x\text{S}_y$ as a compact layer at the contact with glass substrate and as open microporous film at the surface suggests that the thin film may be suitable as wide band gap semiconductor for solar cells apart from acting as a buffer layer material (Kaufmann, 2002), since the

compact structure will be useful for good rectification while the highly structured surface will enhance optical light trapping.

5.2.3 Surface morphology of lead hydroxy sulphide $\text{Pb(OH)}_x\text{S}_y$

Figure 5.8 is the photomicrograph of chemical bath deposited lead hydroxy sulphide ($\text{Pb(OH)}_x\text{S}_y$) coated on spray pyrolysis deposited titanium dioxide substrate underlayer. The CBD – $\text{Pb(OH)}_x\text{S}_y$ film shown in figure 5.8, is barely visible by SEM.

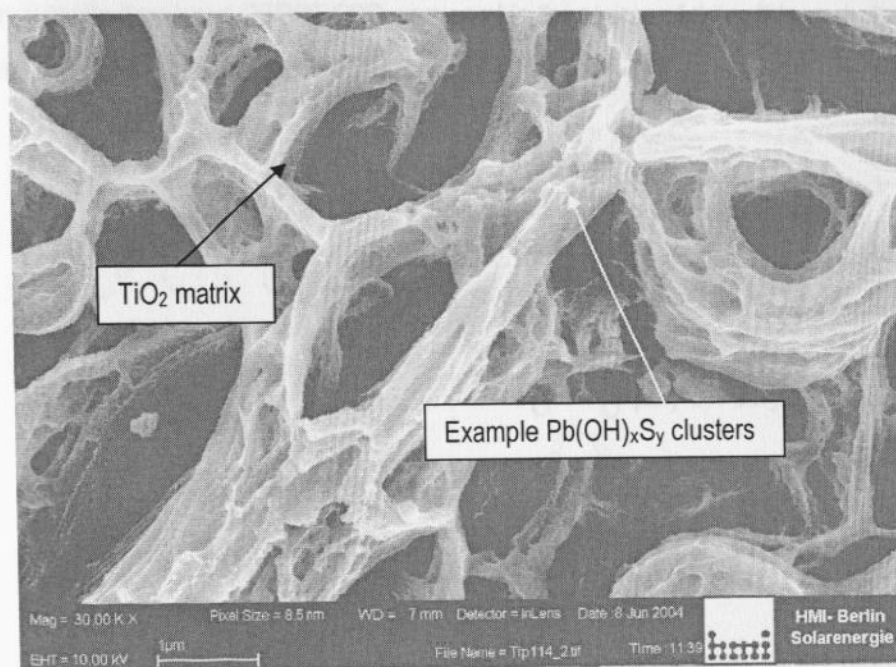


Figure 5.8: Scanning electron micrograph for CBD - lead hydroxy sulphide deposited on TiO_2 magnified at 30,000. The arrows points at TiO_2 porous matrix and typical $\text{Pb(OH)}_x\text{S}_y$ clusters.

The $\text{Pb(OH)}_x\text{S}_y$ particles grew by clustering on the surface of the TiO_2 matrix forming a thin film layer of approximately 10 nm thick. Also it should be noted here that it was not possible to grow coating of $\text{Pb(OH)}_x\text{S}_y$ on bare $\text{SnO}_2:\text{F}$ coated glass. The samples used for SEM analysis had either been deposited on $\text{In(OH)}_x\text{S}_y/\text{SnO}_2:\text{F}$ or $\text{TiO}_2/\text{SnO}_2:\text{F}$ substrates. The physical appearance of the thin films was brownish in colour. Further deposition increasing their thickness made the thin films turn black in colour.

The chemical bath deposition method makes it possible to alter the properties of $\text{Pb(OH)}_x\text{S}_y$ especially the band gap through variation of concentration of precursor materials, (Oja, *et. al.*, 2006). Hoyer and

Könenkamp (1995) demonstrated that it is possible to engineer the band gap of PbS thin film from 0.4 eV for bulk material to as wide as 2.0 eV for thin film, this is confirmed later in our discussion in section 5.2.7.

5.2.4 Poly(3,4-ethylenedioxythiophene) doped with polystyrene sulfonic acid

Figure 5.9 is the chemical structure of electrically semiconducting polymer used in this work. The p-type wide band gap semiconductor shown is a polythiophene derivative poly(3,4-ethylenedioxythiophene) (PEDOT) doped with a water-soluble polyelectrolyte known as polystyrene sulfonic acid (PSS). Three types of undiluted industrially developed PEDOT:PSS were used in the course of doing this work, these included, Baytron P, Baytron PH, and Baytron formula.

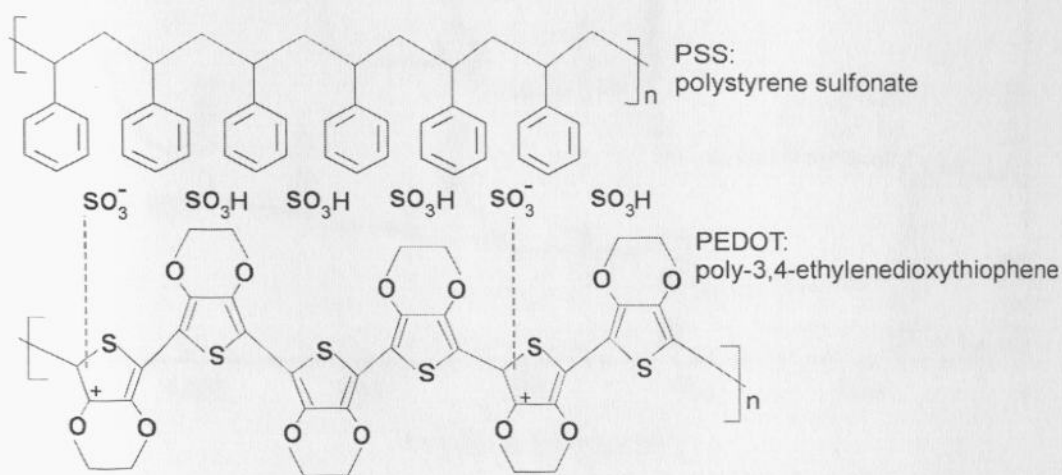


Figure 5.9: Chemical structure of poly(3,4-ethylenedioxythiophene) doped with polystyrene sulfonic acid (PEDOT:PSS).

The PEDOT:PSS belongs to a family of conducting polymers mainly from derivatives of polyanilines, polypyrroles, polythiophenes, polyphenylenes, and poly(*p*-phenylene vinylene)s. The most environmentally stable (especially when exposed to open air and temperature) amongst these polymers are only polythiophene and poly(*p*-phenylene vinylene) (Huang, *et. al.*,2003; Jönsson, *et. al.*, 2003). The conductivity of PEDOT:PSS is known to remain stable when treated for over 1000 hrs at 100 °C, but undergoes irreversible structural changes in the PEDOT chain after 48 hrs in the air at 150 °C, this implies that the oxygen molecules in the air do not have adverse effects on the polymer chain for temperatures below 100 °C (Groenendaal, *et. al.*,2000).

5.2.5 Stoichiometry of lead hydroxy sulphide (Pb(OH)_xS_y).

X-ray photoelectron spectroscopy (XPS) and X-ray induced Auger electron spectroscopy (XAES) survey spectra for the samples of the type In(OH)_xS_y/SnO₂:F and Pb(OH)_xS_y/In(OH)_xS_y/SnO₂:F are shown in figure 5.10.

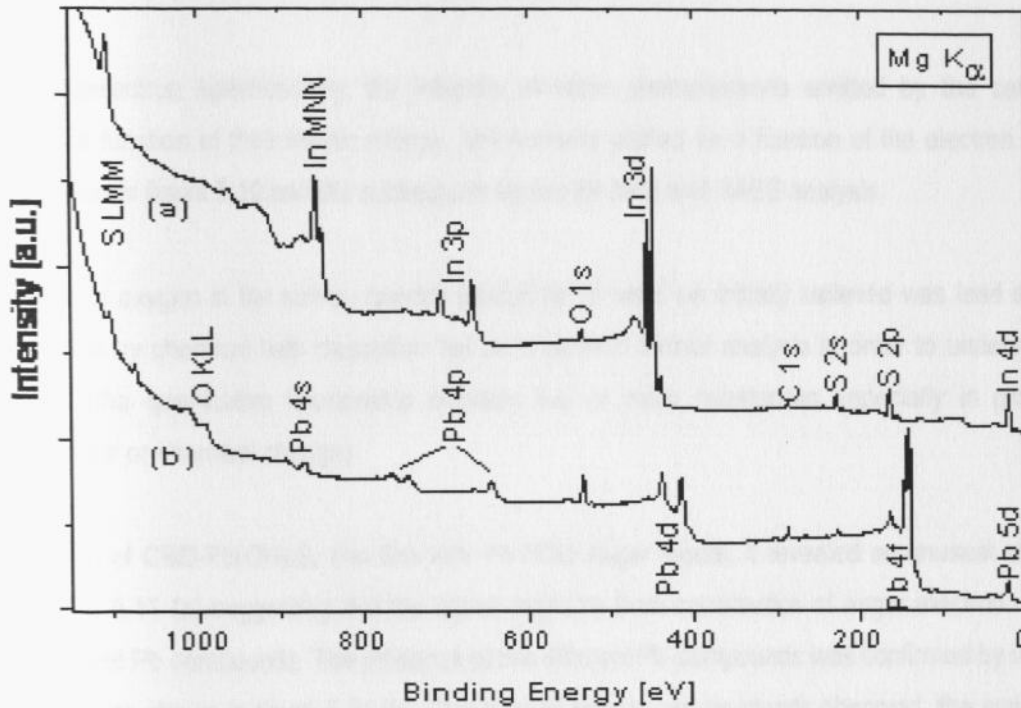


Figure 5.10: X-ray photoelectron and X-ray Auger electron survey spectra's for two samples of the type (a) In(OH)_xS_y/SnO₂:F/glass, and (b) Pb(OH)_xS_y/In(OH)_xS_y/SnO₂:F/glass substrate.

In the figure, the sample represented by the upper spectrum labeled (a) is In(OH)_xS_y coated on SnO₂:F/glass substrate, while the lower spectrum labeled (b) is for sample of Pb(OH)_xS_y coated on In(OH)_xS_y/SnO₂:F/glass substrate.

In figure 5.10, the upper spectrum labeled (a) shows Mg K_α photoelectron excitation in indium (In), sulfur (S) and oxygen (O) atoms from different atomic orbitals (example 1s, 2p, 3p and 4d etc), and a possible contamination because of the presence of carbon (C) atom. The upper spectrum also shows MNN Auger electron excitation in indium atom, where the first letter M denotes the core level hole, while the middle N is the relaxing electron's initial state and last letter N is the emitted electrons initial energy state; the Auger

electron nomenclatures is defined by $j - j$ coupling method for heavy elements ($Z \geq 75$) and the Russell Sanders (L - S) method for lighter elements ($Z < 20$) and a combination of both for intermediate elements, Z denotes the atomic number. In the same figure 5.10, the lower spectrum labeled (b) reveals photoelectron excitation from different atomic orbitals in lead (Pb), and also Auger electrons excitation KLL and LMM in oxygen (O) and sulfur (S) atoms, respectively (Kittel, 1996).

In X-ray photoelectron spectroscopy, the intensity of those photoelectrons emitted by the sample is measured as a function of their kinetic energy, and normally plotted as a function of the electron binding energy as shown in figure 5.10 and the subsequent figures for XPS and XAES analysis.

The presence of oxygen in the survey spectra labeled (b) in what we initially believed was lead sulphide (PbS) deposited by chemical bath deposition led us to perform further analysis in order to understand its stoichiometry (the quantitative relationship between two or more substances especially in processes involving physical or chemical change).

Upon excitation of CBD-Pb(OH)_xS_y thin film with Pb NOO Auger signal, it revealed an unusual shape as shown in figure 5.11 (a) suggesting that the signal might be from contribution of auger electrons from at least two different Pb compounds. The presence of two different Pb compounds was confirmed by using Pb 4f_{7/2} emission as shown in figure 5.11 (b). The doublet signals can be clearly observed, the main signal contribution [II] which peaks at 137.3 ± 0.1 eV can be attributed to PbS, this is corroborated by literature data (PbS - 137.3 – 137.8 eV) from work done by Pederson (1982). In figure 5.11 (b), a clear signal can also be observed at 138.3 ± 0.1 eV, which can be attributed to PbO. The PbO contribution [I] is in good agreement with literature work done by Pederson (1982), where PbO signal was recorded to appear between $137.4 \pm 0.1 - 139 \pm 0.1$ eV. The signal for component [II] was also confirmed by O 1s emission spectra shown in figure 5.11 (c). In figure 5.11 (c) the main signal is attributed to PbO since this is also supported by literature work by Kim, *et. al.*, (1973); Wagner, *et. al.*, (1980), for PbO (527.5 – 531.6 eV).

Binding Energy (eV)

The photoelectron and X-ray induced Auger electron spectroscopy for CBD-Pb(OH)_xS_y thin film with (a) Pb NOO (b) Pb 4f_{7/2} (c) and O 1s Auger signals

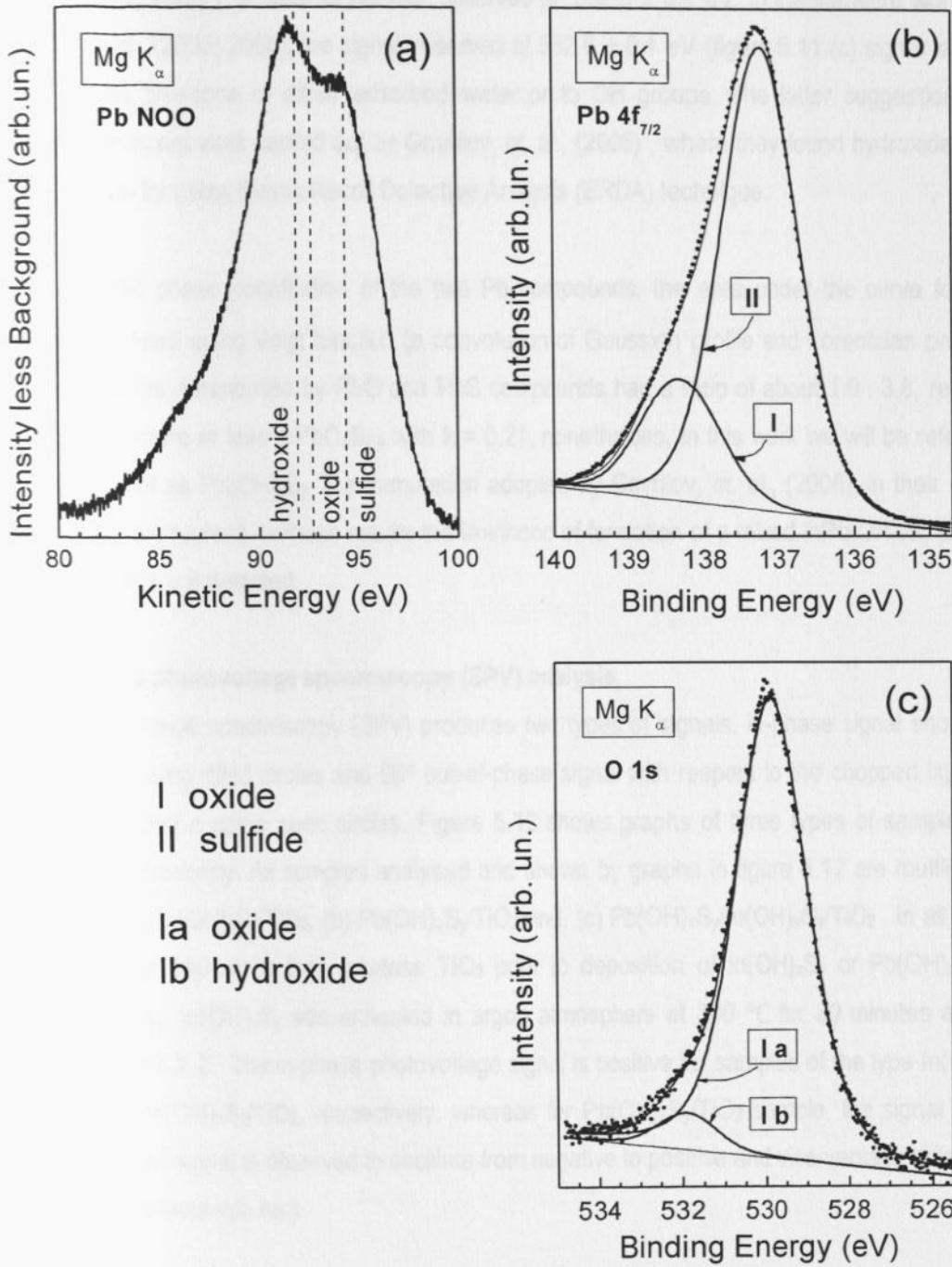


Figure 5.11: X-ray photoelectron and X-ray induced Auger electron spectroscopies for $\text{Pb(OH)}_x\text{S}_y/\text{In(OH)}_x\text{S}_y/\text{SnO}_2:\text{F}$ sample excited with (a) Pb NOO (b) Pb 4f_{7/2} (b) and O 1s Auger signals from Mg K_α source.

At higher binding energy, a small signal was observed at 532.8 ± 0.1 eV. In the literature work published by Bayon, *et. al.*, (2005; 2006), the signal observed at 532.8 ± 0.1 eV (figure 5.11 (c) signal labeled lb) is ascribed to the presence of either adsorbed water or to OH groups. The latter suggestion has been confirmed in a recent work carried out by Gavrilov, *et. al.*, (2006), where they found hydroxide ions in the film composition by using Elastic Recoil Detection Analysis (ERDA) technique.

Using the mixed phase contribution of the two Pb compounds, the area under the curve for Pb $4f_{3/2}$ emission were fitted using Voigt function (a convolution of Gaussian profile and Lorentzian profile), and it was found that the contribution by PbO and PbS compounds had a ratio of about 1.0 : 3.8, revealing that the absorber is more or less a PbO_kS_{1-k} with $k = 0.21$, nonetheless, in this work we will be referring to the absorber material as $Pb(OH)_xS_y$, the formulation adopted by Gavrilov, *et. al.*, (2006), in their recent work (see also literature review). In these results the likelihood of formation of a mixed $InPb(OH)_xS_y$ phase due to ion exchange was not detected.

5.2.6 Surface photovoltage spectroscopy (SPV) analysis

Surface photovoltage spectroscopy (SPV) produces two types of signals, in-phase signal shown in figure 5.12a, b and c using filled circles and 90° out-of-phase signal with respect to the chopped light shown in figure 5.12a, b and c using open circles. Figure 5.12 shows graphs of three types of samples analysed using SPV spectroscopy. All samples analysed and shown by graphs in figure 5.12 are multilayered type consisting of: (a) $In(OH)_xS_y/TiO_2$, (b) $Pb(OH)_xS_y/TiO_2$ and, (c) $Pb(OH)_xS_y/In(OH)_xS_y/TiO_2$. In all cases, TiO_2 was annealed at $450^\circ C$ to form anatase TiO_2 prior to deposition of $In(OH)_xS_y$ or $Pb(OH)_xS_y$ or both, respectively. Also, $In(OH)_xS_y$ was annealed in argon atmosphere at $300^\circ C$ for 30 minutes as explained earlier in section 4.2.2. The in-phase photovoltage signal is positive for samples of the type $In(OH)_xS_y/TiO_2$ and $Pb(OH)_xS_y/In(OH)_xS_y/TiO_2$, respectively, whereas for $Pb(OH)_xS_y/TiO_2$ sample, the signal is negative. The phase-shifted signal is observed to oscillate from negative to positive and vice versa at different photon energy, eV (or wavelength nm).

The surface photovoltage spectroscopy (SPV) is a technique for investigating both optical (spectral properties of photovoltage) and transport (time resolved properties of photovoltage) properties of semiconductor materials using photovoltage.

Three processes are involved in generation of photovoltage signal, these are: absorption of light photon, followed by generation and separation of electron – hole pair, and eventual charge transport in respective electrodes. In this work, SPV studies were performed in order to obtain information about both band gap, E_g and energy values below the band gap, in the exponential absorption tails, E_t . The onset of the SPV signal indicates the separation in space of the photo-generated electron – hole pairs when light absorption sets on.

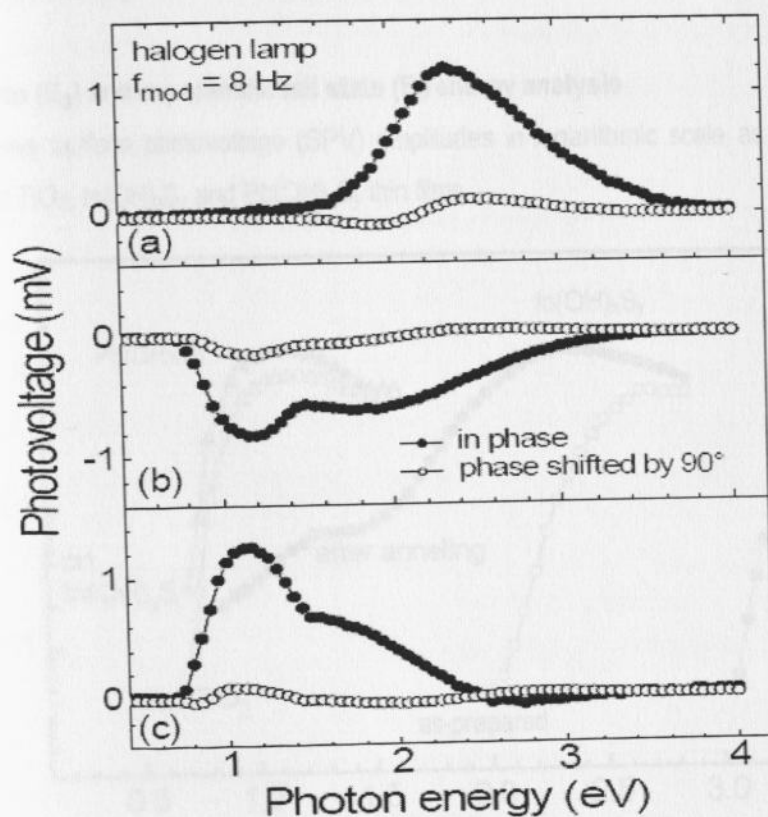


Figure 5.12: Surface photovoltage spectroscopy for different multilayered samples, (a) $\text{TiO}_2/\text{In}(\text{OH})_x\text{S}_y$, (b) $\text{TiO}_2/\text{Pb}(\text{OH})_x\text{S}_y$ and (c) $\text{TiO}_2/\text{In}(\text{OH})_x\text{S}_y/\text{Pb}(\text{OH})_x\text{S}_y$, the filled circles depicts the in-phase component while the unfilled circles shows the 90° phase shifted signal.

A positive amplitude of SPV signal for the in-phase signal means that excess negative charge carriers are being injected into the bulk of the material with respect to the positive charge carriers (Duzhko, 2002). Figure 5.12(a) shows a positive in-phase signal for $\text{In}(\text{OH})_x\text{S}_y/\text{TiO}_2$ sample, this implies that excess negative charge carriers are being injected into the bulk TiO_2 thin film. In contrast, figure 5.12(b) shows the

opposite situation which is quite unusual. In this work we attributed this to trap states dominance at the interface between the absorber material ($\text{Pb}(\text{OH})_x\text{S}_y$) and TiO_2 thin film. Lastly, the spectra for multilayered film consisting of $\text{In}(\text{OH})_x\text{S}_y$ thin film sandwiched between $\text{Pb}(\text{OH})_x\text{S}_y$ and TiO_2 is shown in figure 5.12(c). A positive in-phase signal for energies lower than 2.4 eV is observed for $\text{TiO}_2/\text{In}(\text{OH})_x\text{S}_y/\text{Pb}(\text{OH})_x\text{S}_y$ multilayer film. This means that unlike in the $\text{TiO}_2/\text{In}(\text{OH})_x\text{S}_y$ sample, the positive charge carriers are separated towards $\text{In}(\text{OH})_x\text{S}_y$ deposited on TiO_2 and injected into the bulk $\text{In}(\text{OH})_x\text{S}_y/\text{TiO}_2$ material. The deduction arrived at is corroborated by literature work earlier reported by Bayon, *et. al.*, (2005; 2006).

5.2.7 Band gap (E_g) and exponential tail state (E_t) energy analysis

Figure 5.13 shows surface photovoltage (SPV) amplitudes in logarithmic scale as a function of photon energy in eV, for TiO_2 , $\text{In}(\text{OH})_x\text{S}_y$ and $\text{Pb}(\text{OH})_x\text{S}_y$ thin films.

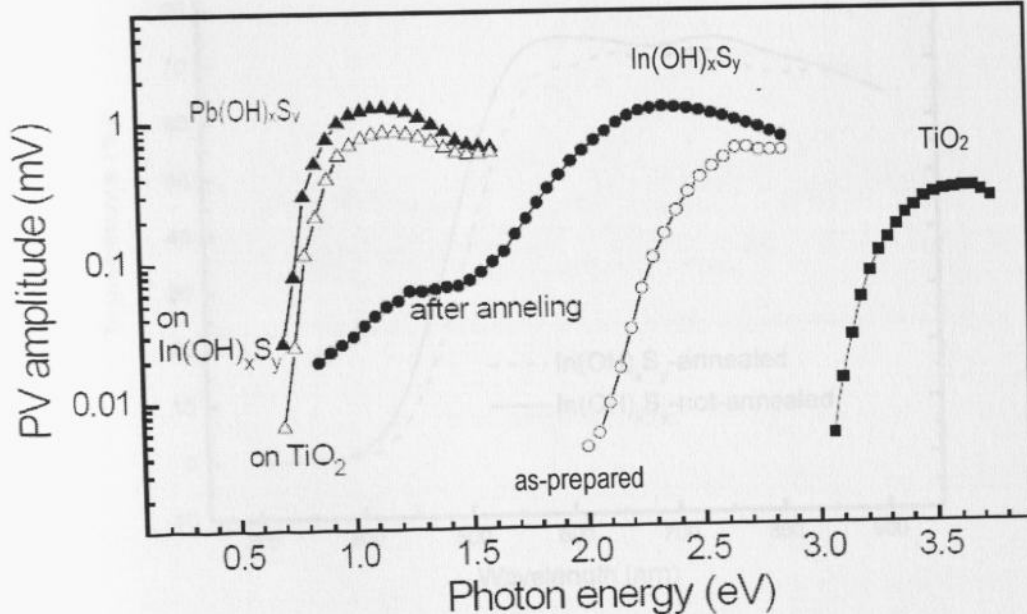


Figure 5.13: Surface photovoltage spectroscopy amplitude for $\text{Pb}(\text{OH})_x\text{S}_y$ prepared on $\text{In}(\text{OH})_x\text{S}_y$ (filled triangles) and TiO_2 (open triangles), $\text{In}(\text{OH})_x\text{S}_y$ as prepared (unfilled circles) and annealed sample (filled circles) and TiO_2 (squares).

For the purpose of comparison analysis of the effect of underlying substrate material, the $\text{Pb}(\text{OH})_x\text{S}_y$ thin film coated on $\text{TiO}_2/\text{SnO}_2:\text{F}$ and $\text{In}(\text{OH})_x\text{S}_y$ substrates, are shown in figure 5.13 using SPV signals plotted with open and filled triangles, respectively; this was necessitated by the fact that it was not possible to grow thin films of $\text{Pb}(\text{OH})_x\text{S}_y$ on bare $\text{SnO}_2:\text{F}/\text{glass}$ substrate.

The following was deduced from the results shown in figure 5.13: the band gap energy of anatase TiO_2 was calculated to be approximately $E_g = 3.2$ eV, and since the band gap energy is not abrupt the energy in the exponential tail states below the band gap E_t was computed from the gradient of the amplitude signal of the graph shown for TiO_2 and was approximately $E_t = 45$ meV. For the case of $\text{In}(\text{OH})_x\text{S}_y$ thin film, the band gap and tail state energies for as-prepared sample were approximately; $E_g = 2.4$ eV, and $E_t = 80$ meV, respectively. After annealing the sample in argon atmosphere at 300°C for 30 minutes, the band gap and exponential tail state values shifted to $E_g = 2.2$ eV and $E_t = 190$ meV, respectively. These changes could mean that $\text{In}(\text{OH})_x\text{S}_y$ underwent stoichiometric changes or developed deep defects states after annealing (Bayon, *et. al.*, 2002; 2005; Bayon and Herrero, 2000). The changes in stoichiometry after annealing $\text{In}(\text{OH})_x\text{S}_y$ are also supported by the observed decrease in optical transmittance of the material as shown in figure 5.14.

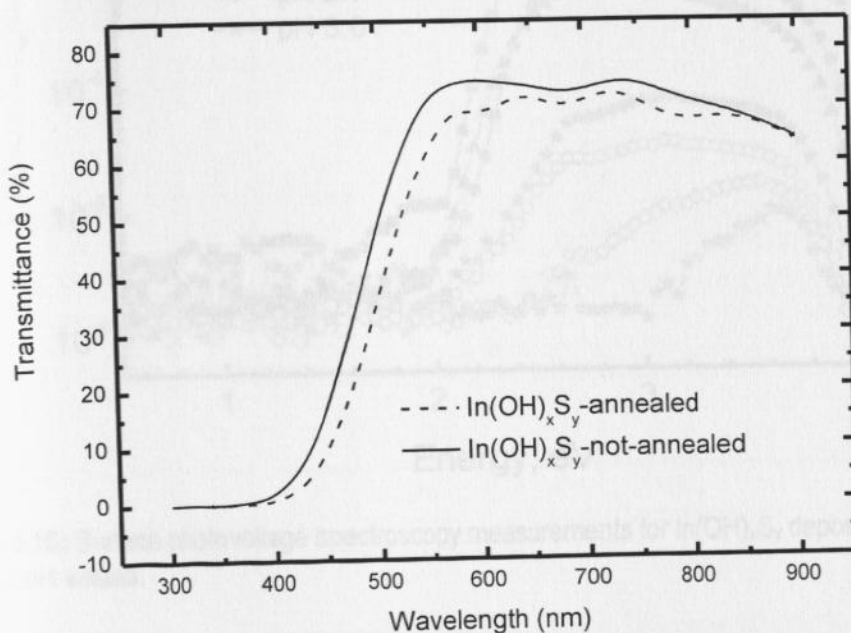


Figure 5.14: Optical transmittance of as prepared $\text{In}(\text{OH})_x\text{S}_y$ (not annealed) and $\text{In}(\text{OH})_x\text{S}_y$ annealed in argon atmosphere for 30 minutes at 300°C .

Interestingly, for the case of $\text{Pb}(\text{OH})_x\text{S}_y$, the two samples namely $\text{Pb}(\text{OH})_x\text{S}_y/\text{TiO}_2$ and $\text{Pb}(\text{OH})_x\text{S}_y/\text{In}(\text{OH})_x\text{S}_y$ had the same value for band gap and exponential tail state energy below the band gap, that is $E_g = 0.85$ eV and $E_t = 40$ meV, respectively. The observation suggests that, the formation of a mixed homogeneous $\text{InPb}(\text{OH})_x\text{S}_y$ phase due to ion exchange mechanism seems unlikely, thus supporting XPS/XAES results earlier discussed.

5.2.8 Band gap optimization of the buffer layer.

Surface photovoltage spectroscopy technique was used to monitor variation in the band gap for as-prepared $\text{In}(\text{OH})_x\text{S}_y$ to be used as the buffer layer. Figure 5.15 shows photovoltage amplitudes plotted as a function of photon energy in eV.

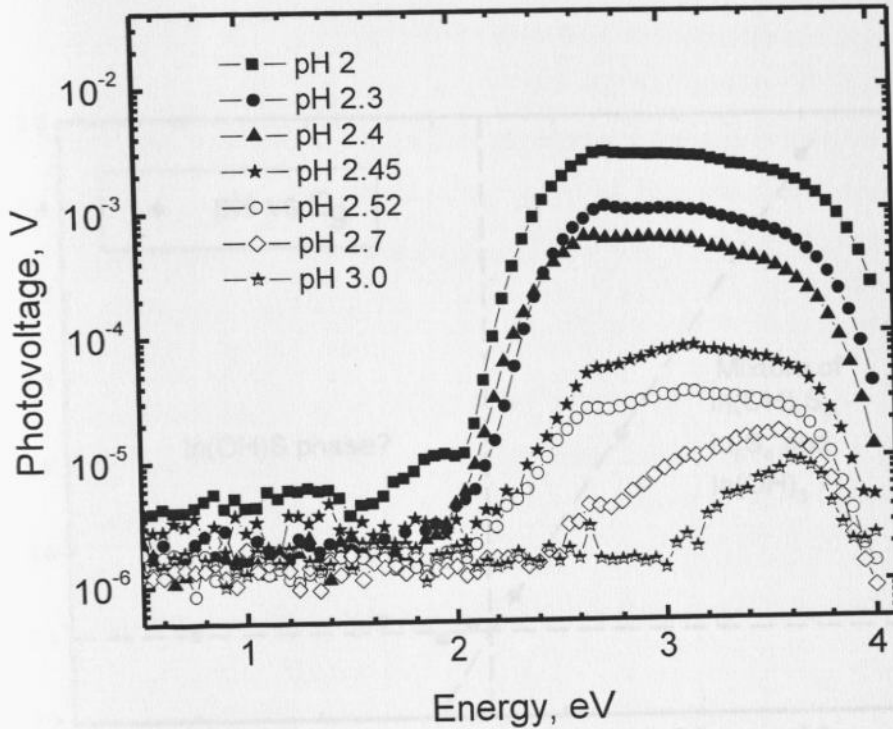


Figure 5.15: Surface photovoltage spectroscopy measurements for $\text{In}(\text{OH})_x\text{S}_y$ deposited at different pH values.

It is observed in figure 5.15 that, when pH value of the aqueous solution used in preparing the samples was decreased from 3.0 – 2.0 pH, it resulted in corresponding increase in photovoltage amplitude signal. The change in pH value is as a result of varying the HCl precursor concentration in the chemical bath as explained in section 4.2.2. The concentration in this case was varied from 0.02 – 0.001 M resulting in pH changes of the aqueous solution from 2.0 – 3.0.

Figure 5.16 shows band gap energy in eV of $\text{In}(\text{OH})_x\text{S}_y$ samples plotted as a function of pH of the solution used in coating respective samples. The band gap values were computed from the photovoltage amplitude signals shown in figure 5.15. It is observed in figure 5.16 that, thin films of $\text{In}(\text{OH})_x\text{S}_y$ fabricated using aqueous solution with pH values of approximately <2.5 , had band gaps < 2.6 eV, whilst those samples fabricated from aqueous solution of higher pH values that is >2.5 , the band gaps of the samples produced were between 2.6 – 3.5 eV.

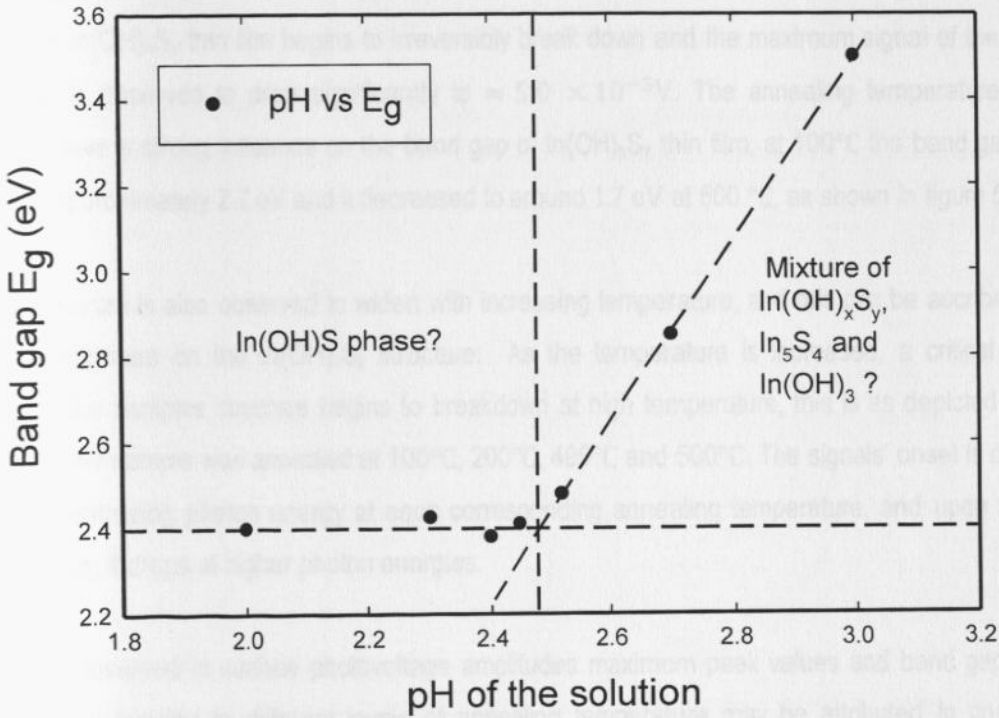


Figure 5.16: Derived E_g as a function of pH value of $\text{In}(\text{OH})_x\text{S}_y$ SPV analysis shown in figure 5.15. The question marks depict the likelihood of $\text{In}(\text{OH})_x\text{S}_y$ phase in either of the sections.

The changes observed in band gap energies in $\text{In}(\text{OH})_x\text{S}_y$ thin films as a result of varying the pH of the aqueous solution used in their deposition, may be attributed to phase changes during coating. This allusion is corroborated by similar work reported in the literature by Bayon, *et. al.*, (1998; and 2002) and Bayon and Herrero, (2000), that changes in pH of the aqueous solution influences the contents in $\text{In}(\text{OH})_x\text{S}_y$, such that higher pH values give high content of hydroxide and/or oxide, whereas dominant content in sulphide is realised when deposition is done at low pH value of the chemical bath solution.

5.2.9 Effect of annealing $\text{In}(\text{OH})_x\text{S}_y$ thin film

The effects of annealing temperature on $\text{In}(\text{OH})_x\text{S}_y$ thin films is shown by the photovoltage amplitudes as a function of photon energy in figure 5.17. The figure shows ex-situ measurements of photovoltage spectroscopy amplitudes for the same sample at different stages of annealing temperature from 100 °C - 500°C. At each stage shown, the sample prior to measurement had been annealed in inert atmosphere for 30 minutes at the temperature indicated in each of the diagrams. The SPV maximum peak amplitude is observed to initially increase with increasing temperature from surface photovoltage amplitude of approximately $\approx 6 \times 10^{-5}\text{V}$ at 100 °C to $\approx 12 \times 10^{-5}\text{V}$ at 400 °C, thereafter, at higher temperature of 500°C, the $\text{In}(\text{OH})_x\text{S}_y$ thin film begins to irreversibly break down and the maximum signal of the surface photovoltage is observed to drop significantly to $\approx 5.0 \times 10^{-5}\text{V}$. The annealing temperature also is observed to have a strong influence on the band gap of $\text{In}(\text{OH})_x\text{S}_y$ thin film, at 100°C the band gap of the sample was approximately 2.2 eV and it decreased to around 1.7 eV at 500 °C, as shown in figure 5.17.

The SPV spectrum is also observed to widen with increasing temperature, and this can be ascribed to the effect of temperature on the $\text{In}(\text{OH})_x\text{S}_y$ structure. As the temperature is increased, a critical point is reached and the samples structure begins to breakdown at high temperature, this is as depicted by SPV signals when the sample was annealed at 100°C, 200°C, 400°C and 500°C. The signals' onset is observed to begin at decreasing photon energy at each corresponding annealing temperature, and upon reaching maximum value, it drops at higher photon energies.

The changes observed in surface photovoltage amplitudes maximum peak values and band gaps, when the sample is subjected to different levels of annealing temperature may be attributed to changes in $\text{In}(\text{OH})_x\text{S}_y$ stoichiometry. This is in accordance to works reported elsewhere (Bayon, *et. al.*, 1998; 1999; 2002; 2005; 2006; Barreau, *et. al.*, 2003; Kaufmann, 2002).

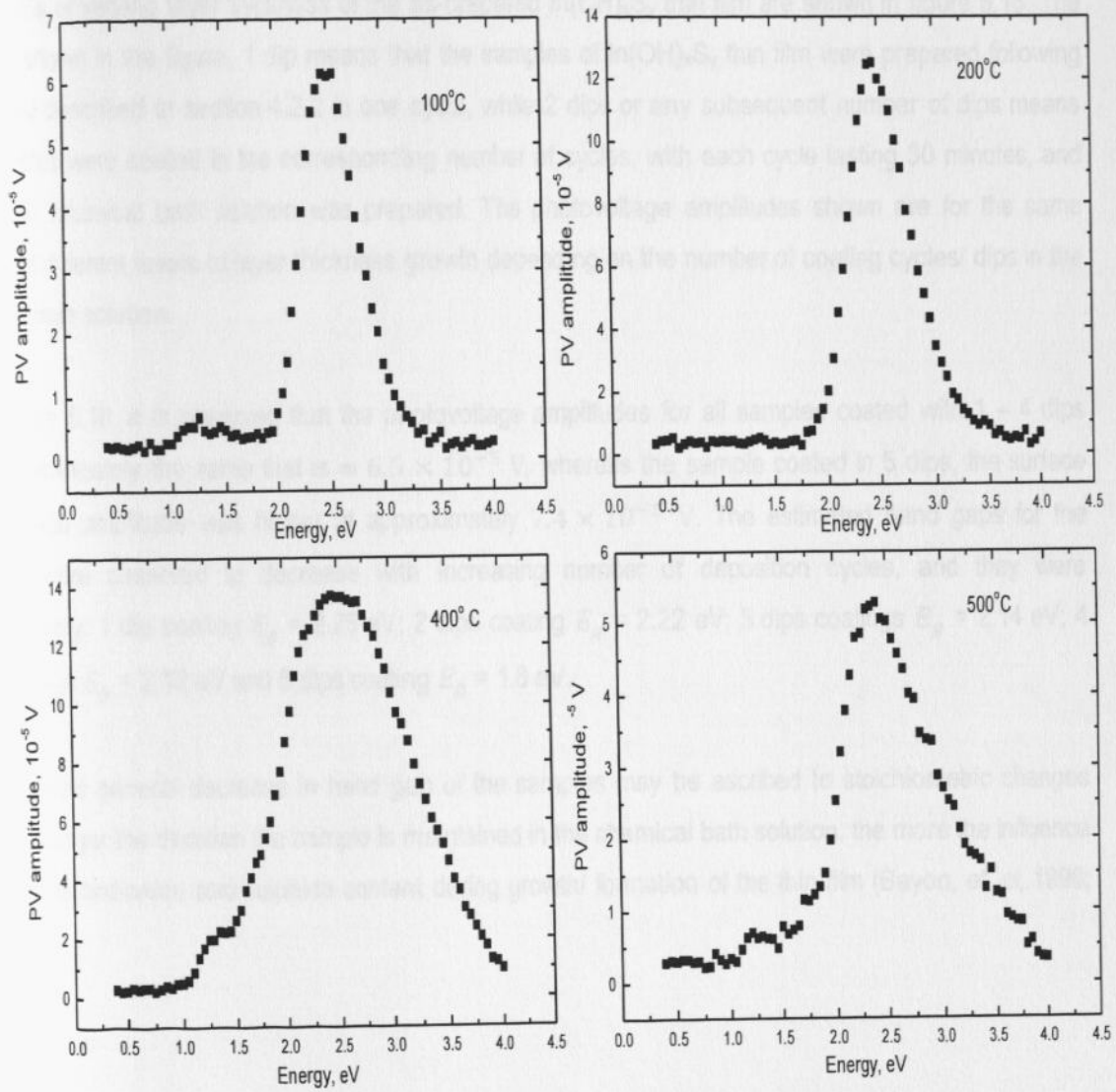


Figure 5. 17: Influence of temperature on $\text{In}(\text{OH})_x\text{S}_y$ annealed in argon atmosphere at different temperature levels (100 °C - 500 °C). SPV measurements were done after annealing the sample at the temperatures shown. After each measurement the sample was annealed at higher temperature.

5.2.10 Effect of $\text{In}(\text{OH})_x\text{S}_y$ layer thickness

The effects of varying layer thickness of the as-prepared $\text{In}(\text{OH})_x\text{S}_y$ thin film are shown in figure 5.18. The legends shown in the figure, 1 dip means that the samples of $\text{In}(\text{OH})_x\text{S}_y$ thin film were prepared following procedure described in section 4.2.2 in one cycle, while 2 dips or any subsequent number of dips means the samples were coated in the corresponding number of cycles, with each cycle lasting 30 minutes, and then fresh chemical bath solution was prepared. The photovoltage amplitudes shown are for the same sample at different levels of layer thickness growth depending on the number of coating cycles/ dips in the chemical bath solution.

From figure 5.18, it is observed that the photovoltage amplitudes for all samples coated with 1 – 4 dips were approximately the same that is $\approx 6.5 \times 10^{-5}$ V, whereas the sample coated in 5 dips, the surface photovoltage amplitude was higher at approximately 7.4×10^{-5} V. The estimated band gaps for the samples were observed to decrease with increasing number of deposition cycles, and they were approximately: 1 dip coating $E_g = 2.25$ eV; 2 dips coating $E_g = 2.22$ eV; 3 dips coatings $E_g = 2.14$ eV; 4 dips coatings $E_g = 2.12$ eV and 5 dips coating $E_g = 1.8$ eV.

The observed general decrease in band gap of the samples may be ascribed to stoichiometric changes since the longer the duration the sample is maintained in the chemical bath solution, the more the influence of hydroxide and/oxide and sulphide content during growth/ formation of the thin film (Bayon, *et. al.*, 1998; 2002).

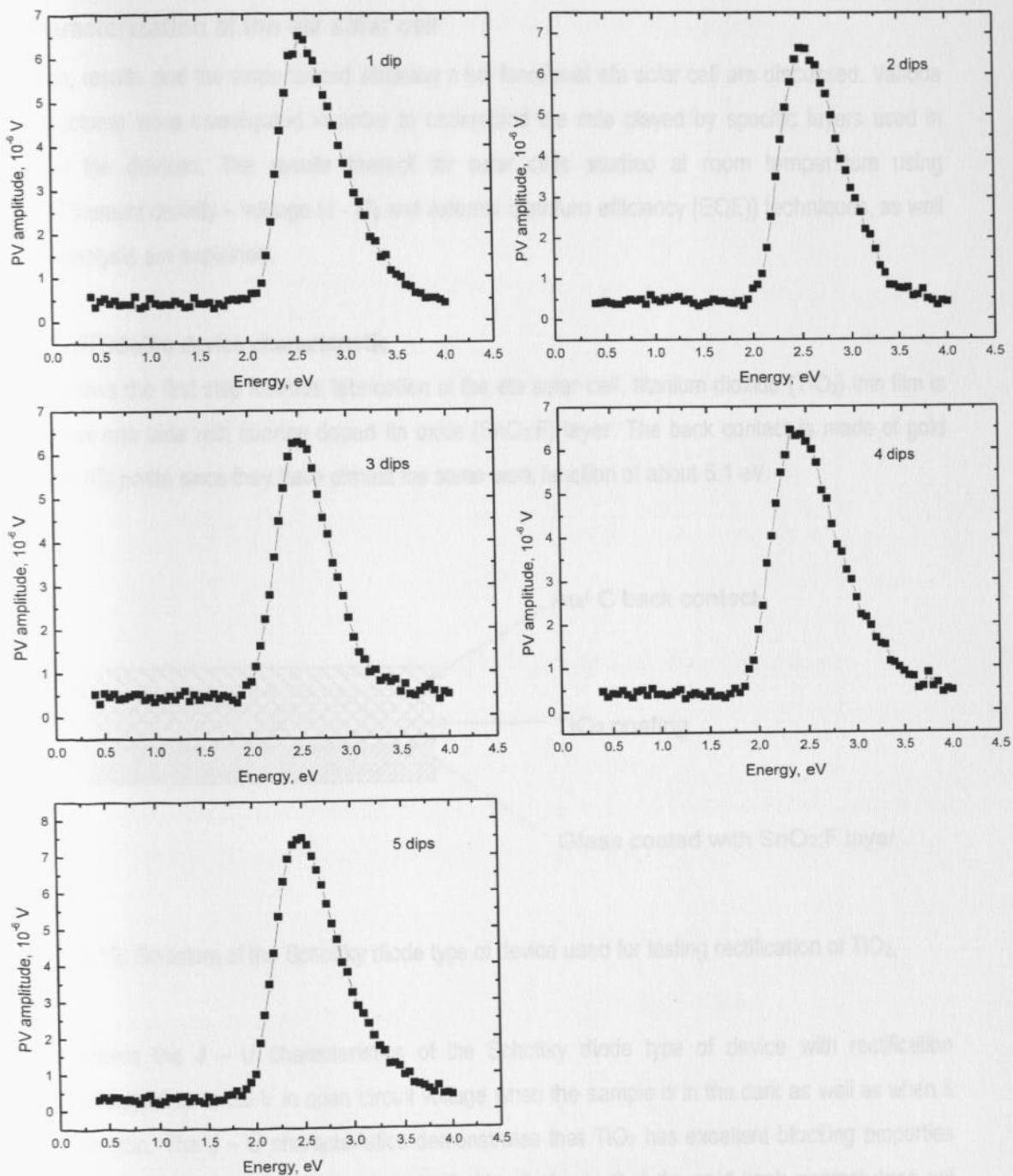


Figure 5.18: Surface photovoltage spectroscopy analysis of $\text{In}(\text{OH})_x\text{S}_y$ thin film of different thicknesses depending on the number of dips in the chemical bath solution.

5.3 Characterization of the eta solar cell

In this section, results and the steps toward attaining a full functional eta solar cell are discussed. Various solar cell structures were investigated in order to understand the role played by specific layers used in fabrication of the devices. The results thereof for solar cells studied at room temperature using optoelectrical (current density – voltage (J - U) and external quantum efficiency (EQE)) techniques, as well as structural analysis are explained.

5.3.1 SnO₂:F/TiO₂/Au device characteristic

Figure 5.19 shows the first step towards fabrication of the eta solar cell, titanium dioxide (TiO₂) thin film is coated on glass one side with fluorine doped tin oxide (SnO₂:F) layer. The back contact is made of gold (Au) or carbon (C) paste since they have almost the same work function of about 5.1 eV.

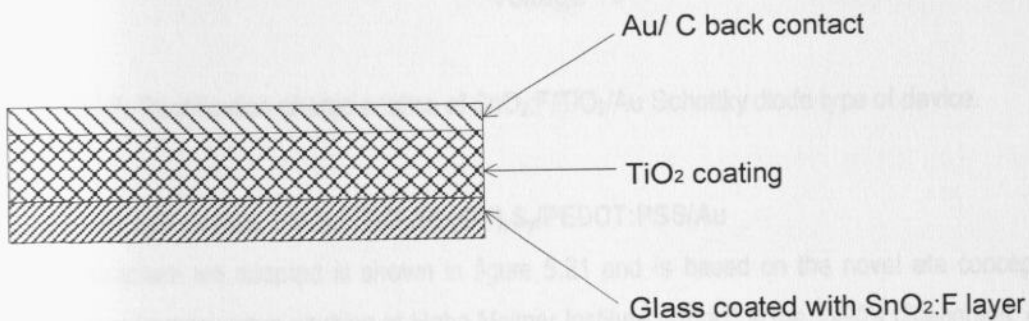


Figure 5.19: Structure of the Schottky diode type of device used for testing rectification of TiO₂.

Figure 5.20 shows the J – U characteristics of the Schottky diode type of device with rectification (photovoltaic effect) of up to 0.6 V in open circuit voltage when the sample is in the dark as well as when it is under illumination. The J – U characteristics demonstrates that TiO₂ has excellent blocking properties essential for good photovoltaic effect of a solar cell. Also it shows that the gold back contact does not diffuse into the bulk of the material since there are no signs of shunting for both dark or under illumination J – U characteristics.

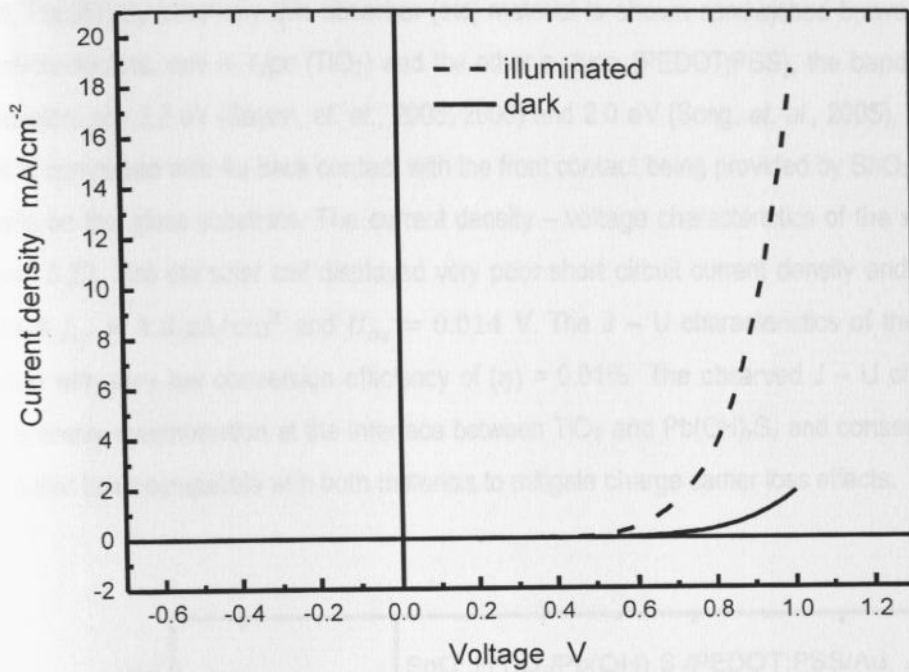


Figure 5.20: Rectification characteristics of $\text{SnO}_2\text{:F/TiO}_2\text{/Au}$ Schottky diode type of device.

5.3.2 ETA solar cell device, $\text{SnO}_2\text{:F/TiO}_2\text{/Pb(OH)}_x\text{S}_y\text{/PEDOT:PSS/Au}$

The solar cell structure we adopted is shown in figure 5.21 and is based on the novel eta concept first proposed by Könenkamps' group working at Hahn Meitner Institute GmbH¹ in the 1990's (Siebentritt, *et. al.*, 1997).

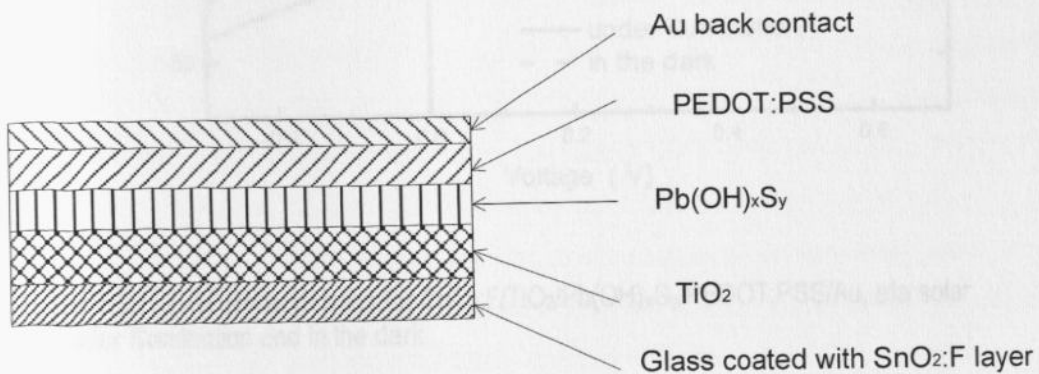


Figure 5.21: Initial eta solar cell proposed in this work, n-type material is TiO_2 , p-type material is PEDOT:PSS and the absorber material is $\text{Pb(OH)}_x\text{S}_y$.

¹ Renamed in 2008 Helmholtz Centre Berlin for Materials and Energie, Lise Meitner Campus

In figure 5.21, $\text{Pb(OH)}_x\text{S}_y$ extremely thin absorber (eta) material is shown sandwiched between two wide band gap semiconductors, one n- type (TiO_2) and the other p- type (PEDOT:PSS), the band gaps of the two semiconductors are 3.2 eV (Bayon, *et. al.*, 2005; 2006) and 2.0 eV (Song, *et. al.*, 2005), respectively. The solar cell is completed with Au back contact with the front contact being provided by SnO_2 :F layer or a thin film of gold on the glass substrate. The current density – voltage characteristics of the solar cell are shown in figure 5.22. The eta solar cell displayed very poor short circuit current density and open circuit voltage of about $J_{sc} = 1.8 \mu\text{A}/\text{cm}^2$ and $U_{oc} = 0.014 \text{ V}$. The J – U characteristics of the device are ohmic in nature with very low conversion efficiency of (η) = 0.01%. The observed J – U characteristics shows there is heavy recombination at the interface between TiO_2 and $\text{Pb(OH)}_x\text{S}_y$ and consequently there is a need for buffer layer compatible with both materials to mitigate charge carrier loss effects.

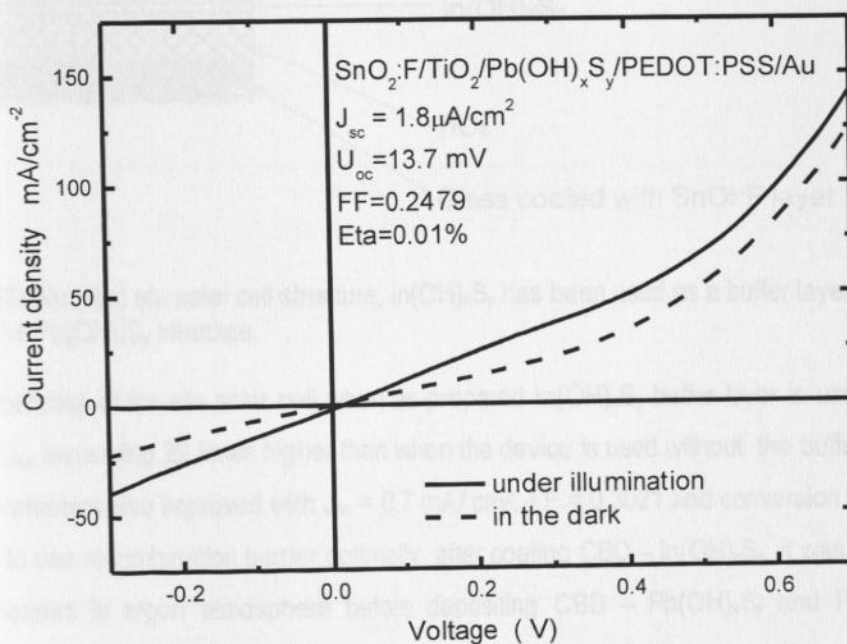


Figure 5.22: J - U characteristics for SnO_2 :F/ TiO_2 / $\text{Pb(OH)}_x\text{S}_y$ /PEDOT:PSS/Au, eta solar cell under illumination and in the dark.

5.3.3 Effect of $\text{In}(\text{OH})_x\text{S}_y$ buffer layer on ETA solar cell device

The modified eta solar cell using $\text{In}(\text{OH})_x\text{S}_y$ recombination barrier inserted between the TiO_2 and $\text{Pb}(\text{OH})_x\text{S}_y$ interface is shown in figure 5.23. The suitability of $\text{In}(\text{OH})_x\text{S}_y$ for use as a buffer layer when chalcogenide (chemical compound consisting of at least one chalcogen ion, that is, either sulfides, selenides or tellurides) material is used as sensitizer for transparent semiconductor is described in the literature by Kaufmann (2002), Kaufmann, *et. al.*, (2002) and, Wienke, *et. al.*, (2003).

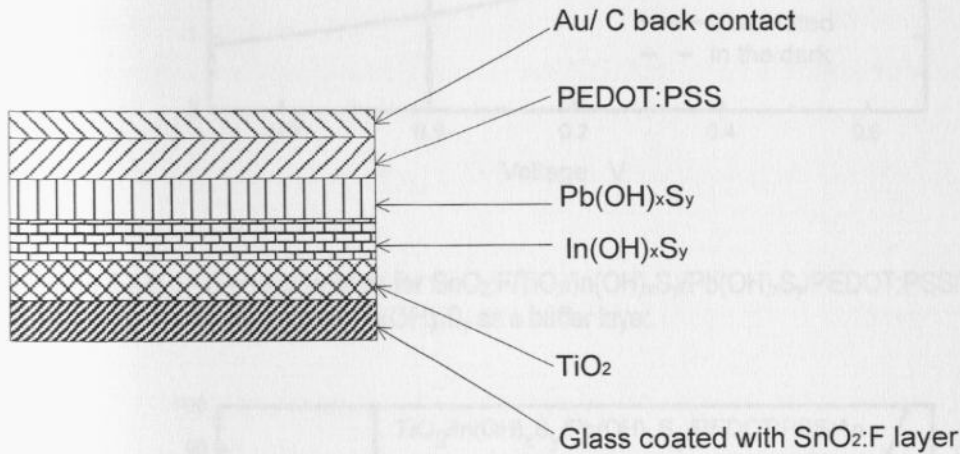


Figure 5.23: Modified eta solar cell structure, $\text{In}(\text{OH})_x\text{S}_y$ has been used as a buffer layer at the TiO_2 and $\text{Pb}(\text{OH})_x\text{S}_y$ interface.

The J – U characteristics of the eta solar cell when as-prepared $\text{In}(\text{OH})_x\text{S}_y$ buffer layer is used improved substantially with U_{oc} increasing 22 times higher than when the device is used without the buffer layer. The other solar cell parameters also improved with $J_{sc} = 0.7 \text{ mA/ cm}^2$, $FF = 0.3021$ and conversion efficiency, $\eta = 0.07\%$. In order to use recombination barrier optimally, after coating CBD – $\text{In}(\text{OH})_x\text{S}_y$, it was annealed at $300 \text{ }^\circ\text{C}$ for 30 minutes in argon atmosphere before depositing CBD – $\text{Pb}(\text{OH})_x\text{S}_y$ and PEDOT:PSS. Annealing the buffer layer gave us the best results for eta solar cell; these are shown by J – U characteristics in figure 5.25. The device open circuit voltage and short circuit current density were 281 mV and 7.4 mA/ cm^2 , respectively. The fill factor was approximately 0.4 and the overall conversion efficiency was about 0.83%, while series and parallel (shunt) resistance of the device were calculated to be approximately $47.4 \text{ } \Omega$ and $4758.9 \text{ } \Omega$, respectively (see appendix B for screen shots of the software used in calculations).

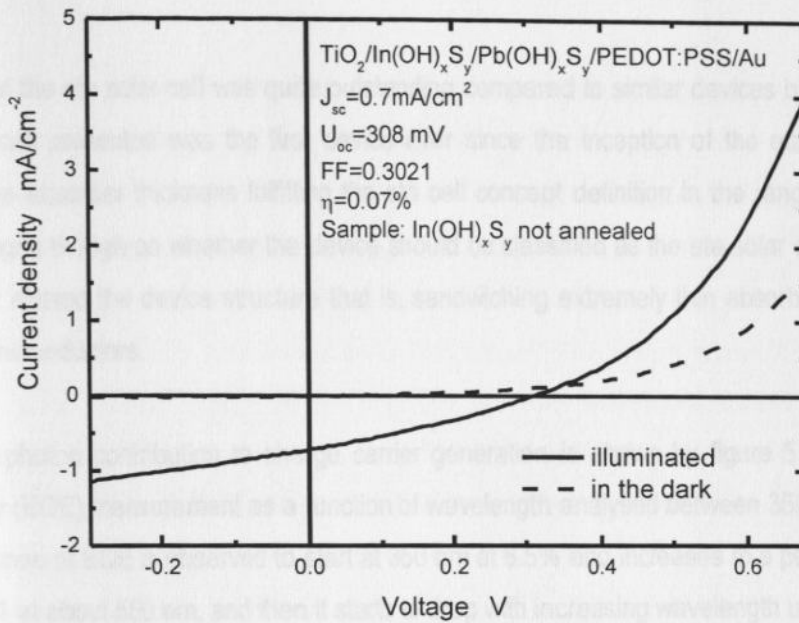


Figure 5.24: J - U characteristics for $\text{SnO}_2:\text{F}/\text{TiO}_2/\text{In}(\text{OH})_x\text{S}_y/\text{Pb}(\text{OH})_x\text{S}_y/\text{PEDOT:PSS}/\text{Au}$, eta solar cell with as-prepared $\text{In}(\text{OH})_x\text{S}_y$ as a buffer layer.

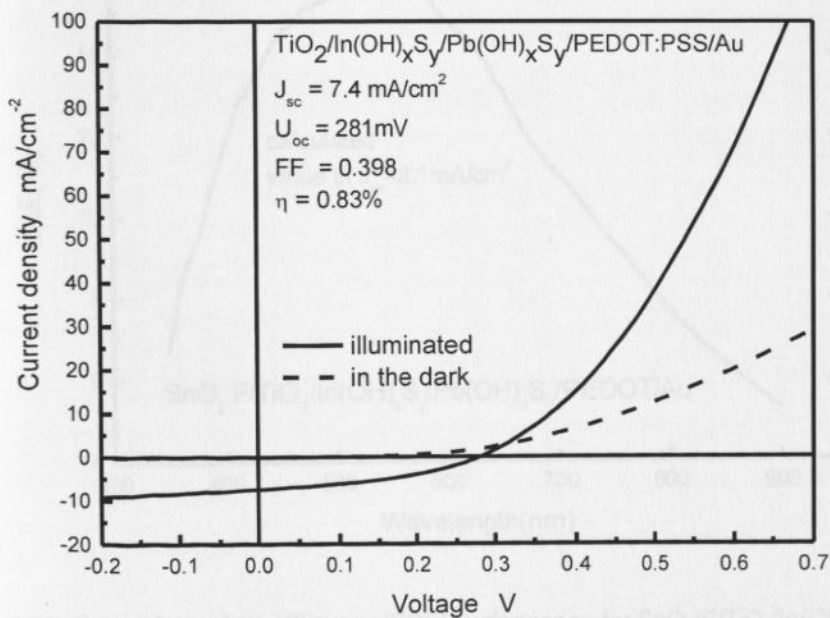


Figure 5.25: J - U characteristics for $\text{SnO}_2:\text{F}/\text{TiO}_2/\text{In}(\text{OH})_x\text{S}_y/\text{Pb}(\text{OH})_x\text{S}_y/\text{PEDOT:PSS}/\text{Au}$, eta solar cell with annealed $\text{In}(\text{OH})_x\text{S}_y$ buffer layer giving the best conversion efficiency.

The performance of the eta solar cell was quite outstanding compared to similar devices based on the eta concept. The eta cell presented was the first device ever since the inception of the eta concept to be fabricated using the absorber thickness fulfilling the eta cell concept definition in the range of ≈ 10 nm. Controversy still rages though on whether the device should be classified as the eta solar cell because the use of buffer layer altered the device structure that is, sandwiching extremely thin absorber between two wide band gap semiconductors.

The incident light photon contribution to charge carrier generation is shown by figure 5.26, as external quantum efficiency (EQE) measurement as a function of wavelength analysed between 350 nm to 900 nm. The spectral response of EQE is observed to start at 350 nm at 6.5% and increases to a peak maximum of approximately 16% at about 550 nm, and then it starts to drop with increasing wavelength up to 900 nm.

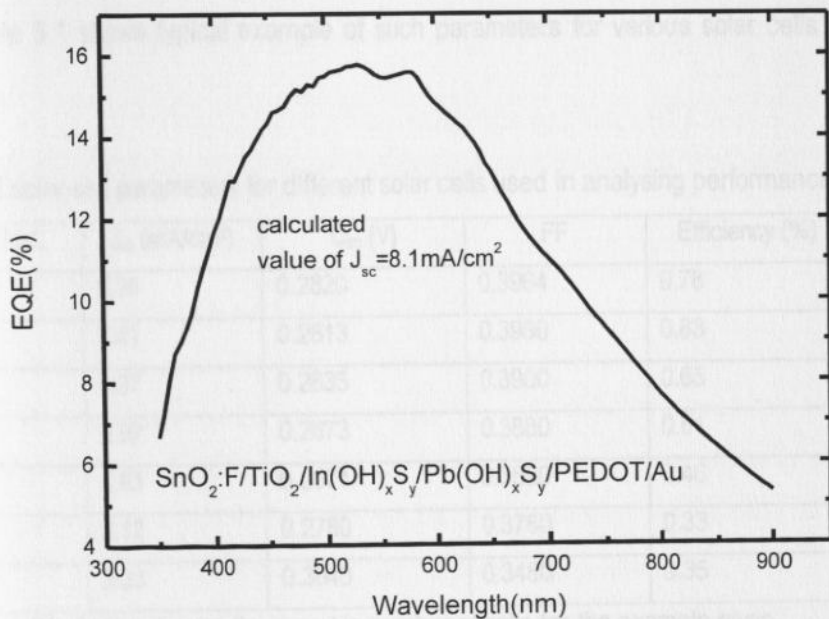


Figure 5.26: External quantum efficiency (EQE) performance for $\text{SnO}_2:\text{F}/\text{TiO}_2/\text{In}(\text{OH})_x\text{S}_y/\text{Pb}(\text{OH})_x\text{S}_y/\text{Au}$ eta solar cell measured from 350 nm to 900 nm. Inset is the calculated J_{sc} value.

Interestingly, there is no significant contribution to EQE signal by the $\text{Pb(OH)}_x\text{S}_y$ absorber whose band gap was estimated to be about 0.85 eV, which means the peak absorption wavelength of the material should be about 1459 nm, therefore in order for the absorber material used to make any contribution, it is expected the EQE to be larger for wavelengths beyond 700 nm, which is not the case as is shown in figure 5.26. The observation suggests that the interface between $\text{In(OH)}_x\text{S}_y/\text{Pb(OH)}_x\text{S}_y$ may also be contributing to the photovoltaic action of the eta solar cell, a conclusion that corroborates earlier works (Oja, *et. al.*, 2006; Musembi, *et. al.*, 2008). Current density of the eta solar cell was also calculated from EQE spectral response by integrating the area under the curve in figure 5.26, and by using normalization method to get approximately $J_{sc} = 8.1 \text{ mA/cm}^2$, which agrees well with the short circuit current density obtained from $J - U$ characteristics measurements.

The trend in solar cell parameters which includes open circuit voltage, fill factor, short circuit current density and conversion efficiency were further used in analysing solar cell behaviour to gain deeper understanding of the device. Table 5.1 shows typical example of such parameters for various solar cells with different performances.

Table 5.1: Typical solar cell parameters for different solar cells used in analysing performance trend

Cell No*	J_{sc} (mA/cm ²)	U_{oc} (V)	FF	Efficiency (%)
1	6.96	0.2820	0.3964	0.78
2	7.41	0.2813	0.3980	0.83
3	6.37	0.2635	0.3900	0.65
4	5.92	0.2673	0.3880	0.61
5	4.63	0.2571	0.3880	0.46
6	3.12	0.2780	0.3760	0.33
7	3.33	0.3040	0.3480	0.35

*Cell No indicates the count in number of cells for the example given

The extracted characteristic data from 7 solar cells shown in table 5.1 was used in plotting statistics for 89 such solar cells as shown in figure 5.27, which is a plot of open circuit voltage (U_{oc}), fill factor (FF) and conversion efficiency (η) as a function of short circuit current density (J_{sc}). From this figure it is observed that the fill factor and open circuit voltage have an average value of approximately 0.35 and 0.3 V, respectively for all values of short circuit current density, while conversion efficiency is observed to be

directly proportional to the short circuit current density values. The low values of FF and U_{oc} can be attributed to recombination of charge carriers as well as the effects of low shunt resistance in the solar cell.

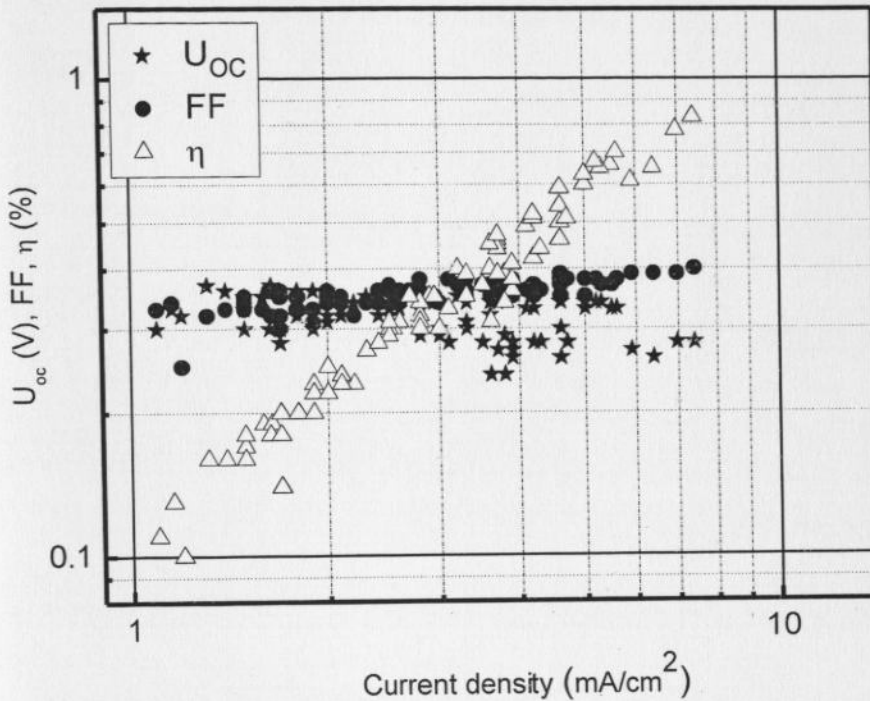


Figure 5.27: Statistics of 89 solar cells, plotted solar cell parameters are U_{oc} , FF and η as function of short circuit current density.

5.3.4 Structural analysis of the eta solar cell

Figure 5.28 shows photomicrograph of indium hydroxy sulphide modified eta solar cell cross sectional structure. The structure displayed is for the solar cell of the type $\text{SnO}_2:\text{F}/\text{TiO}_2/\text{In}(\text{OH})_x\text{S}_y/\text{Pb}(\text{OH})_x\text{S}_y/\text{PEDOT}:\text{PSS}/\text{Au}$. From the cross section, it is not possible to figure out clearly the thin $\text{In}(\text{OH})_x\text{S}_y$ and $\text{Pb}(\text{OH})_x\text{S}_y$ layers from the TiO_2 matrix, but PEDOT:PSS and Au back contact are clearly discernable at the top of the other layers as pointed out by the arrows. At the bottom of the coated thin film multilayer, the contacting $\text{SnO}_2:\text{F}$ layer is plainly noticeable as the even compact thin layer at the bottom directly in contact with the glass substrate. It is apparent from the photomicrograph in figure 5.28 that the chemical bath deposited buffer layer and the absorber material did not permeate and fill up the microporous TiO_2 matrix. Additionally, PEDOT:PSS is observed to form a continuous non-penetrating layer on top of the solar cell.

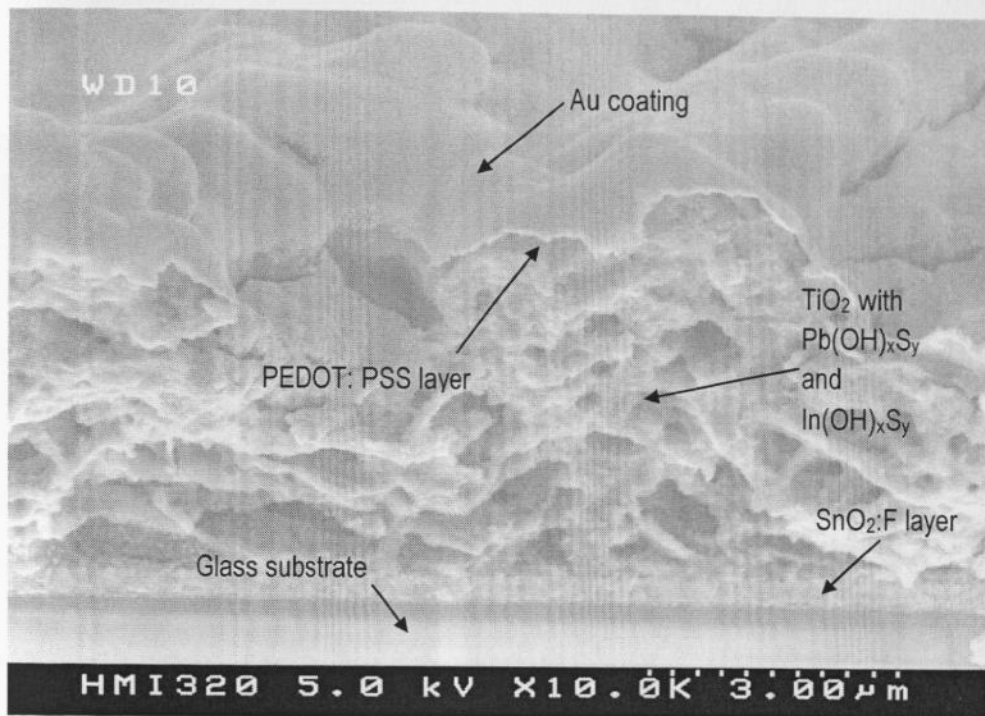


Figure 5.28: Cross-sectional structure of the eta solar cell of the type SnO₂:F/TiO₂/In(OH)_xS_y/Pb(OH)_xS_y/PEDOT:PSS/Au.

Figure 5.29 shows energy dispersive X-ray mapping of the eta solar cell device whose cross-sectional structure is displayed in figure 5.28. The distributions of elements from thin film material used in fabricating each layer in the solar cell are clearly seen. It is observed that the materials deposited using various techniques formed good coating without interfacial diffusion of the compositional elements. The coatings are distinguishable by the colour concentration; the faded part represents the reflections while the highly concentrated colour is the thin film (the figure is better viewed in soft copy or high pixel colour print). From figure 5.29, the following annotations are used: Au represents gold used in coating the back contact, Sn is the tin in the fluorine doped tin oxide, C is the carbon in PEDOT:PSS, Ti is the element titanium in TiO₂, Pb is the lead in the absorber material Pb(OH)_xS_y, and lastly, In is indium in the buffer layer material In(OH)_xS_y. The import of energy dispersive X-ray (EDX) mapping is to understand the extent of the stacked layer structure of the eta solar cell, and analyse whether material such as Au back contact had diffused during deposition and mixed with the bulk structure, in which case it can lead to existence of surface states and resultant photocurrent shunting in the solar cell.

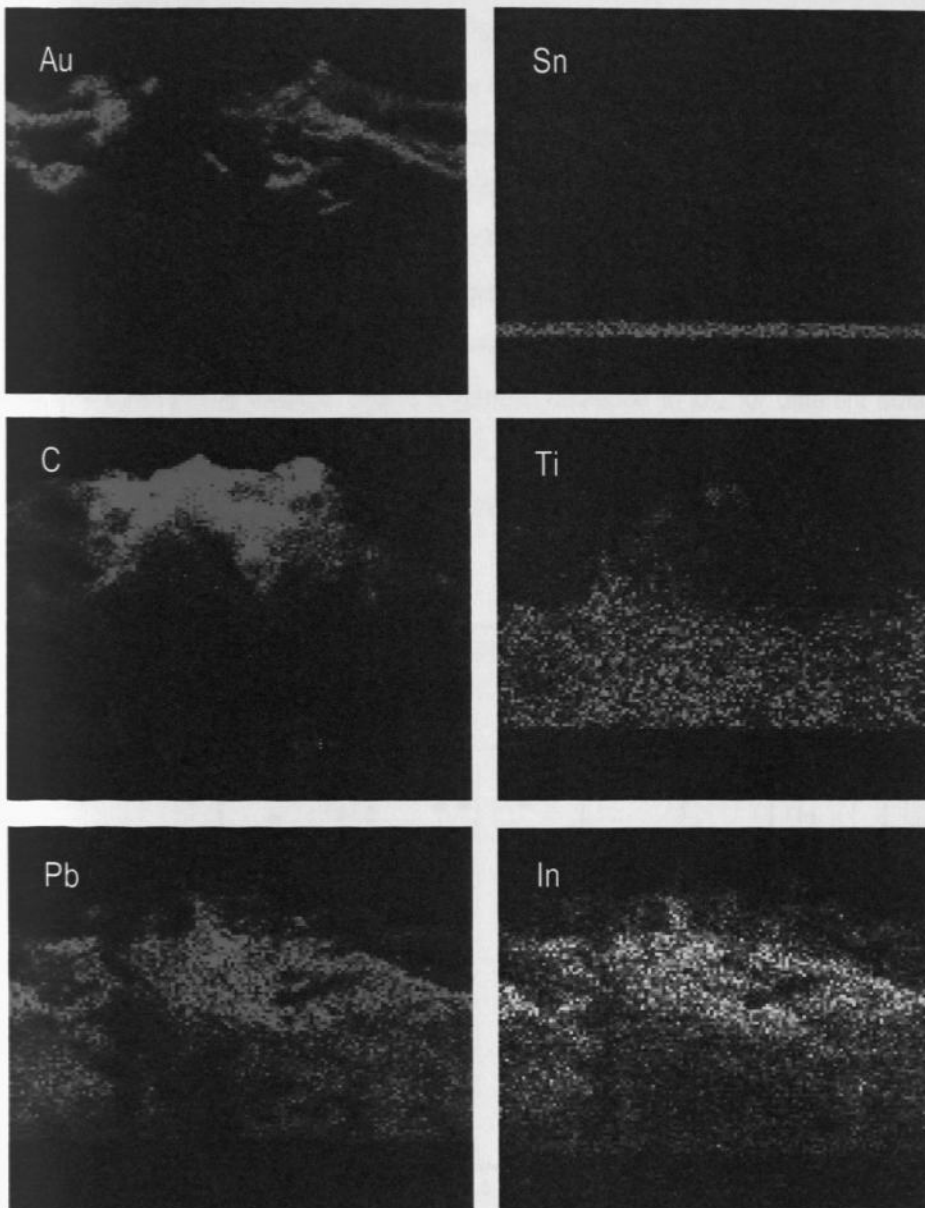


Figure 5.29: Energy dispersive X-ray mapping of the elemental composition in material of various layers used in fabricating eta solar cell, Au is element gold in Au back contact, Sn is tin in $\text{SnO}_2\text{:F}$ layer, C is carbon in PEDOT:PSS, Ti is element titanium in TiO_2 , Pb is lead in $\text{Pb(OH)}_x\text{S}_y$, and In is the element indium in $\text{In(OH)}_x\text{S}_y$.

5.3.5 Effect of thickness of various layers on the device performance.

The effect of varying thickness of the stacked multilayer of the $\text{In}(\text{OH})_x\text{S}_y$ modified eta solar cell is shown in figure 5.30 by U_{oc} , FF and η device parameters as a function of current density statistics. The numbers in parenthesis in $\text{TiO}_2(10)/\text{In}(\text{OH})_x\text{S}_y(3)/\text{Pb}(\text{OH})_x\text{S}_y(9)/\text{PEDOT:PSS}(2)/\text{Au}$ solar cell structure whose statistics are shown in figure 5.29, means that the respective layers were coated at that corresponding number of cycles following the deposition methods as described in chapter 4. In this section, the thickness of the sample was being controlled by the number of coating cycles. It should be noted here that the deposition technique referred to throughout this section for $\text{Pb}(\text{OH})_x\text{S}_y$ is SILAR (successive ion layer absorption and reaction). For easier interpretation of the data in figure 5.29, a dash-dot vertical line labeled H has been traced to show parameters of one of the cells, the values marked are $U_{oc} = 0.227$ V, FF = 0.356, $J_{sc} = 6.1$ mA/cm^2 , and $\eta = 0.49\%$. The diagram shows a general decrease in U_{oc} for different solar cells with a corresponding increase in FF and current density for the same solar cells. Despite the decrease in open circuit voltage, a high current density with corresponding high FF resulted in increase of conversion efficiency for the corresponding solar cells.

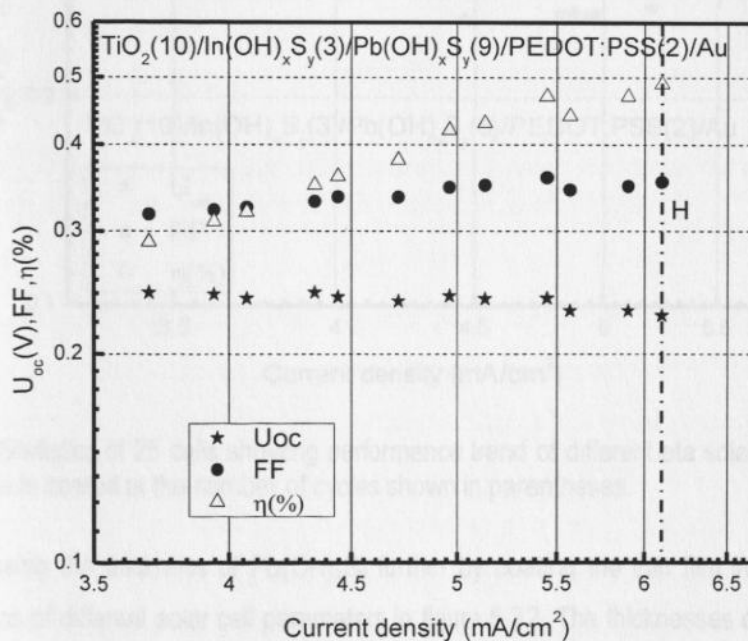


Figure 5.30: Statistics of 15 cells showing performance trend of eta solar cell when the layer thickness is coated at the number of cycles shown in parentheses. Dash-dot line H marks through parameters of one of the cells.

Figure 5.31 shows statistics of $\text{TiO}_2(10)/\text{In}(\text{OH})_x\text{S}_y(3)/\text{Pb}(\text{OH})_x\text{S}_y(6)/\text{PEDOT:PSS}(2)/\text{Au}$ structured solar cell. From the values in the parenthesis representing coating cycles, with the thicknesses of titanium dioxide, indium hydroxy sulphide and PEDOT:PSS kept constant while that of lead hydroxy sulphide was decreased to 6 dips. The fill factors of the solar cells from the statistics in figure 5.30 indicates it was fairly constant at approximately 0.37, Also, the open circuit voltage of the device remained constant at average value of about 0.3 V for current density $J_{sc} < 4.7 \text{ mA/cm}^2$ but for $J_{sc} > 4.8$ the U_{oc} decreases to 0.26 V average for different cells. The high conversion efficiency observed is due to the high short circuit current density recorded in those particular cells.

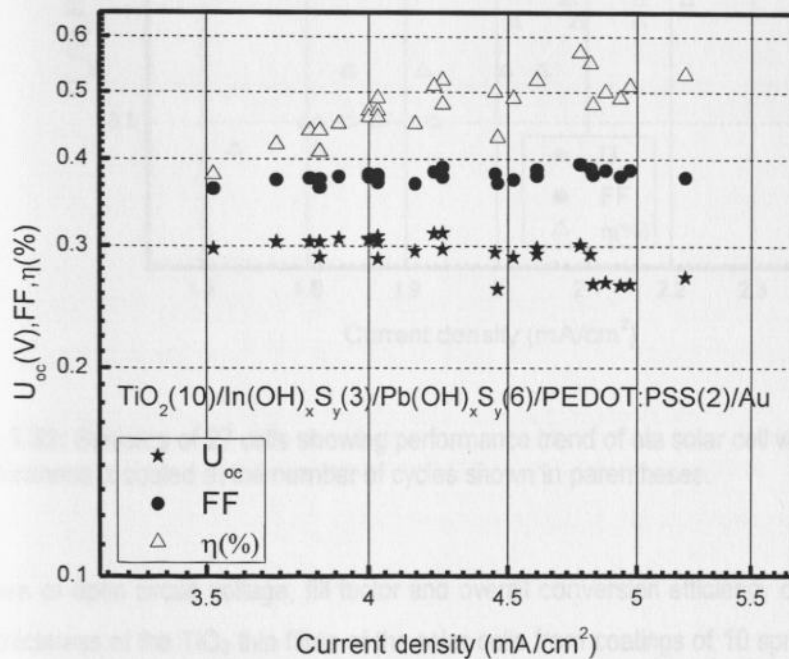


Figure 5.31: Statistics of 25 cells showing performance trend of different eta solar cells when the layer thickness is coated at the number of cycles shown in parentheses.

The effect of decreasing the thickness of $\text{Pb}(\text{OH})_x\text{S}_y$ further by coating the thin film in 3 cycles only is shown by the statistics of different solar cell parameters in figure 5.32. The thicknesses of TiO_2 , $\text{In}(\text{OH})_x\text{S}_y$ and PEDOT:PSS were maintained constant for the $\text{TiO}_2(10)/\text{In}(\text{OH})_x\text{S}_y(3)/\text{Pb}(\text{OH})_x\text{S}_y(6)/\text{PEDOT:PSS}(2)/\text{Au}$ structured solar cells. The fill factors of the solar cells were approximately constant at 0.43, while the open circuit voltages were approximately 0.38 V. The device recorded very low overall conversion efficiency

despite the high fill factor and open circuit voltage. The low conversion efficiencies are due to the low short circuit current density recorded from the devices.

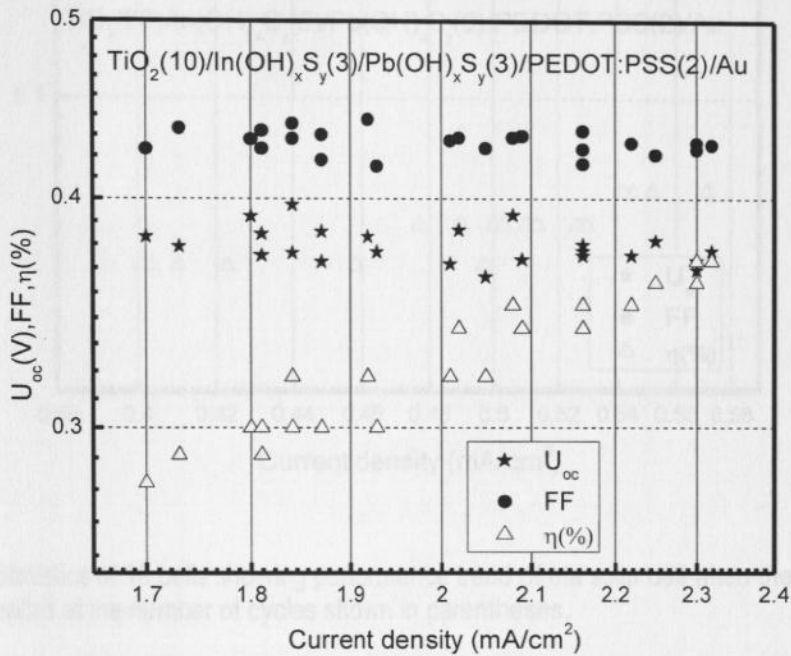


Figure 5.32: Statistics of 27 cells showing performance trend of eta solar cell when the layer thickness is coated at the number of cycles shown in parentheses.

The average values of open circuit voltage, fill factor and overall conversion efficiency decreased slightly after varying the thickness of the TiO₂ thin films of the solar cells from coatings of 10 sprays to 20 sprays, this is as depicted by statistics in figure 5.33, compare these statistics with those shown in figure 5.32. The FF and U_{oc} had an average value of approximately 0.36 and 0.28 V, respectively. The low conversion efficiency observed of approximately 0.05% for this type of device in spite of the high fill factor and high open circuit voltage may be attributed to the low short circuit current density recorded from the solar cells. In conclusion, it may be stated that varying thicknesses of the stacked multilayers in a solar cell affects the space charge region of the device leading to the changes in parameters like fill factor, open circuit voltage, short circuit current density and overall conversion efficiency.

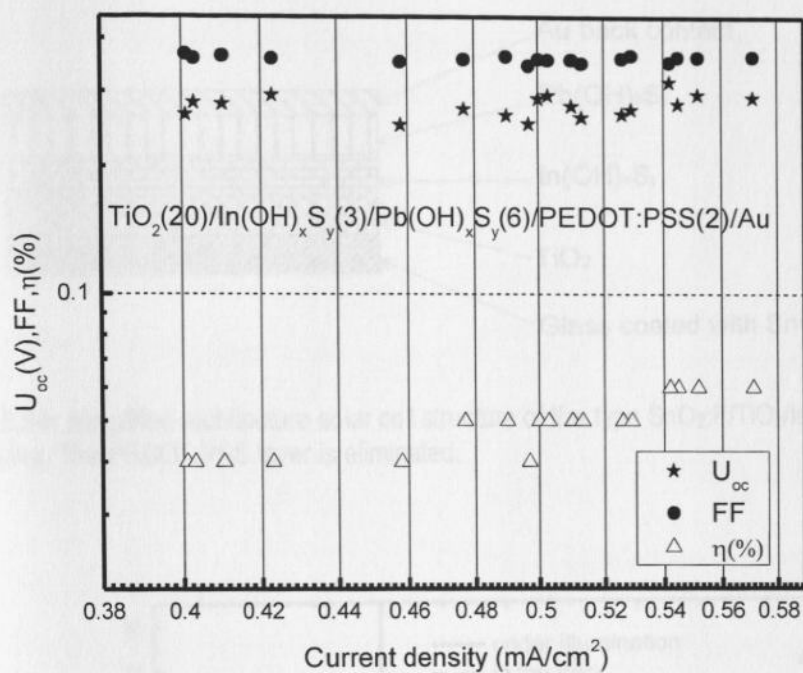


Figure 5.33: Statistics of 18 cells showing performance trend of eta solar cell when the layer thickness is coated at the number of cycles shown in parentheses.

5.3.6 The role of component materials in the eta solar cell heterostructure

In this section, the role of specific layer materials in the $\text{In(OH)}_x\text{S}_y$ modified eta solar cell is elucidated. This is achieved by use of devices with simplified architectures by applying the layer elimination method and then analysing the resulting solar cells' photoelectrical properties.

5.3.6.1 J – U characteristics of $\text{SnO}_2:\text{F}/\text{TiO}_2/\text{In(OH)}_x\text{S}_y/\text{Pb(OH)}_x\text{S}_y/\text{Au}$ device

The solar cell structure shown in figure 5.34 of the type $\text{SnO}_2:\text{F}/\text{TiO}_2/\text{In(OH)}_x\text{S}_y/\text{Pb(OH)}_x\text{S}_y/\text{Au}$ was realised after eliminating PEDOT:PSS from the full device discussed in section 5.3.3. The photovoltaic parameters performance are shown using J – U characteristics in figure 5.35. The device fill factor and open circuit voltage were approximately 0.4 and 0.34 V, respectively. The short circuit current density was about 6.16 mA/cm² and the overall conversion efficiency was approximately 0.94%. The calculated series (R_{se}) and shunt resistance (R_{sh}) were 38.4 Ω and 24452.0 Ω , respectively.

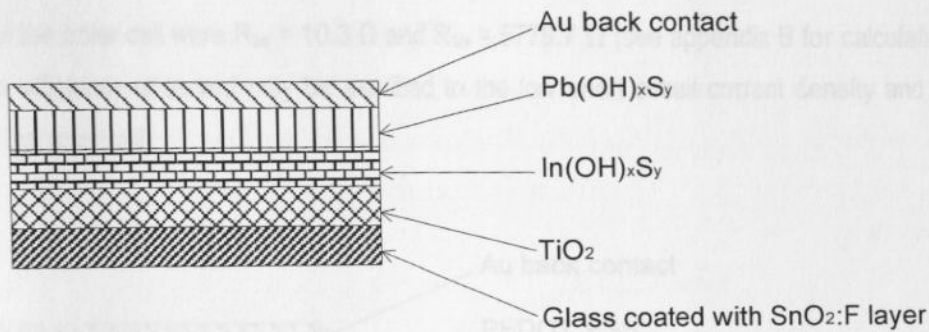


Figure 5.34: Simplified architecture solar cell structure of the type SnO₂:F/TiO₂/In(OH)_xS_y/In(OH)_xS_y/Au. The PEDOT:PSS layer is eliminated.

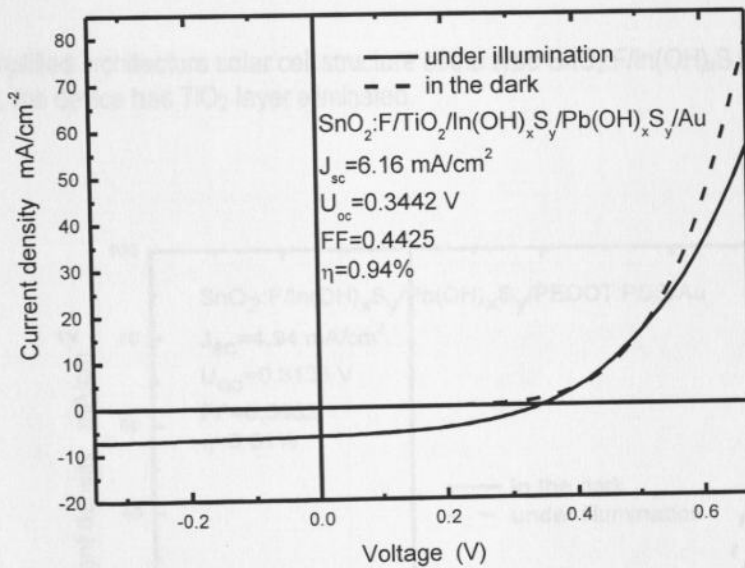


Figure 5.35: J - U characteristics for SnO₂:F/TiO₂/In(OH)_xS_y/Pb(OH)_xS_y/Au solar cell structure shown in figure 5.34.

5.3.6.2 J - U characteristics of SnO₂:F/In(OH)_xS_y/Pb(OH)_xS_y/PEDOT:PSS/Au device

The solar cell with SnO₂:F/In(OH)_xS_y/Pb(OH)_xS_y/PEDOT:PSS/Au structure is shown in figure 5.35. In the device displayed, TiO₂ has been eliminated from the full In(OH)_xS_y modified eta solar cell. The performance of the simplified device is given by the J - U characteristics as shown in figure 5.36. The following values were recorded: J_{sc} = 4.94, U_{oc} = 0.31, FF = 0.40, and conversion efficiency of 0.61%. The calculated

parasitic resistant of the solar cell were $R_{se} = 10.3 \Omega$ and $R_{sh} = 5779.7 \Omega$ (see appendix B for calculation). The low conversion efficiency observed may be ascribed to the low short circuit current density and low shunt resistance in the solar cell.

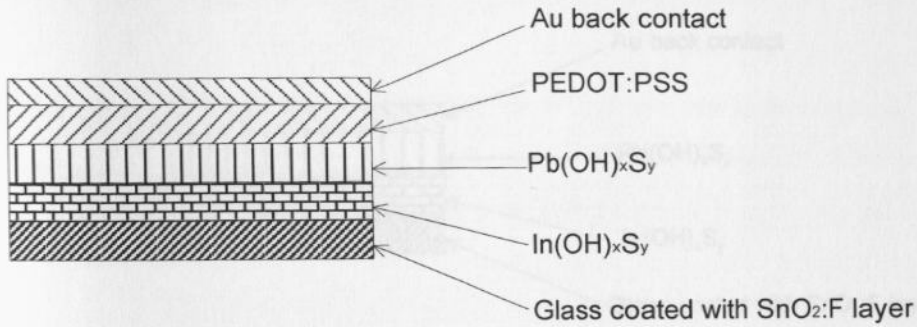


Figure 5.36: Simplified architecture solar cell structure of the type SnO₂:F/In(OH)_xS_y/In(OH)_xS_y/PEDOT:PSS/Au, the device has TiO₂ layer eliminated.

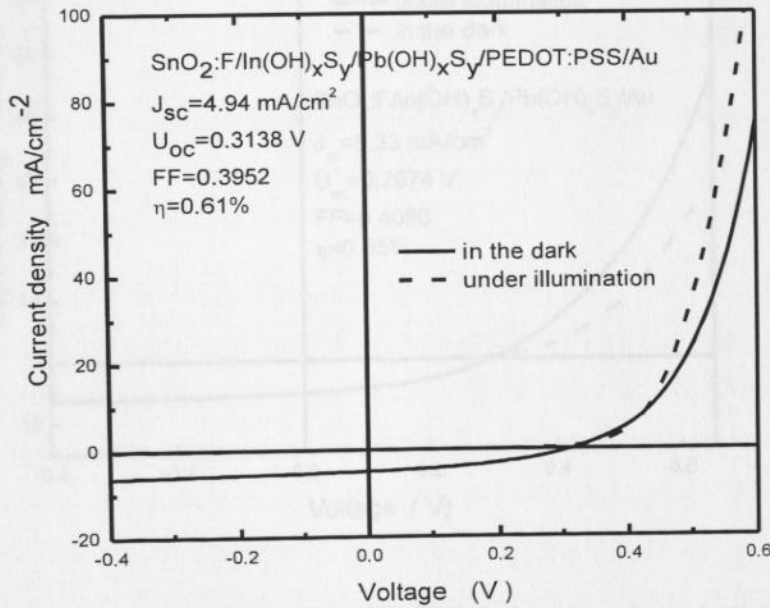


Figure 5.37: J - U characteristics of SnO₂:F/In(OH)_xS_y/Pb(OH)_xS_y/PEDOT:PSS/Au solar cell structure shown in figure 5.36.

5.3.6.3 J - U characteristics of $\text{SnO}_2\text{:F}/\text{In}(\text{OH})_x\text{S}_y/\text{Pb}(\text{OH})_x\text{S}_y/\text{Au}$ device

Figure 5.38 shows the most simplified working p - n junction type of device whereby only two layers have been used to assemble a solar cell of the type $\text{SnO}_2\text{:F}/\text{In}(\text{OH})_x\text{S}_y/\text{Pb}(\text{OH})_x\text{S}_y/\text{Au}$ structure. The corresponding J - U characteristics for the device are shown in figure 5.39.

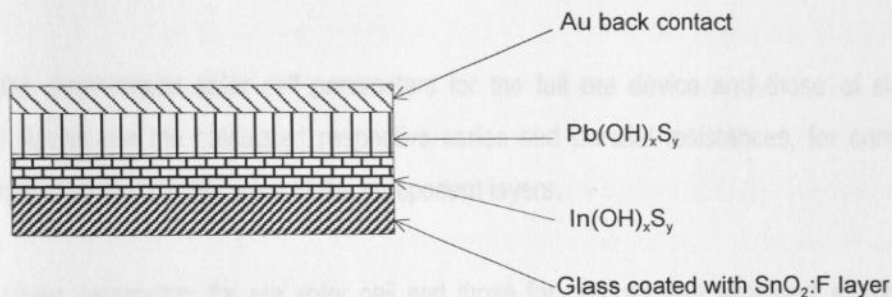


Figure 5.38: Simplified architecture solar cell structure of the type $\text{SnO}_2\text{:F}/\text{In}(\text{OH})_x\text{S}_y/\text{Pb}(\text{OH})_x\text{S}_y/\text{Au}$. The device has TiO₂ and PEDOT:PSS layers eliminated.

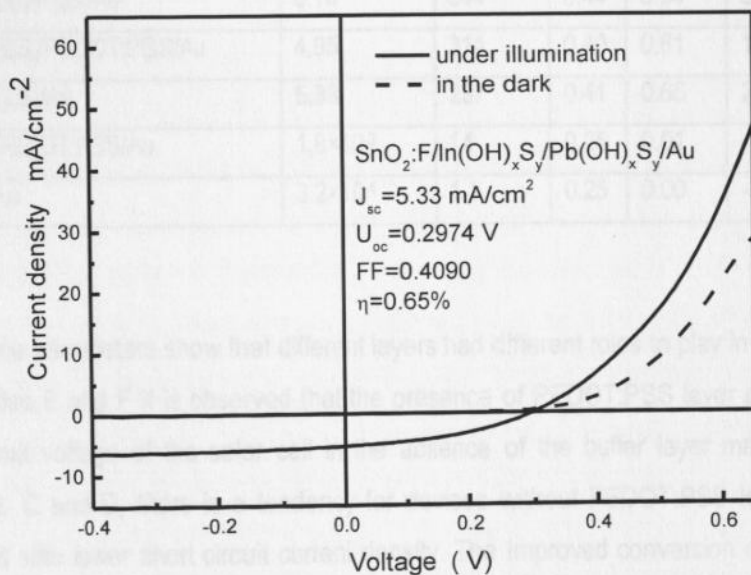


Figure 5.39: J - U characteristics of $\text{SnO}_2\text{:F}/\text{In}(\text{OH})_x\text{S}_y/\text{Pb}(\text{OH})_x\text{S}_y/\text{Au}$ solar cell structure shown in figure 5.38.

The p - n junction type of solar cell with TiO₂ and PEDOT:PSS layers eliminated realised short circuit current density and open circuit voltage of approximately 5.33 mA/cm² and 0.3 V, respectively, with good fill factor of about 0.4. The overall conversion efficiency of the device was 0.65% and the calculated series resistance of the solar cell was 23.8 Ω. For the shunt resistance, there was no clear value obtained. This may be attributed to the fact that the device was found to be a two diode type with $A_{i1} = 6.1$ and $A_{i2} = 2.0$.

Table 5.2 shows the summarised solar cell parameters for the full eta device and those of simplified architectures. Also shown are the calculated respective series and parallel resistances, for comparison purposes and in explaining the specific roles of the component layers.

Table 5.2: Photovoltaic parameters for eta solar cell and those for devices with simplified structures for explaining specific roles of the component layers.

Device	Photovoltaic device structure	J _{sc} (mA/cm ²)	U _{oc} (mV)	FF	Eff(%)	R _{se}	R _{sh}
A	TiO ₂ /In(OH) _x S _y /Pb(OH) _x S _y /PEDOT:PSS/Au	7.40	281	0.40	0.83	47.4	4759.0
B	TiO ₂ /In(OH) _x S _y /Pb(OH) _x S _y /Au	6.16	344	0.44	0.94	38.4	24452.0
C	In(OH) _x S _y /Pb(OH) _x S _y /PEDOT:PSS/Au	4.95	314	0.40	0.61	10.2	5779.7
D	In(OH) _x S _y /Pb(OH) _x S _y /Au	5.33	297	0.41	0.65	23.8	-
E	TiO ₂ /Pb(OH) _x S _y /PEDOT:PSS/Au	1.8×10 ⁻³	14	0.25	0.01	-	-
F	TiO ₂ /Pb(OH) _x S _y /Au	3.2×10 ⁻⁴	1.1	0.25	0.00	-	-

From Table 5.2, the device parameters show that different layers had different roles to play in the whole eta device. Comparing devices E and F it is observed that the presence of PEDOT:PSS layer plays a role in improving the open circuit voltage of the solar cell in the absence of the buffer layer material, but on comparing devices A, B, C and D, there is a tendency for devices without PEDOT:PSS to have higher conversion efficiency but with lower short circuit current density. The improved conversion efficiency may be attributed to the improved fill factors in both cases as observed from devices A – B and C – D after eliminating PEDOT:PSS in each case. The observed behaviour can be linked to the bulk resistance and inherent low conductivity in polymer materials. The positive attribute of PEDOT:PSS is that, it acts as protective layer of the Pb(OH)_xS_y against diffusion of the Au back contact atoms into the bulk of the device structure which would otherwise shunt the device in the event of high applied voltage during J – U characteristics measurements.

The role of TiO_2 can be explained by comparing devices A and C which had similar structures save for the presence or absence of TiO_2 layer. In both samples, similar fill factors are observed, the open circuit voltages are also comparable, but the short circuit current density of device C is 35% lower than that of device A. Thus, TiO_2 seems to provide increased surface area resulting in better optoelectrical properties, as well as playing the role of reducing recombination at the $\text{SnO}_2\text{:F}/\text{In}(\text{OH})_x\text{S}_y$ interface. Likewise the role of $\text{In}(\text{OH})_x\text{S}_y$ layer can be deduced by comparing devices A, B, C, D, E and F. Devices E and F recorded the poorest device parameter characteristics, unlike devices A, B, C and D which all contain the $\text{In}(\text{OH})_x\text{S}_y$ layer. It can be concluded that, $\text{In}(\text{OH})_x\text{S}_y$ acts as the recombination barrier in devices fabricated. Also by comparing devices D and F, it is apparent that charge separation occurs at the interface between $\text{In}(\text{OH})_x\text{S}_y$ and $\text{Pb}(\text{OH})_x\text{S}_y$ corroborating results of the external quantum efficiency measurement shown in figure 5.25.

5.4 Effects of light soaking on eta solar cell.

In this section results on the effect of light soaking and stability of eta solar cell and those of devices with reduced number of layers are discussed.

5.4.1 $\text{SnO}_2\text{:F}/\text{TiO}_2/\text{In}(\text{OH})_x\text{S}_y/\text{Pb}(\text{OH})_x\text{S}_y/\text{PEDOT:PSS}/\text{Au}$ performance

The performance of $\text{SnO}_2\text{:F}/\text{TiO}_2/\text{In}(\text{OH})_x\text{S}_y/\text{Pb}(\text{OH})_x\text{S}_y/\text{PEDOT:PSS}/\text{Au}$ eta solar cell soaked in solar simulator light beam for 120 minutes is displayed in figure 5.40. The characteristics of solar cell parameters that is fill factor, open circuit voltage (U_{oc}) and efficiency (η) as a function of light soaking duration in minutes are plotted in the same graph. The conversion efficiency of the solar cell is observed to have an exponential increment from $\eta = 0.13\%$ for as-prepared device to as high as $\eta = 0.33\%$ after light soaking for 2 hours, equivalent to an increment factor of 2.5. On the other hand, the corresponding short circuit current density increased by a factor of 2.8 from $J_{sc} = 2.1 \text{ mA/cm}^2$ to $J_{sc} = 5.9 \text{ mA/cm}^2$. The fill factor of the device is observed to gradually increase from a minimum value of 0.29 and reaches a maximum value of 0.34 after 45 minutes of light soaking, and then it gradually decreased to 0.33 after 120 minutes of light soaking. Likewise, the U_{oc} of the solar cell gradually decreased from a value of 0.21 V to minimum value of 0.17 V after 120 minutes of light soaking.

A similar structured one week old device tested for light soaking effect gave results plotted in figure 5.41. The conversion efficiency and short circuit current density increased from $\eta = 0.80$ to 0.94% and $J_{sc} = 10.1$ to 13.0 mA/cm^2 , respectively, while both fill factor and U_{oc} decreased slightly.

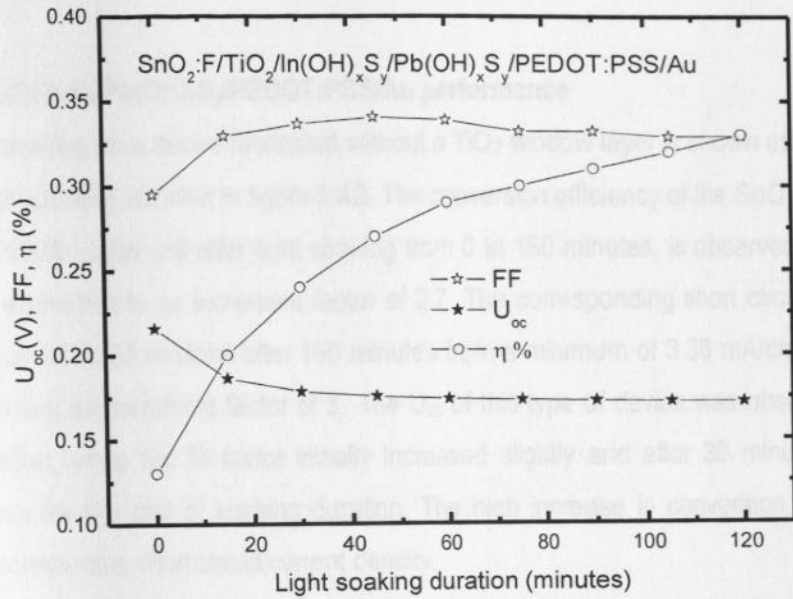


Figure 5.40: Light soaking characteristics for $\text{SnO}_2\text{:F/TiO}_2\text{/In(OH)}_x\text{S}_y\text{/Pb(OH)}_x\text{S}_y\text{/PEDOT:PSS/Au}$ eta solar cell, U_{oc} , FF and η are plotted as function of light soaking duration.

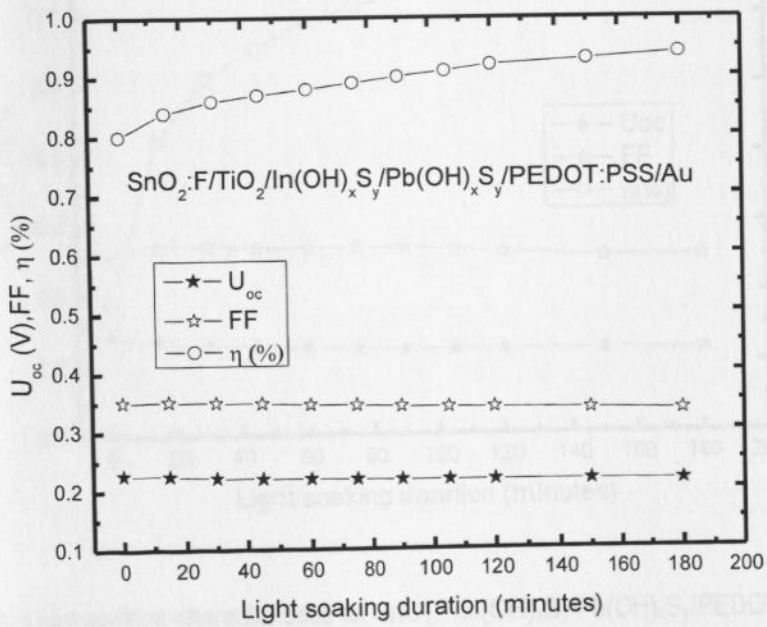


Figure 5.41: Light soaking characteristics for $\text{SnO}_2\text{:F/TiO}_2\text{/In(OH)}_x\text{S}_y\text{/Pb(OH)}_x\text{S}_y\text{/PEDOT:PSS/Au}$ of one week old eta solar cell, U_{oc} , FF and η are plotted as function of light soaking duration.

5.4.2 SnO₂:F/In(OH)_xS_y/Pb(OH)_xS_y/PEDOT:PSS/Au performance

The effect of light soaking on a device fabricated without a TiO₂ window layer is shown using U_{oc}, FF and η as a function of light soaking duration in figure 5.42. The conversion efficiency of the SnO₂:F/In(OH)_xS_y/Pb(OH)_xS_y/PEDOT:PSS/Au solar cell after light soaking from 0 to 180 minutes, is observed to increase from 0.29% to 0.78%, equivalent to an increment factor of 2.7. The corresponding short circuit current density reached a maximum of 10.09 mA/cm² after 180 minutes from a minimum of 3.36 mA/cm² for as-prepared solar cell, representing an increment factor of 3. The U_{oc} of this type of device was observed to decrease with soaking duration, while the fill factor initially increased slightly and after 30 minutes of soaking, it started to decrease for the rest of soaking duration. The high increase in conversion efficiency can be attributed to the increment in short circuit current density.

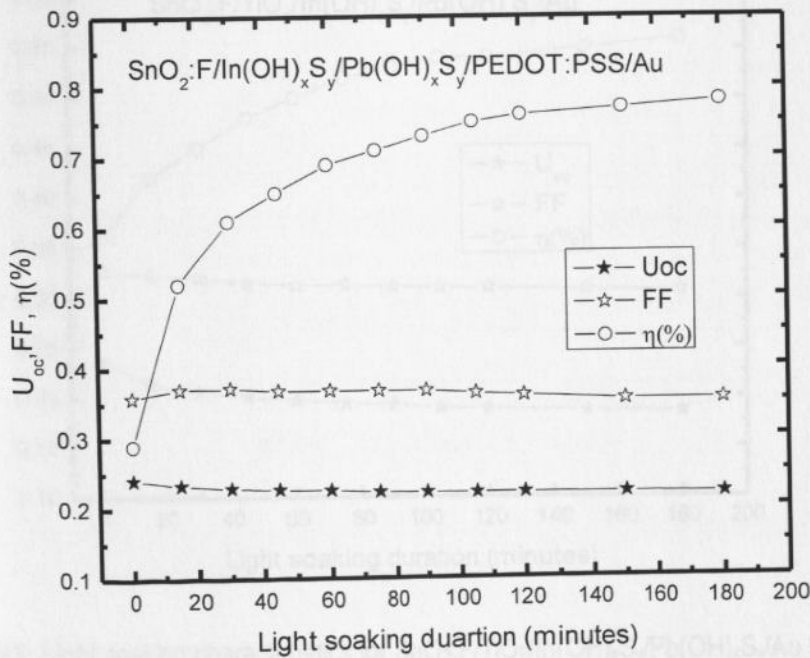


Figure 5.42: Light soaking characteristics for SnO₂:F/In(OH)_xS_y/Pb(OH)_xS_y/PEDOT:PSS/Au solar cell, U_{oc}, FF and η are plotted as function of light soaking duration.

5.4.3 SnO₂:F/TiO₂/In(OH)_xS_y/Pb(OH)_xS_y/Au performance

Open circuit voltage, fill factor and efficiency as a function of light soaking duration for a device without a PEDOT:PSS layer with SnO₂:F/In(OH)_xS_y/Pb(OH)_xS_y/Au structure is shown in figure 5.43. The conversion efficiency of this type of solar cell increased from a minimum of 0.36% for as prepared solar cell to a maximum of 0.56% after soaking in light for 180 minutes, representing increment factor of 1.6, while short circuit current density increased by a factor of 2.1 from 4.72 mA/cm² for as prepared sample to 9.87 mA/cm² after 180 minutes of light soaking. Both open circuit voltage and FF displayed a decrement by a factor of 0.03 and 0.01, respectively. The increment in short circuit current density of this type of device lead to the observed increase in overall conversion efficiency.

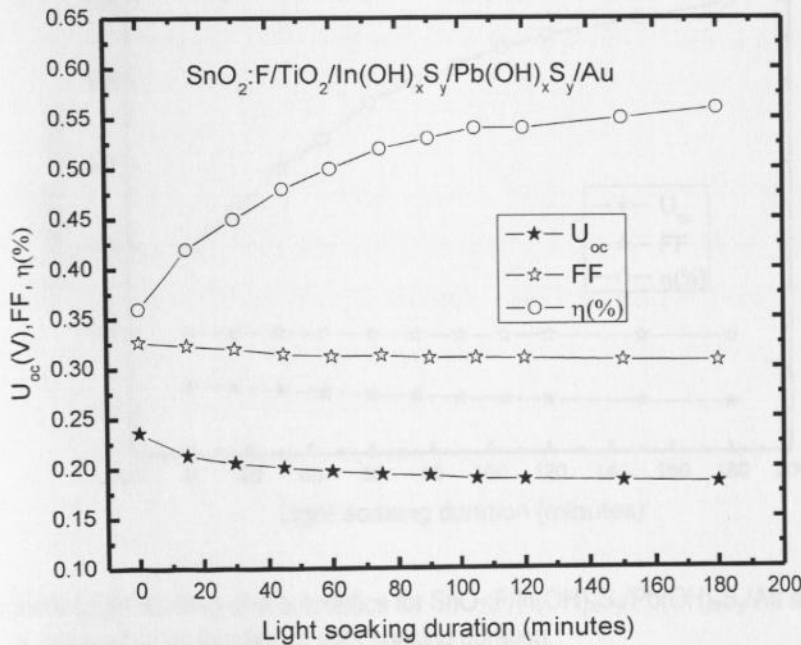


Figure 5.43: Light soaking characteristics for SnO₂:F/TiO₂/In(OH)_xS_y/Pb(OH)_xS_y/Au solar cell. U_{oc}, FF and η are plotted as function of light soaking duration.

5.4.4 SnO₂:F/In(OH)_xS_y/Pb(OH)_xS_y/Au performance

Lastly, the solar cell device with the simplest configuration of p – n heterojunction structure of the type SnO₂:F/In(OH)_xS_y/Pb(OH)_xS_y/Au was subjected to light soaking test, and exposed to solar simulator beam calibrated at 1 sun = 100 mW/cm² from 0 – 180 minutes. The J – U characteristics parameters shown in

figure 5.44 were taken at 15 minutes interval for the first 120 minutes and at 30 minutes interval for the rest of duration of soaking. For this type of device, the open circuit voltage and fill factor were observed to decrease with increasing light soaking duration, while the short circuit current density and solar cell conversion efficiency changed by a factor of about 2.5 and 2.0, respectively. The maximum value reached after 180 minutes of light soaking was $J_{sc} = 14.32 \text{ mW/cm}^2$ from initial value of about 5.69 mW/cm^2 for as prepared solar cell, whereas the corresponding conversion efficiency for the same duration increased from $\eta = 0.60\%$ to $\eta = 1.19\%$.

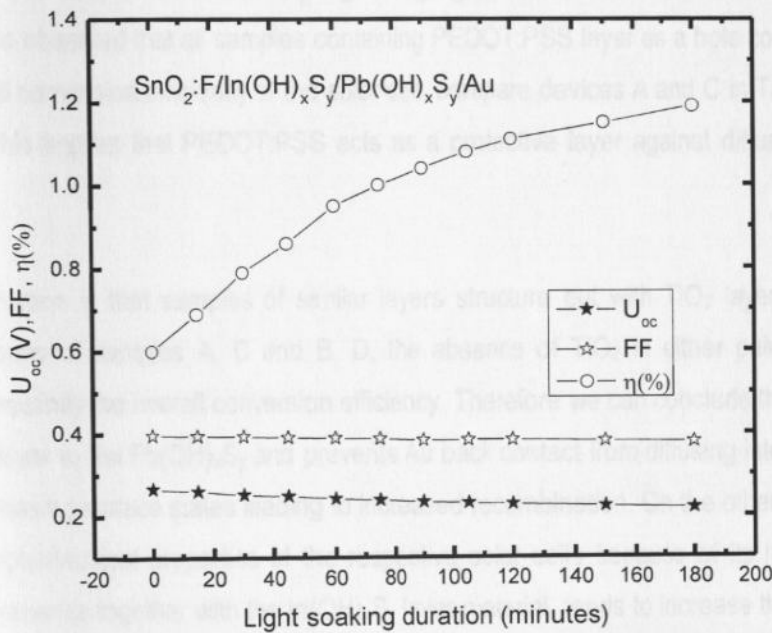


Figure 5.44: Light soaking characteristics for $\text{SnO}_2:\text{F}/\text{In}(\text{OH})_x\text{S}_y/\text{Pb}(\text{OH})_x\text{S}_y/\text{Au}$ solar cell, U_{oc} , FF and η are plotted as function of light soaking duration.

From the light soaking experiments for full eta solar cell modified with a buffer layer and simplified solar cell devices with reduced number of layers, Table 5.3 can be extracted to simplify the analysis procedure. The results show that light soaking has a strong influence on the solar cells overall conversion efficiency and short circuit current density for devices containing $\text{In}(\text{OH})_x\text{S}_y/\text{Pb}(\text{OH})_x\text{S}_y$ layers as the basic structure. The parameters have been observed to increase with light soaking duration since after 180 minutes of samples' exposure to the solar simulator light beam, both efficiency and short circuit current density increased by

Table 5.3: Changes in photovoltaic parameters of eta solar cell and those of simplified devices

Solar cell	Photovoltaic device structure	J_{sc} (mA/cm ²)	U_{oc} (mV)	FF	Eff(%)
A	SnO ₂ :F/TiO ₂ /In(OH) _x S _y /Pb(OH) _x S _y /PEDOT:PSS/Au	2.8	D	I - D	2.5
B	SnO ₂ :F/TiO ₂ /In(OH) _x S _y /Pb(OH) _x S _y /Au	2.1	D	D	1.6
C	SnO ₂ :F/In(OH) _x S _y /Pb(OH) _x S _y /PEDOT:PSS/Au	3	D	I - D	2.7
D	SnO ₂ :F/In(OH) _x S _y /Pb(OH) _x S _y /Au	2.5	D	D	2.0

D* represents decrement in the particular solar cell parameter, I - D* depicts increase then decrease

a factor of between ~ 2 and 3, which is a very big change given the initial values for as-prepared solar cells. Clearly, it can be observed that all samples containing PEDOT:PSS layer as a hole conductor had the highest gain in overall conversion efficiency of the solar cell, compare devices A and C in Table 5.3 against samples B and D. This implies that PEDOT:PSS acts as a protective layer against diffusion of Au back contact.

An interesting observation is that samples of similar layers structure but with TiO₂ layer eliminated, for example, compare pairs of samples A, C and B, D, the absence of TiO₂ in either pair resulted in J_{sc} increment and consequently the overall conversion efficiency. Therefore we can conclude that PEDOT:PSS acts as a protective layer to the Pb(OH)_xS_y and prevents Au back contact from diffusing into the bulk of the material thereby increasing surface states leading to increased recombination. On the other hand, although TiO₂ improves the optoelectrical properties of the respective solar cells because of its highly structured porous surface, its presence together with the In(OH)_xS_y layer material, tends to increase the space charge region such that recombination losses can set in. We conclude that, the charge transport in these types of devices is controlled by trap states due to the increased space charge region making the probability of defects states and interface states higher. This reasoning corroborates work previously done by Oja, *et. al.*, (2005).

5.4.5 Degradation study of SnO₂:F/In(OH)_xS_y/Pb(OH)_xS_y/PEDOT:PSS/Au device

In section 5.4.1, figure 5.41, it was observed that eta solar cell is stable to degradation under room environment. One week after measurements of J - U characteristics, the samples' short circuit current density and conversion efficiency increased by a factor of 1.3 and 1.2, respectively after the device was subjected to light soaking for 180 minutes. The behaviour observed inspired us to conduct degradation

studies after light soaking. An as-prepared solar cell device similar to that represented by device C in Table 5.3, was analysed by optoelectrical method using external quantum efficiency (EQE) measurements, as shown in figure 5.45. The EQE measurements were done first for as-prepared samples, thereafter the samples were soaked in light for 180 minutes (3 hours) using standard solar simulator calibrated to 1 sun = 100 mW/cm². After light soaking the EQE was measured and found to have increased to 25% (peak wavelength $\lambda = 540$ nm) from the initial value for as-prepared solar cells of about EQE = 17% (peak wavelength $\lambda = 510$ nm). The EQE was then monitored after 24 hours and 96 hours and found to have dropped to 23% (peak wavelength $\lambda = 530$ nm) and 21% (peak wavelength $\lambda = 520$ nm), respectively.

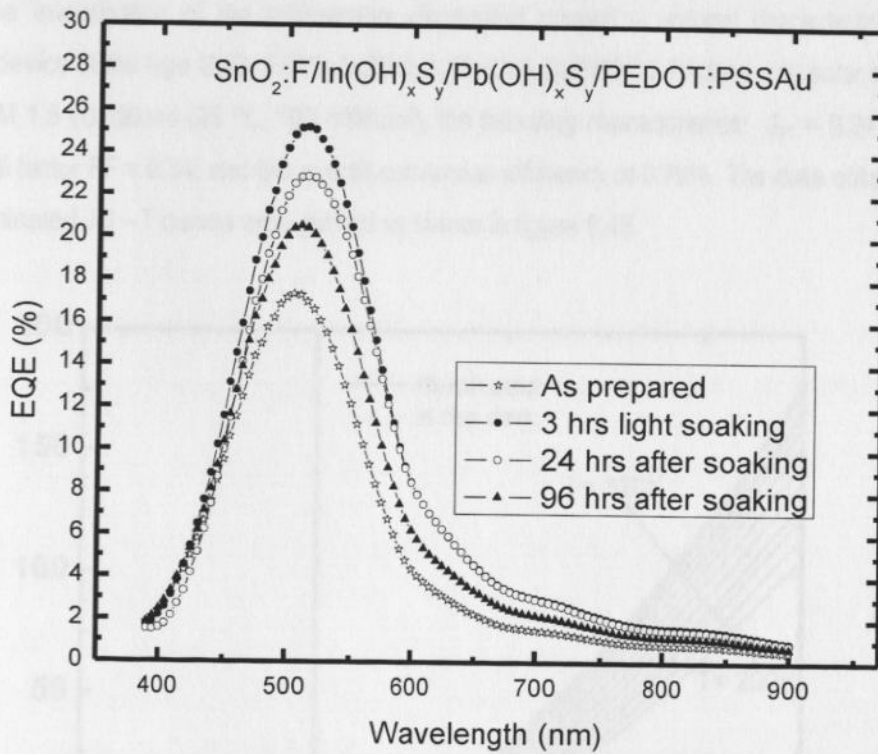


Figure 5.45: External Quantum efficiency characteristics for SnO₂:F/In(OH)_xS_y/Pb(OH)_xS_y/PEDOT:PSS/Au solar cell devices. EQE spectrums shown were used in monitoring degradation after light soaking.

The variations in EQE may not be attributed to changes in band gap since all the EQE curves start cutting (the onset of wavelength signal) from approximately the same wavelength of about 400 nm. The device stability is supported by the slow degradation of the EQE spectrum, and the resilience of optoelectrical properties upon re-soaking the sample in solar simulator light. It can be concluded that, eta solar cell and

devices based on $\text{In}(\text{OH})_x\text{S}_y/\text{Pb}(\text{OH})_x\text{S}_y$ basic structure can have their optoelectrical properties improved by light soaking. At this juncture it remains unclear to us the particular material responsible for the observed changes in these type of devices and this calls for further investigation.

5.5 JU – T characterization of eta solar cell.

Current transport mechanism were studied in order to understand the type of recombination taking place in the full eta solar cell device. The $\text{In}(\text{OH})_x\text{S}_y$ modified eta solar cell was chosen for JU – T characterization since it was observed to have good stability and therefore suitable for the analysis of transport mechanisms. The investigation of the temperature dependent current – voltage characterization was carried out for a device of the type $\text{SnO}_2:\text{F}/\text{TiO}_2/\text{In}(\text{OH})_x\text{S}_y/\text{Pb}(\text{OH})_x\text{S}_y/\text{PEDOT}:\text{PSS}/\text{Au}$, eta solar cell, which showed under AM 1.5 conditions (25°C , $100\text{ mW}/\text{cm}^2$), the following characteristics: $J_{\text{sc}} = 9.24\text{ mW}/\text{cm}^2$, $U_{\text{oc}} = 0.25\text{ V}$, a fill factor $\text{FF} = 0.34$, and the overall conversion efficiency of 0.79% . The data obtained from the dark and illuminated JU – T curves were plotted as shown in figure 5.46.

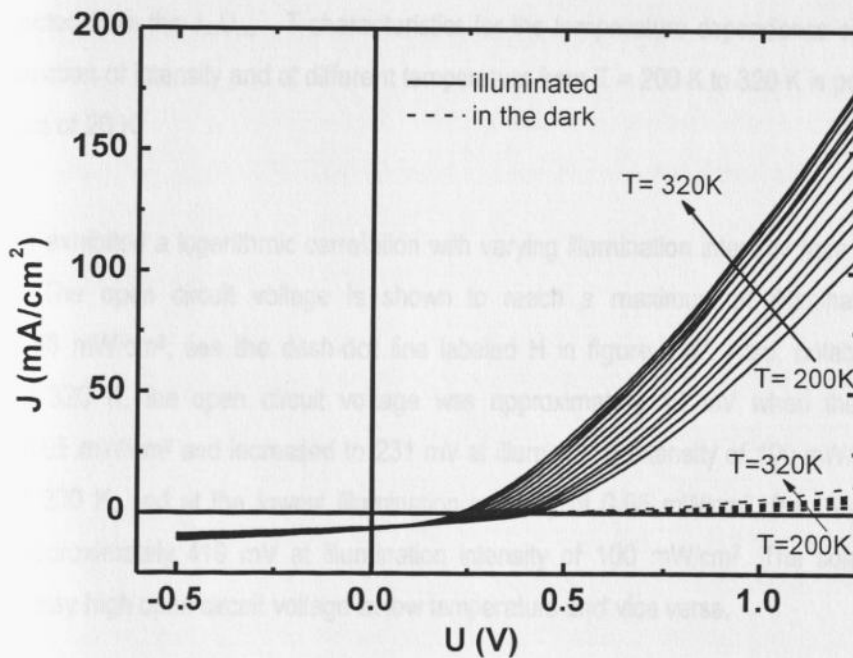


Figure 5.46: Current - voltage characterization in the dark and under illumination at different temperatures in the range 200 - 320 K in steps of 20 K from one curve to the other.

The $JU - T$ and $J_{sc}U_{oc} - T$ curves plotted were data collected at different temperatures, from 200 K – 320 K in steps of 20 K from one curve to the other. Significant differences are apparent between the dark and illuminated $JU - T$ and $J_{sc}U_{oc} - T$ curves. Nonetheless, the curves in all the cases can be fitted to the one-diode model described in chapter 3, the equation is restated in 5.1.

$$J_m = J_o \left(\exp \left(\frac{q(U_m - J_m R_s)}{A_i k T} \right) - 1 \right) + \frac{U_m - J_m R_s}{R_p} - J_{ph} \quad 5.1$$

It is worth mentioning here for clarity that the $JU - T$ and $J_{sc}U_{oc} - T$ characteristics curves shown in figure 5.46 were chosen for those of the same light intensity that is 100 mW/cm² but at different temperatures, since it is not easy to plot $J - U$ curves at different temperatures and at the same time at various light intensities in a shared graph. This applies in the subsequent subsections.

5.5.1 Intensity dependency characterization

The data extracted from the $J_{sc}U_{oc} - T$ characteristics for the temperature dependence of the open circuit voltage as a function of intensity and at different temperature from $T = 200$ K to 320 K is presented in figure 5.47, at intervals of 20 K.

The U_{oc} curves exhibited a logarithmic correlation with varying illumination intensity from 0.05 mW/cm² to 100 mW/cm². The open circuit voltage is shown to reach a maximum at illumination intensity of approximately 45 mW/cm², see the dash-dot line labeled H in figure 5.47. Also, notable is that at the temperature of 320 K, the open circuit voltage was approximately 46 mV when the solar cell was illuminated at 0.05 mW/cm² and increased to 231 mV at illumination intensity of 100 mW/cm². Likewise at temperature of 200 K, and at the lowest illumination intensity of 0.05 mW/cm², the $U_{oc} = 284$ mV, and increased to approximately 419 mV at illumination intensity of 100 mW/cm². The solar cell device is observed to display high open circuit voltage at low temperature and vice versa.

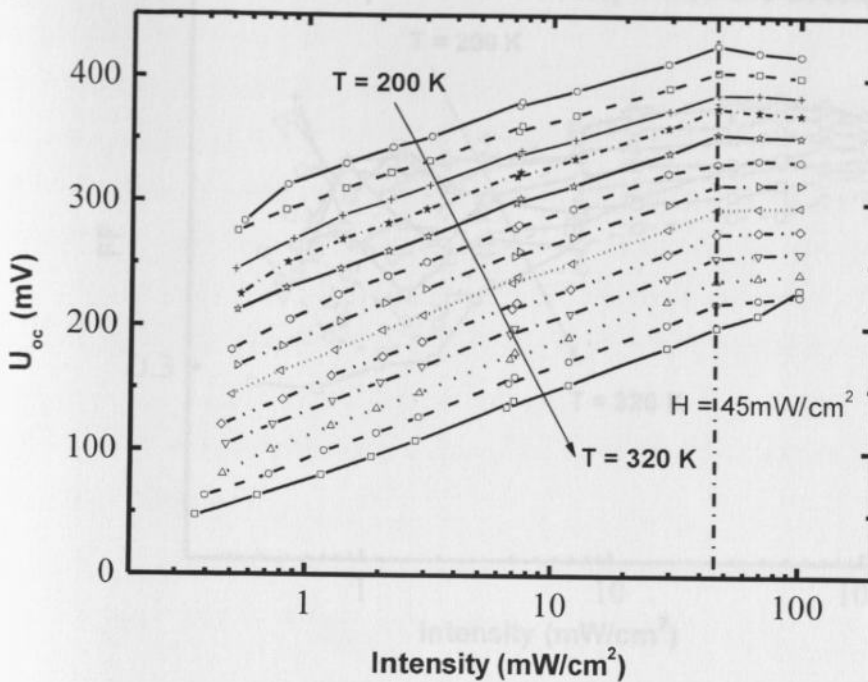


Figure 5.47: Open circuit voltage (U_{oc}) as a function of illumination intensity and at different temperature. The data is plotted at temperature intervals of 20 K.

The corresponding fill factor of the eta solar cell plotted as a function of illumination intensity and at different temperatures is shown in figure 5.48. The fill factors of the eta cell are observed to be inconsistent at different temperatures and illumination intensities. The fill factors varied between 0.30 and 0.36, a small dependency on illumination intensity and temperature.

The overall conversion efficiency of the eta solar cell at different temperatures and at various illumination intensities is shown in figure 5.49. The conversion efficiency displays a logarithmic correlation with the illumination intensity. From figure 5.49, it is observed that at the lowest intensity of 0.05 mW/cm^2 and at the highest temperature of 320 K, the conversion efficiency increased from its lowest value of approximately 0.09% to 0.55% at 200K, while at maximum illumination intensity of 100 mW/cm^2 , the efficiency increased from 0.53% at temperature of 320 K to its maximum value of 0.85% at temperature of 200 K. This shows that temperature has a strong influence on the device conversion efficiency. Also noteworthy is that the kind of influence light intensity has on the device conversion efficiency is different as it was the case when the samples were soaked in light.

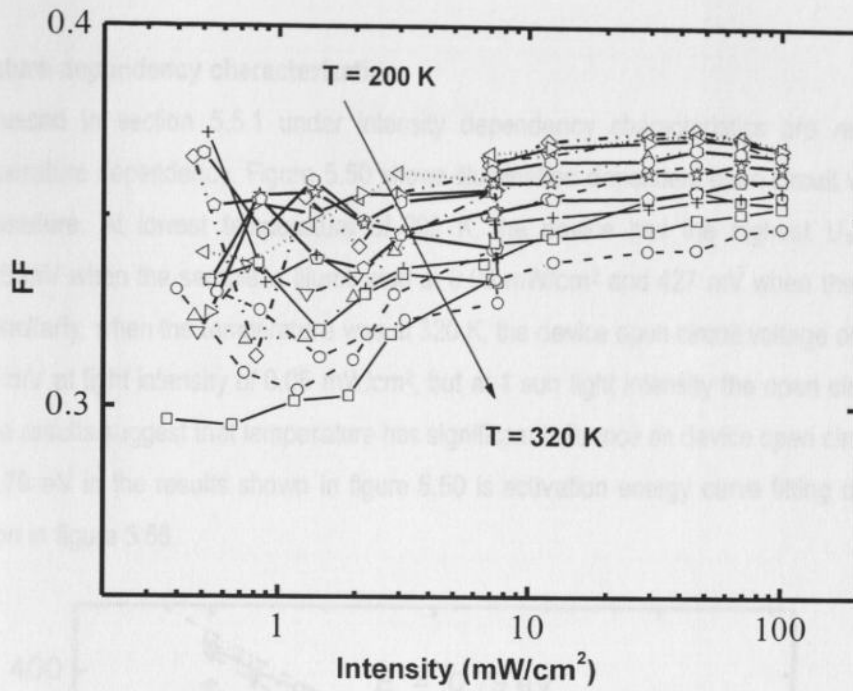


Figure 5.48: Temperature dependence of fill factor as a function of illumination intensity. Measurements are done from 200 K – 320 K at intervals of 20 K.

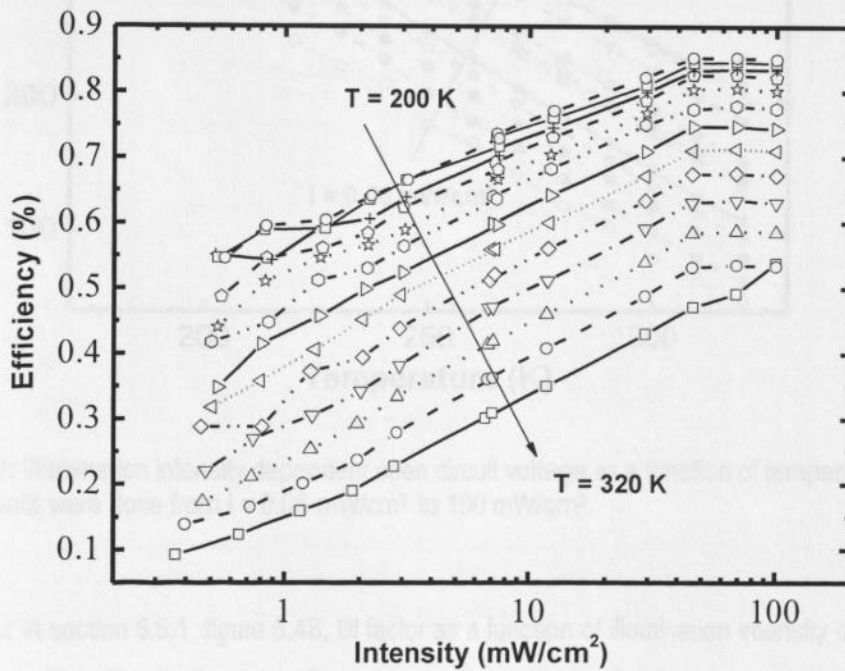


Figure 5.49: Temperature dependency of conversion efficiency as a function of illumination intensity. Measurements were done from 200 K - 320 K at intervals of 20 K.

5.5.2 Temperature dependency characterization

The results discussed in section 5.5.1 under intensity dependency characteristics are revisited and analysed for temperature dependency. Figure 5.50 shows illumination dependent open circuit voltage as a function of temperature. At lowest temperature of 200 K, the device had the highest U_{oc} values of approximately 285 mV when the sample is illuminated at 0.05 mW/cm^2 and 427 mV when the intensity is raised to 1 sun. Similarly, when the temperature was at 320 K, the device open circuit voltage obtained was approximately 46 mV at light intensity of 0.05 mW/cm^2 , but at 1 sun light intensity the open circuit voltage $U_{oc} = 229 \text{ mV}$. The results suggest that temperature has significant influence on device open circuit voltage. The inset $E_a = 0.79 \text{ eV}$ in the results shown in figure 5.50 is activation energy curve fitting discussed in subsequent section in figure 5.56.

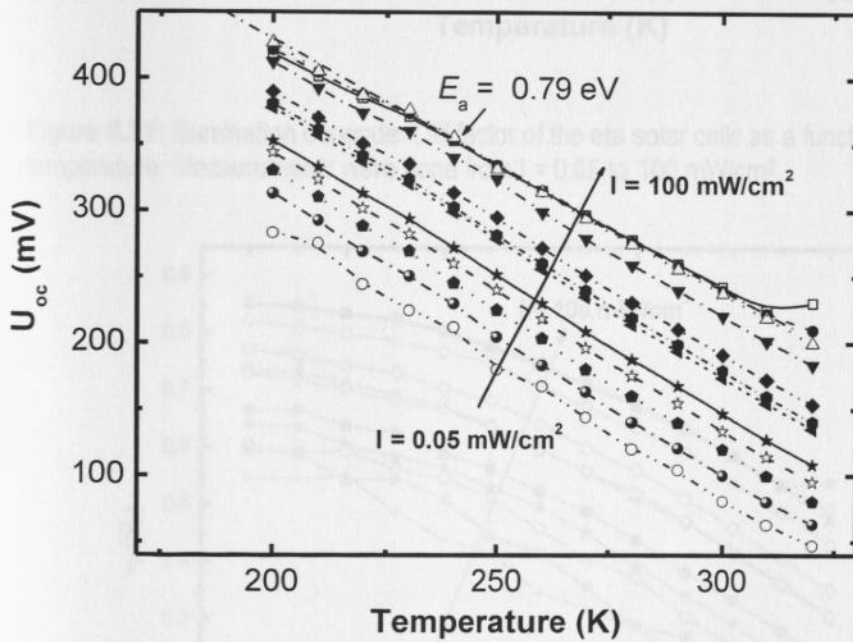


Figure 5.50: Illumination intensity dependent open circuit voltage as a function of temperature. Measurements were done from $I = 0.05 \text{ mW/cm}^2$ to 100 mW/cm^2 .

As observed earlier in section 5.5.1, figure 5.48, fill factor as a function of illumination intensity did not have any dependency on either illumination intensity or temperature; this is also the case as shown in figure 5.51. The fill factor at some points of illumination intensity and temperature, it was not consistent. Figure 5.52 displays illumination intensity dependence of conversion efficiency of the eta solar cell as a function of

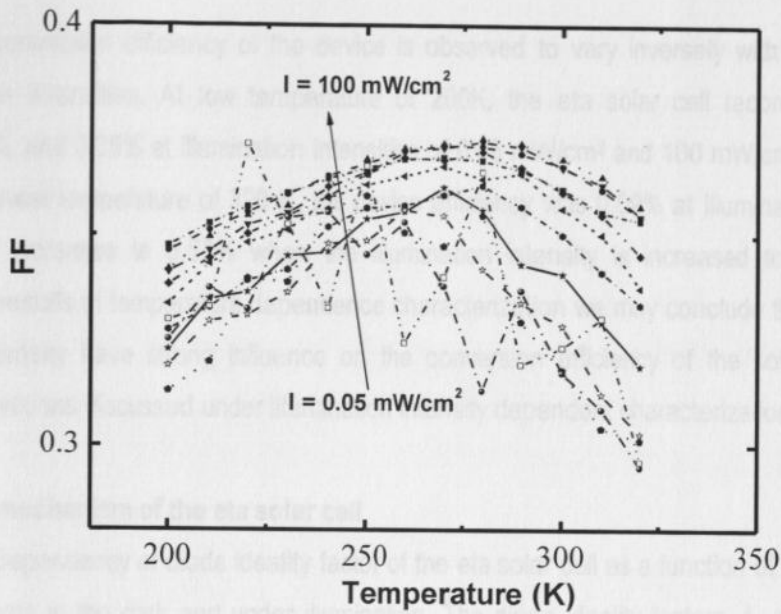


Figure 5.51: Illumination dependent fill factor of the eta solar cells as a function of temperature. Measurements were done from $I = 0.05$ to 100 mW/cm^2 .

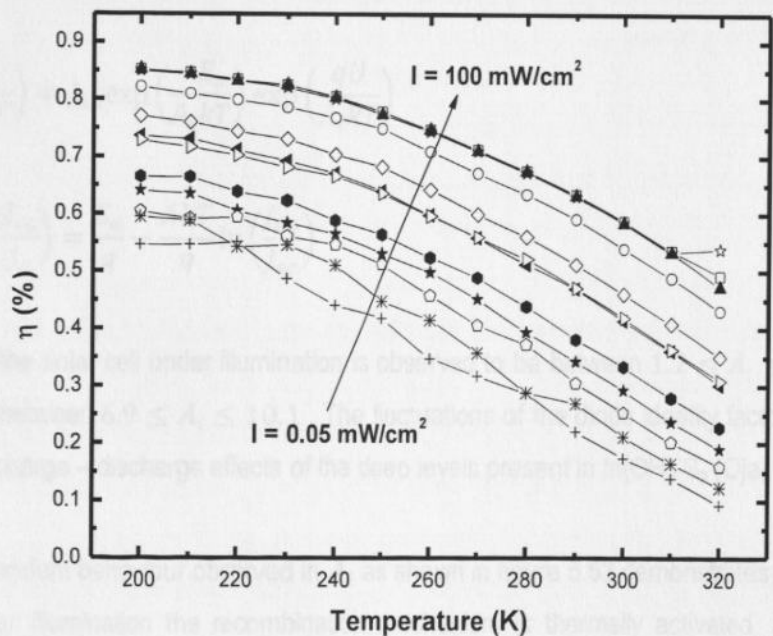


Figure 5.52: Illumination dependence of conversion efficiency of the eta solar cells as a function of temperature. Measurements were done from $I = 0.05$ to 100 mW/cm^2 .

temperature. The conversion efficiency of the device is observed to vary inversely with temperature at different illumination intensities. At low temperature of 200K, the eta solar cell recorded conversion efficiencies of 0.54% and 0.85% at illumination intensities of 0.05 mW/cm² and 100 mW/cm², respectively. Likewise, at the highest temperature of 320 K, the device efficiency was 0.09% at illumination intensity of 0.05 mW/cm² and increases to 0.53% when the illumination intensity is increased to 100 mW/cm². Therefore from the results of temperature dependence characterization we may conclude that temperature and illumination intensity have strong influence on the conversion efficiency of the solar cell devices corroborating observations discussed under illumination intensity dependent characterizations.

5.5.3 Transport mechanism of the eta solar cell

Figure 5.53 shows dependency of diode ideality factor of the eta solar cell as a function of temperature for $JU - T$ measurements in the dark and under illumination. The diode ideality factors A_i and the reverse saturation current density J_o of the eta solar cell were determined by fitting the dark $JU - T$ and illuminated $J_{sc}U_{oc} - T$ curves into equation 5.1 and 5.2: (NB. These equations appear in chapter 3 as equation 3.25 and 3.26, respectively)

$$J = J_o \exp\left(\frac{qU}{A_i kT}\right) = J_{oo} \exp\left(\frac{-E_a}{A_i kT}\right) \exp\left(\frac{qU}{A_i kT}\right) \quad 5.2$$

$$U_{oc} \approx \frac{A_i kT}{q} \ln\left(\frac{J_{sc}}{J_o}\right) = \frac{E_a}{q} - \frac{A_i kT}{q} \ln\left(\frac{J_{oo}}{J_{sc}}\right) \quad 5.3$$

The ideality factor of the solar cell under illumination is observed to be between $1.2 \leq A_i \leq 1.6$, while in the dark the value is between $6.9 \leq A_i \leq 10.1$. The fluctuations of the diode ideality factors in the latter case are ascribed to charge – discharge effects of the deep levels present in $\text{In}(\text{OH})_x\text{S}_y$ (Oja, *et. al.*, 2006).

The temperature dependent behaviour observed in A_i as shown in figure 5.53 demonstrates that, when the eta solar cell is under illumination the recombination mechanism is thermally activated, and when the sample is in the dark, the charge carriers undergoes tunneling enhanced recombination (Rusu, *et. al.*, 2003; Musembi, *et. al.*, 2008). The ideality factor A_i is observed to decrease as the temperature increases from approximately 1.6 at 200 K to ~ 1.2 at 320 K, which shows that the recombination occurs through

exponentially distributed energy recombination levels (Walter, *et. al.*, 1996). Therefore, when the sample is under illumination and exposed to high temperature, recombination occurs through shallow levels ($A_i \sim 1$), whereas at low temperature, deep levels are responsible.

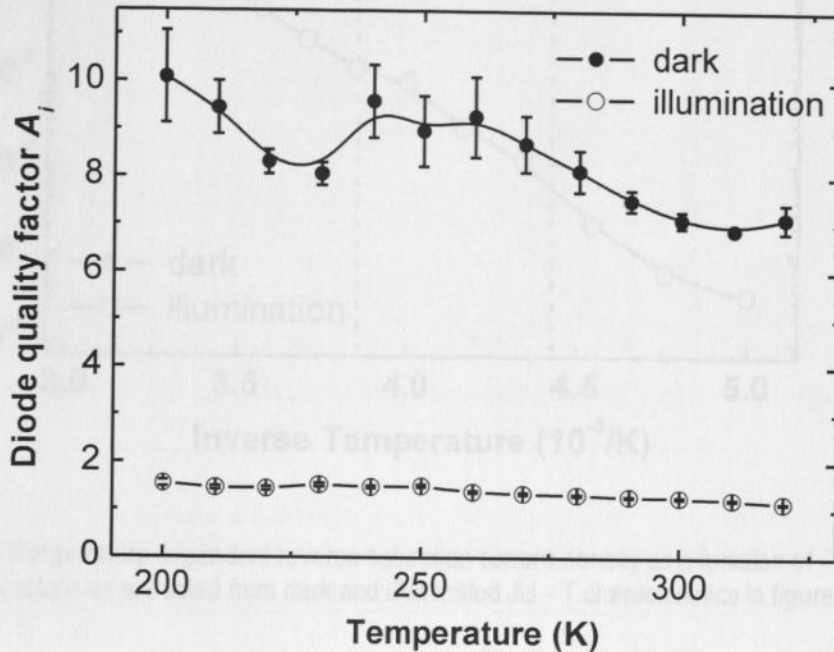


Figure 5.53: Temperature dependence of the diode ideality factor as extracted from dark $JU - T$ curves and $J_{sc}U_{oc} - T$ curves in figure 5.46.

The findings that recombination mechanism in the eta solar cell is a tunneling dominated process when the device is in the dark and thermally dominated under illumination are supported by the temperature behaviour of saturation current density J_o as a function of temperature as is shown in figure 5.54. From the figure (in the dark) it is observed that the $J_o = f(1/T)$ curve has two regions I and II where saturation current densities are independent of the inverse temperatures confirming the tunneling assisted recombination mechanisms. On the other hand, it is also noticeable that, under illumination, the reverse saturation current density J_o is inversely proportional to the inverse temperature which verifies that a thermally activated mechanism dominates the recombination of the charge carriers.

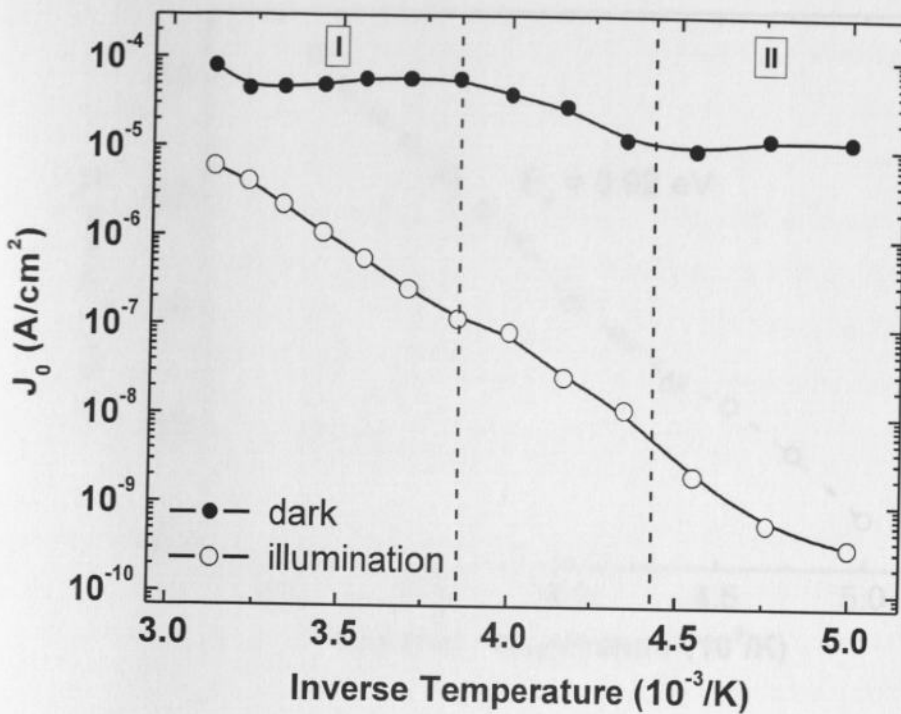


Figure 5.54: Temperature dependent reverse saturation current density as a function of inverse temperature as extracted from dark and illuminated $JU - T$ characteristics in figure 5.46.

Figure 5.55 shows a modified Arrhenius plot of the reverse saturation current density J_o corrected by diode ideality factor A_i , such that $A_i * \ln(J_o)$ as a function of inverse temperature $1/T$, as extracted from the illuminated $JU - T$ characteristics as in figure 5.46. The Arrhenius plot yields a straight line with a slope corresponding to the activation energy $E_a = 0.92$ eV.

The activation energy can also be determined from open circuit voltage as a function of temperature ($U_{oc} = f(T)$) plots in figure 5.56. Plotting U_{oc} as a function of temperature and assuming that the ideality factor A_i , reverse saturation current density J_o and the weakly temperature dependent prefactor J_{oo} are independent of temperature as expressed in equation 5.3, then a linear extrapolation to $T = 0$ K gives the activation energy $E_a = 0.79$ eV.

$$A_i \ln J_o = -\frac{E_a}{kT} + A_i \ln J_{oo} \quad 5.3$$

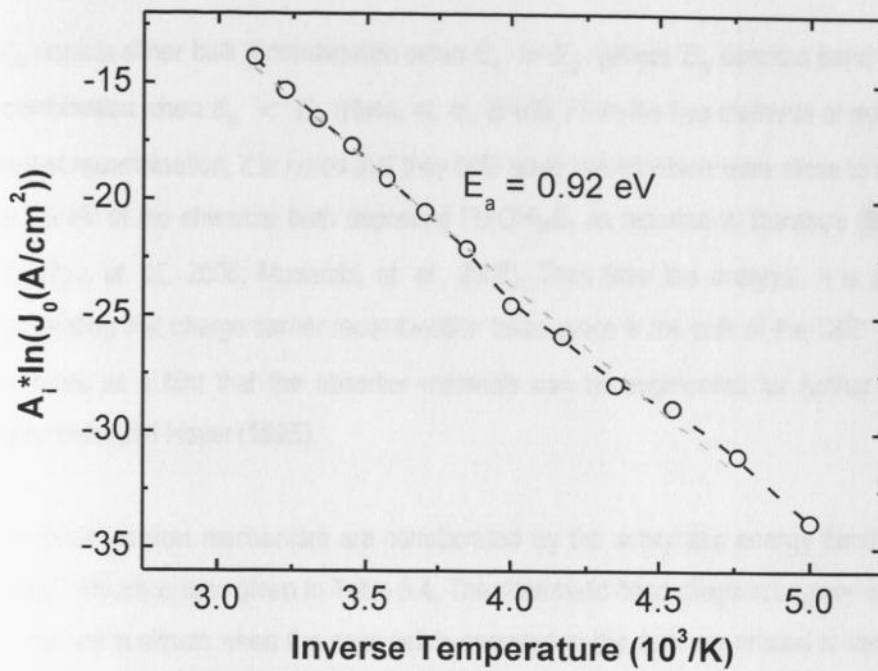


Figure 5.55: Arrhenius plot of the saturation current density J_0 corrected by diode ideality factor A_i with the data extracted from illuminated characteristics as extracted from figure 5.46.

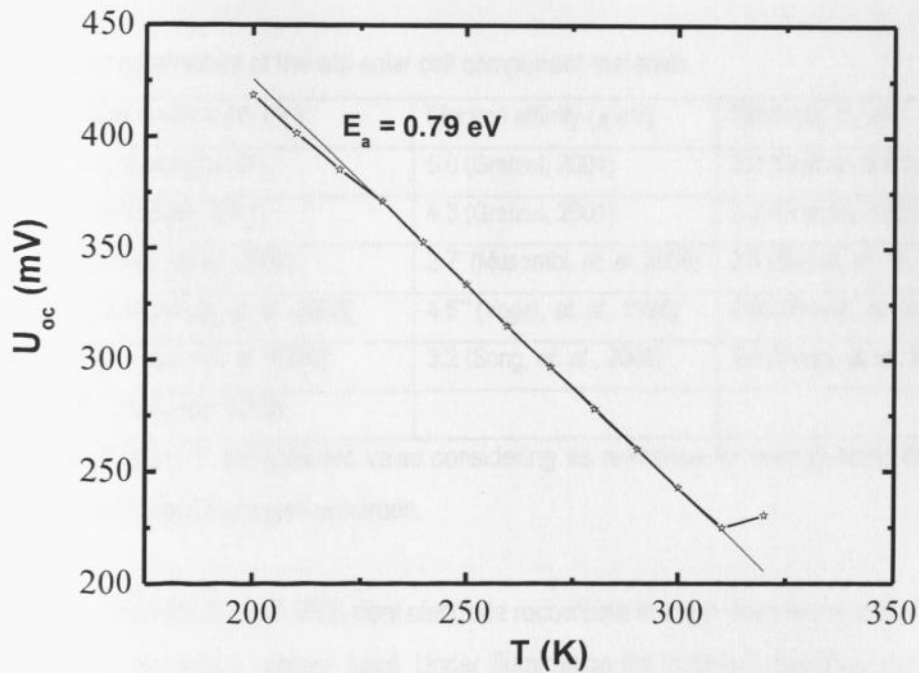


Figure 5.56: Activation energy of recombination derived from open circuit voltage U_{oc} as a function of temperature.

The value of E_a depicts either bulk recombination when $E_a = E_g$ (where E_g denotes band gap energy), or interface recombination when $E_a < E_g$ (Rusu, *et. al.*, 2003). From the two methods of determining the activation energy of recombination, it is noted that they both gave values which were close to the band gap energy $E_g = 0.85$ eV of the chemical bath deposited $\text{Pb}(\text{OH})_x\text{S}_y$ as reported in literature (Bayon, *et. al.*, 2005; 2006; Gavrilov, *et. al.*, 2006; Musembi, *et. al.*, 2008). Thus from the analysis, it is apparent that $E_a \approx E_g$ demonstrating that charge carrier recombination takes place in the bulk of the CBD – $\text{Pb}(\text{OH})_x\text{S}_y$. The conclusion gives us a hint that the absorber materials can be engineered for further widening as reported by Konenkamp and Hoyer (1995).

The findings on recombination mechanism are corroborated by the schematic energy band diagram we proposed by use of reference data given in Table 5.4. The schematic band diagram is given in figure 5.57. Thus the strong tunneling effects when the solar cell is operated in the dark are related to the presence of (i) a cliff in the conduction band at the $\text{TiO}_2/\text{In}(\text{OH})_x\text{S}_y$ interface (ii) a spike in the $\text{In}(\text{OH})_x\text{S}_y$ conduction band, and (iii) the deep recombination levels exponentially distributed in energy in the $\text{In}(\text{OH})_x\text{S}_y$ band gap (Oja, *et. al.*, 2006).

Table 5.4: Electronic parameters of the eta solar cell component materials.

Material	Work function (Φ eV)	Electron affinity (χ eV)	Band gap E_g (eV)
$\text{SnO}_2:\text{F}$	4.5 (Gratzel, 2001)	5.0 (Gratzel, 2001)	3.8 (Gratzel, 2001)
TiO_2	4.5 (Gratzel, 2001)	4.3 (Gratzel, 2001)	3.2 (Gratzel, 2001)
$\text{In}(\text{OH})_x\text{S}_y$	4.7 (Oja, <i>et. al.</i> , 2006)	3.7* (Musembi, <i>et. al.</i> , 2008)	2.4 (Bayon, <i>et. al.</i> , 2005)
$\text{Pb}(\text{OH})_x\text{S}_y$	5.0 (Musembi, <i>et. al.</i> , 2008)	4.5** (Vogel, <i>et. al.</i> , 1994)	0.85 (Bayon, <i>et. al.</i> , 2005)
PEDOT:PSS	5.2 (Brown, <i>et. al.</i> , 1999)	3.2 (Song, <i>et. al.</i> , 2005)	2.0 (Song, <i>et. al.</i> , 2005)
Au	5.1 (Eastman, 1970)		

*approximated value; ** recalculated value considering as reference for energy scale the vacuum level instead of normal hydrogen electrode.

The electrons injected from the $\text{SnO}_2:\text{F}/\text{TiO}_2$ front electrode recombine through deep levels in the $\text{In}(\text{OH})_x\text{S}_y$ with the holes from the $\text{Pb}(\text{OH})_x\text{S}_y$ valence band. Under illumination the $\text{In}(\text{OH})_x\text{S}_y$ bands become flat and the deep levels get filled, as observed earlier in light soaking effects thus leading to better performance of

the eta solar cell. Therefore, in an illuminated device the recombination path shifts from $\text{In}(\text{OH})_x\text{S}_y$ into the $\text{Pb}(\text{OH})_x\text{S}_y$ layer.

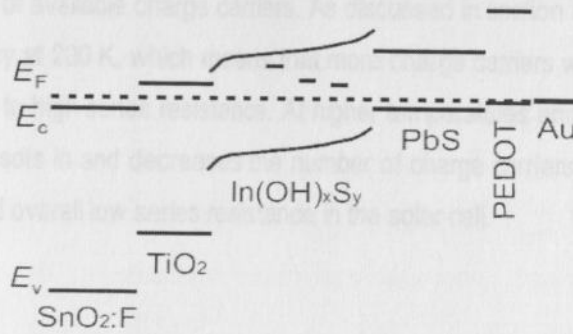


Figure 5.57: Proposed energy band diagram for the eta solar cell of the structure $\text{SnO}_2:\text{F}/\text{TiO}_2/\text{In}(\text{OH})_x\text{S}_y/\text{Pb}(\text{OH})_x\text{S}_y/\text{PEDOT}:\text{PSS}/\text{Au}$

5.5.4 Temperature dependency of series resistance R_s

The eta solar cell device was found to have high series resistant when it is operated at low temperature environment than when the temperature is raised to above the room temperature, as shown in figure 5.58.

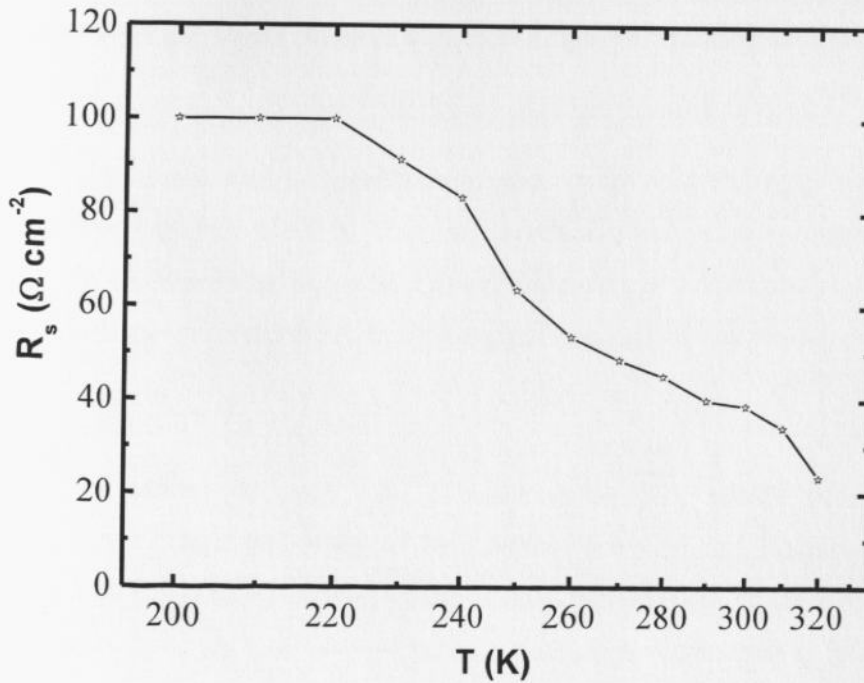


Figure 5.58: Temperature dependence of series resistance R_s of the eta solar cell.

In figure 5.58, it is seen that series resistance is approximately $100 \Omega \text{ cm}^{-2}$ for operation temperatures from 200 K to 220 K then it decays gradually as the temperature increases. The observed behaviour can be attributed to the number of available charge carriers. As discussed in section 5.5, the eta solar cell realised high conversion efficiency at 200 K, which means that more charge carriers were available in the solar cell consequently translating to high series resistance. At higher temperatures and under illumination, thermally activated recombination sets in and decreases the number of charge carriers substantially resulting in low conversion efficiency and overall low series resistance in the solar cell.

CHAPTER 6

Conclusion and suggestions for further work

6.1 Conclusions

The following conclusions can be drawn from the data analysis done in this thesis:

- Eta solar cell device of the type $\text{SnO}_2:\text{F}/\text{TiO}_2/\text{In}(\text{OH})_x\text{S}_y/\text{Pb}(\text{OH})_x\text{S}_y/\text{PEDOT}:\text{PSS}/\text{Au}$ modified with $\text{In}(\text{OH})_x\text{S}_y$ buffer layer has been successfully fabricated and characterized. The band gap energies of the materials used in fabricating the eta solar cell have been measured using surface photovoltage spectroscopy, with the following materials giving the following values: $\text{TiO}_2, E_g = 3.2$ eV, $\text{Pb}(\text{OH})_x\text{S}_y, E_g = 0.85$ eV, $\text{In}(\text{OH})_x\text{S}_y, E_g = 2.2$ eV (for samples annealed in argon atmosphere at 300°C for 30 minutes) and $E_g = 2.4$ eV (for as-prepared samples).
- The chemical bath deposited lead sulphate (PbS) has been found to be a mixed phase of $\text{PbS} + \text{PbO}$ doublet lead compounds and its chemical formula has been derived to be $\text{PbO}_k\text{S}_{1-k}$ with $k = 0.21$, nonetheless due to the presence of hydroxide ions the material has been referred to as $\text{Pb}(\text{OH})_x\text{S}_y$.
- The pH of precursor solution for chemical bath deposited $\text{In}(\text{OH})_x\text{S}_y$ has been found to influence the overall band gap of the thin films. Changes in pH value of the aqueous solution influences the content in $\text{In}(\text{OH})_x\text{S}_y$, such that higher pH values give high content of hydroxide and/ or oxide, while dominant content in sulphide is realised when deposition is done at low pH value of the chemical bath solution.
- Annealing temperature has been found to influence $\text{In}(\text{OH})_x\text{S}_y$ surface photovoltage signal amplitude, with the band gap energy of the material decreasing with increasing temperature, whereas thickness has barely no noticeable influence observable on its variation. The changes observed in the band gap have been attributed to changes in stoichiometry of the $\text{In}(\text{OH})_x\text{S}_y$ thin films.

- This work realised the first eta solar cell to be fabricated with the thinnest absorber material of approximately 10 nm. The best eta solar cell device measured using solar simulator calibrated to 1 sun = 100 mW/cm² at AM 1.5 illumination has been found to give conversion efficiency of approximately 0.83% which is good performance in comparison to other eta solar cell devices so far fabricated with thickness of the absorber material in the regimes of approximately 10 nm.
- The Pb(OH)_xS_y absorber has been found to have no significant contribution to external quantum efficiency, implying that In(OH)_xS_y/Pb(OH)_xS_y interface may be contributing to photovoltaic action of the eta solar cell and the devices with simplified structures.
- Light soaking has been found to influence some of the photovoltaic parameters of the eta solar cell and those of devices with simplified architecture. The overall conversion efficiency and short circuit current density of the solar cells have been found to increase with light soaking duration by a factor of about 1.6 – 2.7 and 2.1 – 3, respectively. The increase in these two parameters has been ascribed to filling up of trap states and/or charge – discharge of deep levels found in In(OH)_xS_y. The fill factor and open circuit voltage are unaffected by these changes.
- Different layer component materials in the eta solar cell have been found to play different specific roles: TiO₂ highly structured porous surface has been found to provide increased surface area resulting into improved optoelectrical properties of the complete eta cell structure, and also provides good interface at SnO₂:F/In(OH)_xS_y consequently reducing recombination process. The In(OH)_xS_y acts as the buffer layer of the eta solar cell and thus mitigates the recombination process of the charge carriers, also the buffer layer forms a good interface between In(OH)_xS_y/Pb(OH)_xS_y which contributes to the external quantum efficiency of the solar cell and hence contributing to the photovoltaic action of the devices. The polymer materials, PEDOT:PSS acts as a protective layer of the Pb(OH)_xS_y against diffusion effects of the Au back contact thus mitigating the effects of recombination of the charge carriers through minimised trap states.
- The ideality factor of the eta solar cell, from the studies of the transport mechanism, shows that the recombination of the charge carriers occurs through exponentially distributed energy recombination levels. Under illumination and high temperature (approximately 320 K) recombination process

occurs through shallow levels, while at low temperatures deep levels are involved in the recombination process.

- The type of recombination mechanism the solar cell undergoes is thermally activated in the bulk of the absorber material when the solar cell is under illumination, whereas in the dark, the recombination mechanism is different and the solar cell undergoes tunneling enhanced recombination.
- Work functions of $\text{SnO}_2:\text{F}$, TiO_2 , $\text{In}(\text{OH})_x\text{S}_y$, $\text{Pb}(\text{OH})_x\text{S}_y$, PEDOT:PSS and Au have been calculated from literature work and typical band diagram of the eta solar cell has been proposed to corroborate the observations of the transport mechanism.
- The $\text{JU} - \text{T}$ operation temperature has been observed to influence the series resistance in the solar cell, such that, at low temperature, the series resistance is very high and then it decreases with the increasing temperature. This behaviour has been attributed to the number of available charge carriers in the device which decreases with increasing operation temperature due to the onset of thermally activated recombination mechanism.

6.2 Suggestions for further work

There is need for further work for both fundamental and technological improvement of the solar cell in the following areas:

1. Capacitance – Voltage (C - V) spectroscopy: The C - V measurements studies may lead to clarification of the actual absorber material in the devices fabricated. The external quantum efficiency measurements revealed that $\text{Pb}(\text{OH})_x\text{S}_y$ was not contributing to EQE signal of the solar cell, leading to the allusion that interface at $\text{In}(\text{OH})_x\text{S}_y/\text{Pb}(\text{OH})_x\text{S}_y$ contributes to the photovoltaic action of the eta solar cell. This clarification will be important to the definition of eta solar cell.
2. Different window layer material for example ZnO combined with a different absorber layer such as In_2S_3 : Properties such charge mobilities, the influence of work function of the window layer and the

substrate material, as well as band gap of the absorber material can have great influence on photovoltaic performance of the fabricated device. We therefore suggest use of a working solar cell structure like the one studied in this work and replacing either window or absorber material, this may lead to realization of solar cell with higher conversion efficiency.

3. Charge carrier lifetime: The charge carrier lifetime studies may reveal more on the charge movement and buttress transport mechanism studies already done. This fundamental study can answer the question of the low conversion efficiency observed in the devices fabricated.
4. Research further on the material responsible for improved performance on light soaking.

References

- Bai, Y., Y. Cao, J. Zhang, M. Wang, R. Li, P. Wang, S.M. Zakeeruddin, M. Graetzel (2008). High performance dye sensitized solar cells on solvent free electrolytes produced from eutectic melts, *Nature Materials*, 7(8), 626 – 630.
- Barreau, N., S. Marsillac, J.C. Bernede, L. Assmann (2003). Evolution of the band structure of β - In_2S_3 - $_{3x}\text{O}_{3x}$ buffer layer with its Oxygen content, *Journal of Applied Physics*, 93 (9), 5456 – 5459.
- Bayhan, H (2006). Tunneling Enhanced Recombination in Polycrystalline CdS/CdTe Solar Cells, *Turk Journal of Physics*, 30, 109 – 114.
- Bayhan, H and A.S. Kavasoglu (2005). Tunneling enhanced recombination in polycrystalline CdS/ CdTe and CdS/ Cu(In,Ga)Se₂ heterojunction solar cells, *Solid State Electronics*, 49, 991 – 996.
- Bayon, R and J. Herrero (2000). Structure and morphology of the indium hydroxy sulphide thin films, *Applied Surface Science*, 158 (1 – 2), 49 – 57.
- Bayon, R., C. Guillen, M.A. Martinez, M.T. Gutierrez and J. Herrero (1998). Preparation of Indium hydroxyl sulphide $\text{In}(\text{OH})_x\text{S}_y$ by chemical bath deposition, *Journal of the Electrochemical Society*, 145 (8), 2775 – 2779.
- Bayon, R., C. Maffiotte, J. Herrero (1999). Chemical bath deposition of indium hydroxyl sulphide thin films: process and XPS characterization, *Thin Solid Films*, 353 (1 – 2), 100 – 107.
- Bayon, R., M. Hernandez-Mayoral and J. Herrero (2002). Growth mechanism of CBD- $\text{In}(\text{OH})_x\text{S}_y$ thin films, *Journal of the Electrochemical Society*, 149 (1), C59 – C67.
- Bayon, R., R. Musembi, A. Belaidi, M. Bär, T. Guminskaya, Ch-H. Fischer, M. Ch. Lux-Steiner, Th. Dittrich (2006). Highly structured $\text{TiO}_2/\text{In}(\text{OH})_x\text{S}_y/\text{PbS}/\text{PEDOT}:\text{PSS}$ to be used in photovoltaic applications, *C.R. Chimie*, 9, 730 – 734.

- Bayon, R., R. Musembi, A. Belaidi, M. Bär, T. Guminskaya, M.Ch. Lux-Steiner, Th. Dittrich (2005). Highly structured $\text{TiO}_2/\text{In}(\text{OH})_x\text{S}_y/\text{PbS}/\text{PEDOT:PSS}$ for photovoltaic applications, *Solar Energy Materials and Solar Cells*, **89**, 13 – 25.
- Belaidi, A (2004). Scanning Electron Micrograph for TiO_2 , Private communication.
- Belaidi, A., R. Bayon, L. Dloczik, K. Ernst, M.Ch. Lux-Steiner, R. Könenkamp (2003). Comparison of different thin film absorbers used in eta solar cells, *Thin Solid Films*, **431 – 432**, 488 – 491.
- Brown, T.M., J.S. Kim, R.H. Friend, F. Cacialli, R. Daik, W.J. Feast (1999). Built-in field electroabsorption spectroscopy of polymer light emitting diodes incorporating doped poly(3,4-ethylene dioxothiophene) hole injection layer, *Applied Physics Letter*, **75**(12), 1679 – 1683.
- Chapin, D.M., C.S. Fuller, G.L. Pearson (1954). A New Silicon p – n Junction photocell for Converting Solar Radiation into Electrical Power, *Journal of Applied Physics*, **25** (5), 676.
- Chiba, Y., A. Islam, Y. Watanabe, R. Komiya, N. Koide, L. Han (2006). Dye Sensitized Solar Cells with Conversion Efficiency of 11.1%, *Japanese Journal of Applied Physics*, **45**, L638 – L640.
- Cooke, M.J (1990). *Semiconductor Devices*, Prentice Hall, London, 83 – 106.
- Duzhko, V (2002). *Photovoltage phenomena in nanoscale materials*, Munich Technical University, Munich, Germany.
- Eastman, D.E (1970). Photoelectric work function of transition, rare earth and noble metals, *Physical Review*, **B2** (1), 1 – 2.
- Ei-Tachi, M., A. Khoury, M.D. Labardonnie, P. Mialhe, F. Pelancon (2000). Degradation of the diode ideality factor of silicon n-p junction, *Solar Energy Materials and Solar Cell*, **62**, 393 – 398.

- Ernst, K., A. Belaidi, R. Könenkamp** (2003). Solar cell with extremely thin absorber on highly structured substrate, *Semiconductor Science and Technology*, **18**, 475 – 479.
- Ernst, K., I. Sieber, M. Neumann-Spallart, M.Ch. Lux-Steiner, R. Könenkamp**, (2000). Characterization of II-VI compounds on porous substrates, *Thin Solid Films*, **361 -362**, 213 – 217.
- Ernst, K., R. Engelhardt, K. Ellmer, C. Kelch, H. J. Muffler, M. Ch. Lux-Steiner, R. Könenkamp** (2001). Contacts to a solar cell with extremely thin CdTe absorber, *Thin Solid Films*, **387**, 26 – 28.
- Fahrenbruch, A.L., and R.H. Bube** (1983). *Fundamentals of Solar Cells: Photovoltaic Solar Energy Conversion*, Academic Press, New York.
- Fritsche, J., D. Kraft, A. Thissen, T. Meyer, A. Klein, A. Jaegermann** (2002). Band energy diagram of CdTe thin films solar cells, *Thin Solid Films*, **403 – 404**, 252 – 257.
- Fuertes - Marron, D** (2003). *Structural and electrical characterization of thin film solar cells based on CVD-grown CuGaSe₂*, Freie Universität, Berlin, Germany.
- Gavrilov, S., I. Oja, B. Lim, A. Belaidi, W. Bohne, E. Strub, J. Röhrich, M. Ch. Lux-Steiner and Th. Dittrich** (2006). Charge selective contact on ultra-thin In(OH)_xS_y/Pb(OH)_xS_y heterostructure prepared by SILAR, *Physica Status Solidi (a)*, **203** (5), 1024 – 1029.
- Granqvist, C.G** (1991). In "Introduction to Material Science for the Solar Energy Conversion Systems", Edited by C.G. Granqvist, Material Science for Solar Energy Conversion Systems, Pergamon Press, Oxford.
- Grasso, C., and M. Burgelman** (2004). Theoretical study on the effect of an intermediate layer in CIS based ETA solar cells, *Thin Solid Films*, **451 – 452**, 156 – 159.
- Grätzel, M** (2001). Photoelectrochemical cells, *Nature*, **414**, 338 – 344.

- Green, M.A.**, (1992). *Solar Cells: Operating Principles, Technology and System Applications*, The University of South Wales, Kensington, 62 – 204.
- Groenendal, B.L., F. Jonas, D.Freitag, H. Pielartzik, J.R. Reynolds** (2000). Poly(3,4-ethylenedioxythiophene) and its derivatives: past, present and future, *Advanced Materials*, **12** (7), 481 – 494.
- Groetzberger, A., C. Hebling, H.W. Schock** (2003). Photovoltaic materials, history, status and outlook, *Material Science and Engineering*, **R40**, 1 – 40.
- Hall, R.N** (1952). Electron – Hole Recombination Germanium, *American Physical Review*, **87**, 387 – 387.
- Huang, J., P.F. Miller, J.C. de Mello, A.J. de Mello, D.D.C. Bradley** (2003). Influence of thermal treatment on the conductivity and morphology of PEDOT:PSS films, *Synthetic Metals* **139**, 569 – 572.
- Hurkx,G.A.M., D.B.M. Klaasen, and M.P.G. Knuvers** (1992). A New Recombination Model for Device Simulation Including Tunneling, *IEEE Transactions on Electron Devices*, **39** (2), 331 – 338.
- Jönsson, S.K.M., J. Birgersson, X. Crispin, G. Greczynski, W. Osikowicz, A.W. Denier van der Gon, W.R. Salaneck, M. Fahlman** (2003). The effects of solvents on the morphology and sheet resistance in poly(3,4-ethylenedioxythiophene-polystyrenesulfonic acid (PEDOT-PSS) films, *Synthetic Metals*, **10361**, 1 – 10.
- Kaiser, I, K. Ernst, C.H. Fischer, R. Könenkamp, C. Rost, I. Sieber, M.Ch. Lux-Steiner** (2001). The eta solar cell with CuInS_2 : A photovoltaic cell concept using an extremely thin absorber (eta), *Solar Energy Materials and Solar Cells*, **67**, 89 – 96.
- Kaufmann, C.A** (2002). *Chemical Bath Deposition of Thin Semiconductor Films for Use as Buffer Layers in CuInS_2 Thin Film Solar Cells*, PhD Thesis, The Queen's College, University of Oxford, UK.

- Kaufmann, C.A., R. Bayon, W. Bohne, J. Röhrich, R. Klenk, and P.J. Dobson** (2002). Chemical Bath Deposition of Indium Oxyhydroxysulphide Thin Films, *Journal of Electrochemical Society*, **149** (1), C1 – C9.
- Kazmerski, L.L** (1997). Photovoltaic: A review of cell and module technologies, *Renewable and Sustainable Energy Reviews*, **1** (1-2), 71 – 170.
- Kim, K.S., T.J. O'Leary, N. Winograd** (1973). X-ray photoelectron spectra of Lead oxides, *Analytical Chemistry*, **45**, 2214 – 2218.
- Kittel, C** (1996). *Introduction to solid state physics*, 7th Edition, Wiley and sons, New York.
- Könenkamp, R., and P. Hoyer** (1995). Photoconduction in porous TiO₂ sensitized by PbS quantum dots, *Applied Physics Letter*, **66** (3), 349 – 351.
- Könenkamp, R., L.Dloczik, K. Ernst, C. Olesch** (2002). Nano-Structure for solar cells with extremely thin absorber, *Physica*, **E 14**, 219 – 223.
- Krunks, M., A. Katerski, T. Dedova, I. Oja Acik, and A. Mere** (2008). Nanostructured solar cell based on spray pyrolysis deposited ZnO nanorod array, *Solar Energy Materials and Solar Cells*, **92**, 1016 – 1019.
- Kumara, G.R.A., S. Kaneko, M. Okuya, K. Tennakone** (2002). Fabrication of dye-sensitized solar cells using triethylamine hydrothiocyanate as CuI crystal growth inhibitor, *Langmuir*, **18** (26), 10493 – 10495.
- Larramona, G., C. Chone, A. Jacob, D. Sakakura, B. Delatouche, D. Pere, X. Cieren, M. Nagino, and R. Bayon** (2006). Nanostructured Photovoltaic Cell of the Type Titanium Dioxide, Cadmium Sulfide Thin Coating, and Copper Thiocyanate Showing High quantum Efficiency, *Chem. Materials*, **18**, 1688 – 1696.
- Lenzmann, F., B. O'Regan, J. Wienke, C. Huisman, L. Reijnen, A. Goossens**, (2002). Surface photovoltage measurements: a useful tool for the detection of electron injection process in extremely thin absorber (ETA) solar cells, *Physica E*, **14**, 233 – 236.

- Lenzmann, F., M. Nanu, O. Kijatkina, A. Belaidi** (2004). Substantial improvement of the photovoltaic characteristics of $\text{TiO}_2/\text{CuInS}_2$ interfaces by the use of recombination barrier coatings, *Thin Solid Films*, **451** – **452**, 639 – 643.
- Levy-Clement, C., A. Katty, S. Bastide, F. Zenia, I. Mora, V. Munoz-Sanjose** (2002). A new CdTe/ZnO columnar composite film for Eta solar cells, *Physica E*, **14**, 229 – 232.
- Levy-Clement, C., R. Tena-Zaera, M. A. Ryan, A. Katty, and G. Hodes** (2005). CdSe-Sensitized p-CuSCN/Nanowire n-ZnO Heterojunction, *Advanced Materials*, **17**, 1512 – 1515.
- Luque, A and A. Marti** (1997). Increasing the efficiency of ideal solar cell by photon induced transitions at intermediate levels, *Physical Review Letter*, **78** (26), 5014 – 5017.
- Mane, R.S. and C.D. Lokhande** (2000). Chemical deposition method for metal chalcogenide thin films, *Material Chemistry and Physics*, **65**, 1 – 31.
- Matsumoto, M., H. Miyazaki, K. Matsuhira, Y. Kumashiro, Y. Takaoka** (1996). A dye sensitized TiO_2 photoelectrochemical cell constructed with polymer solid electrolyte, *Solid State Ionics*, **89** (3-4) 263 – 267.
- Murakoshi, K., R. Kogure, Y. Wada, S. Yanagida** (1998). Fabrication of solid state dye sensitized TiO_2 solar cells combined with polypyrrole, *Solar Energy Materials and Solar Cells*, **55** (1 - 2) 113 – 125.
- Musembi, R., M. Rusu, J.M. Mwabora, B.O. Aduda, K. Fostiropoulos, M.Ch. Lux_Steiner** (2008). Intensity and temperature characterization of eta solar cell, *Physica Status Solidi (a)*, **205** (7), 1713 – 1718.
- Nadenau, V., U. Rau, A. Jasenek, H.W. Schock** (2000). Electronic properties of CuGaSe_2 based heterojunction solar cells: Part I Transport Analysis, *Journal of Applied Physics*, **87**(1), 584 – 593.
- Nelson, J** (2003). *The Physics of Solar Cells*, World Scientific Publishing Co. Imperial College, Uk.

- O'Hayre, R., M. Nanu, J. Schoonman, A. Goosens (2007). A parametric study of $\text{TiO}_2/\text{CuInS}_2$ nanocomposite solar cells: how cell thickness, buffer layer thickness, and TiO_2 particle size affect performance, *Nanotechnology*, **18**, 1 – 7.
- O'Regan, B and M. Gratzel (1991). A low cost high efficiency solar cell based on dye sensitized colloidal TiO_2 films, *Nature*, **335**, 737.
- Oja, I., A. Belaidi, L. Dloczik, M.Ch. Lux-Steiner and Th. Dittrich (2006). Photoelectrical properties of $\text{In}(\text{OH})_x\text{S}_y/\text{PbS}(\text{O})$ structures deposited by SILAR on TiO_2 , *Semiconductor Science and Technology*, **21**, 520 – 526.
- Overstraeten von R.J and R. J. Mertens (1986). *Technology and use of the Photovoltaic*, Adam Hilger Ltd, Bristol and Boston.
- Pederson, L.R (1982). Two dimensional chemical state plot for lead using XPS, *Journal of Electron Spectroscopy and Related Phenomena*, **28**, 203 – 209.
- Peng, B., G. Jungmann, C. Jäger, D. Haarer, H-W. Schmidt and M. Thelakkat (2004). Systematic investigation of the role of compact TiO_2 layer in solid state dye-sensitized TiO_2 solar cells, *Coordination Chemistry Reviews*, **248** (13 - 14), 1479 – 1498.
- Quasching, V (2005). *Understanding Renewable Energy Systems*, Earthscan, London, 1 – 130.
- Rau, U and H.W. Schock (1999). Electronic properties of $\text{Cu}(\text{In,Ga})\text{Se}_2$ heteronjunction solar cells- recent achievements, current understanding, and future challenges, *Thin Solid Films*, **69** (2), 131 – 147.
- Rau, U., A. Jasenek, H.W. Schock, F. Engelhardt, Th. Meyer (2000). Electronic loss mechanisms in chalcopyrite based heteronjunction solar cells, *Thin Solid Films*, **361 – 362**, 298 – 302.
- Reiss, J (2002). *Generation und Rekombination von Ladungsträgern in CuInS_2 – basierten Dünnschicht – Solarzellen*, PhD thesis, Freie Universität, Berlin, Germany.

- Rusu, M., W. Eisele, R. Würz, A. Ennaoui, M. Ch. Lux – Steiner, T.P. Niesen, F. Karg (2003). Current transport in ZnO/ZnS/Cu(In,Ga)(S,Se)₂ solar cell, *Journal of Physics and Chemistry of Solids* **64**, 2037 – 2040.
- Rusu, M., S. Sadewasser, Th. Glatzel, P. Gashin, A. Simashkevich, A. Jäger-Waldau (2002). Contribution of the ZnSe/CuGaSe₂ heterojunction in photovoltaic performance of chalcopyrite based solar cells, *Thin Solid Films*, **403 – 404**, 344 – 348.
- Schilinsky, P., C. Waldauf, J. Hauch, C.J. Brabec (2004). Simulation of light intensity dependent current characteristics of polymer solar cell, *Journal of Applied Physics*, **95**(5), 2816 – 2820.
- Schmela, M (2003). Nothing goes without solar, Photon International, The photovoltaic magazine, Solar Verlag, Germany, **5**, 3.
- Schuller, S (2002). *Transporteigenschaften und Defecte in Polykristallinen CuGaSe₂-Schichten und Heterostrukturen*, PhD thesis, Freie Universität, Berlin, Germany.
- Sg – Lux (2004). Titanium dioxide thin films deposited by sol – gel technique, purchased from Sg – Lux, GmbH, Germany.
- Sharma, G.D., J.K. Sharma, M.S. Roy (2006). Charge generation and photovoltaic properties of hybrid solar cells based on ZnO and Copper Phthalocyanines (CuPc), *Solar Energy Materials and Solar Cells*, **90**(7 – 8), 932 – 943.
- Shockley, W. and W.T. Read Jr (1952). Statistics of the Recombination of Holes and Electrons, *Physical Review*, **87** (5), 835 – 842.
- Siebentritt, S. K. Ernst, Ch. Fischer, R. Konenkamp (1997). CdTe and CdS as extremely thin absorber material in an eta solar cell, 14th European photovoltaic solar energy conference, Barcelona, Spain, 1823.

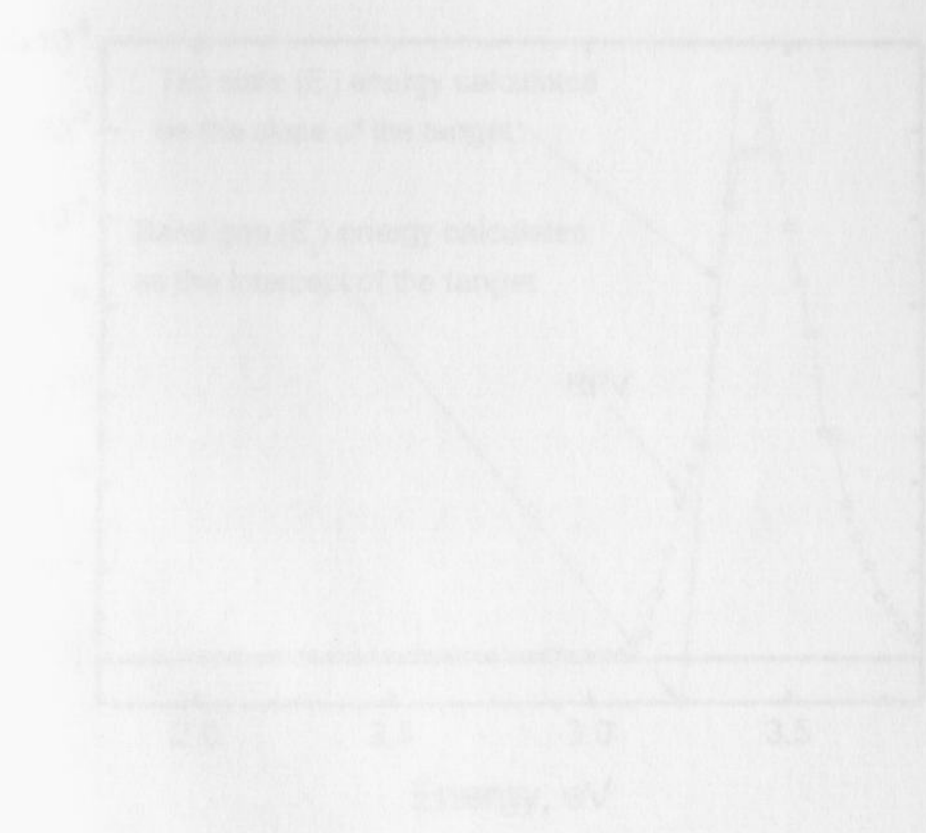
- Song, M.Y., K.J. Kim and D.Y. Kim** (2005). Enhancement of photovoltaic characteristics using a PEDOT interlayer in TiO₂/MEHPPV heterojunction devices, *Solar Energy Materials and Solar Cells*, **85** (1), 31 – 39.
- Streetman, B.G** (1993). *Solid State Electronic Devices*, Prentice Hall of India, New Delhi, India.
- Sze, S.M** (1997). *Physics of Semiconductor Devices*, Wiley – Interscience, New York, 790 – 839.
- Taretto, K., and U. Rau** (2005). Influence of built-in voltage in optimized extremely thin absorber solar cell, *Thin Solid Films*, **480 – 481**, 447 – 451.
- Tennakone, K., G.R.R.A. Kumara, I.R.M. Kottegoda, V.P.S. Perera and G.M.L.P. Aponsu** (1998). Nanoporous n – TiO₂/selenium/p-CuCNs photovoltaic cell, *Journal of Physics D: Applied Physics*, **31**, 2326 – 2330.
- Verschraegen, J., M. Burgelman, P. Penndorf** (2005). Temperature dependence of the diode ideality factor in CuInS₂ –on-Cu tape solar cells, *Thin Solid Films*, **480 – 481**, 307 – 311.
- Vogel, R., P. Hoyer, H. Weller** (1994). Quantum sized PbS, CdS, Ag₂S, Sb₂S₃ and Bi₂S₃ particles as sensitizers for various nanoporous wide-bandgap semiconductors, *Journal of Physical Chemistry*, **98** (12) 3183 – 3188.
- Wagner, C.D., D.A. Zatko, R.H. Raymond** (1980). Use of the oxygen KLL Auger lines in identification of surface chemical states by electron spectroscopy for chemical analysis, *Analytical Chemistry*, **52**, 1445 – 1451.
- Walter, T., R. Herberholz and H.W. Schock** (1996). Distribution of Defects in Polycrystalline Chalcopyrite Thin Films, *Solid State Phenomena*, **51 – 52**, 309 – 316.
- Wienke, J., M. Krunks, F. Lenzmann** (2003). In_x(OH)_yS_z as recombination barrier in TiO₂/inorganic absorber heterojunction, *Semiconductor Science and Technology*, **18**, 876 – 880.

Yanagida, S., S. Kambe, W. Kubo, K. Murakoshi, Y. Wada, T. Kitamura (1999). Structural control of porous nano space in dye sensitized TiO₂ solar cells, *Zeitschrift fuer physikalische chemie*, **212** (1) 31 – 38.

Zhang, X. T., H.W. Liu, T. Taguchi, Q.B. Meng, O. Sato, A. Fujishima (2004). Slow interfacial charge recombination in solid state dye sensitized solar cell using Al₂O₃ coated nanoporous TiO₂ films, *Solar Energy Materials and Solar Cells*, **81**, 197 – 203.

APPENDIX

Calculation of the energy gap (E_g) of a crystal from the slope of the target

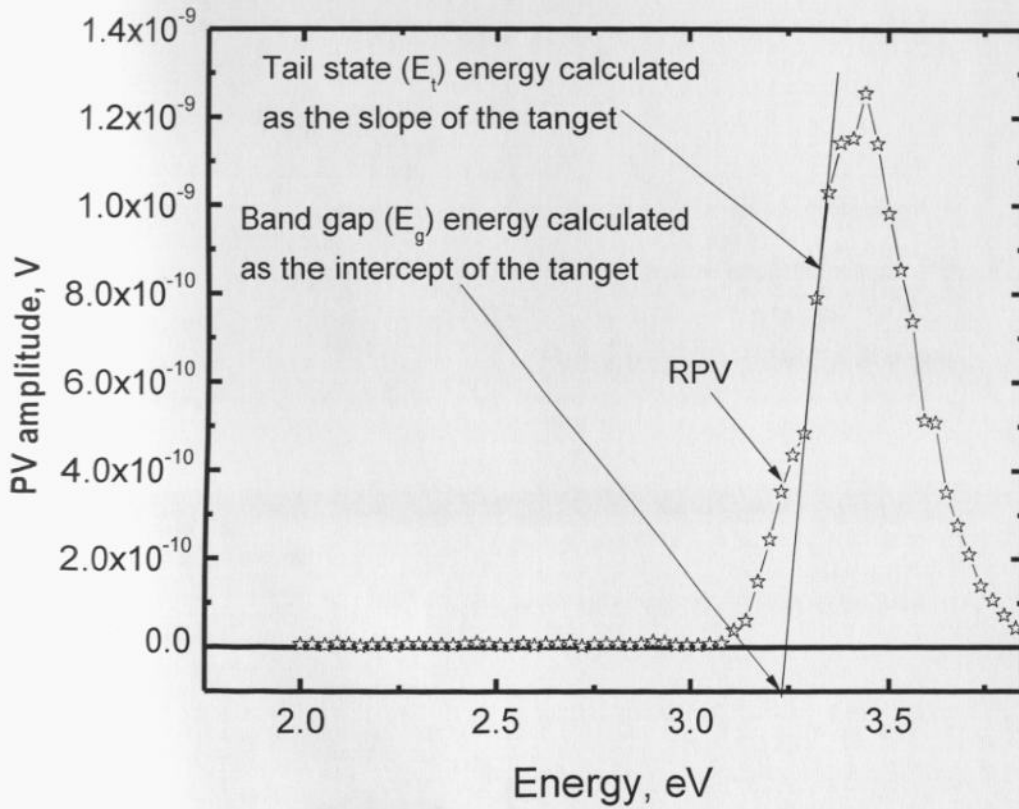


$$E_g = \sqrt{a^2 + b^2}$$

where 'a' is the intercept and 'b' is the slope of the target

APPENDIX A: CALCULATION FOR BAND GAP AND TAIL STATE ENERGY FROM SPV AMPLITUDE

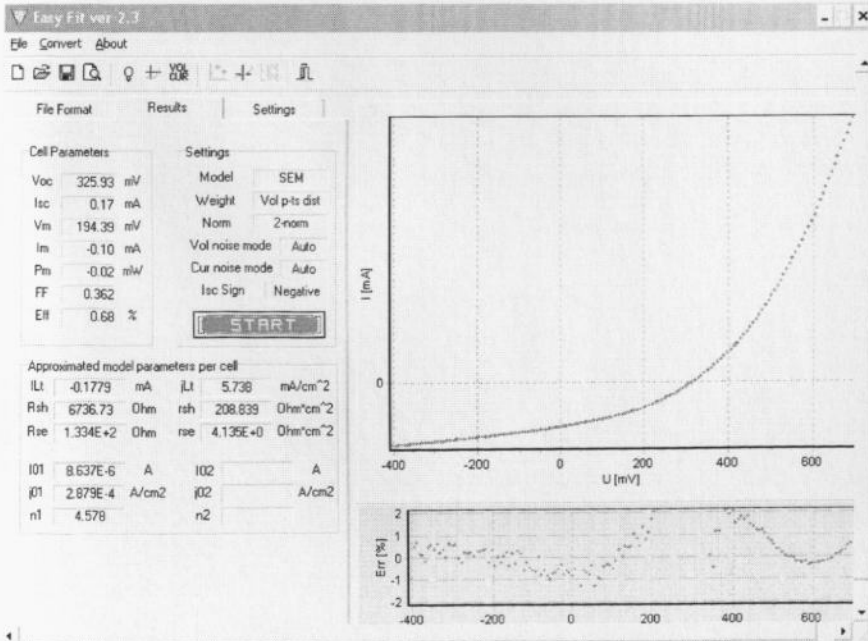
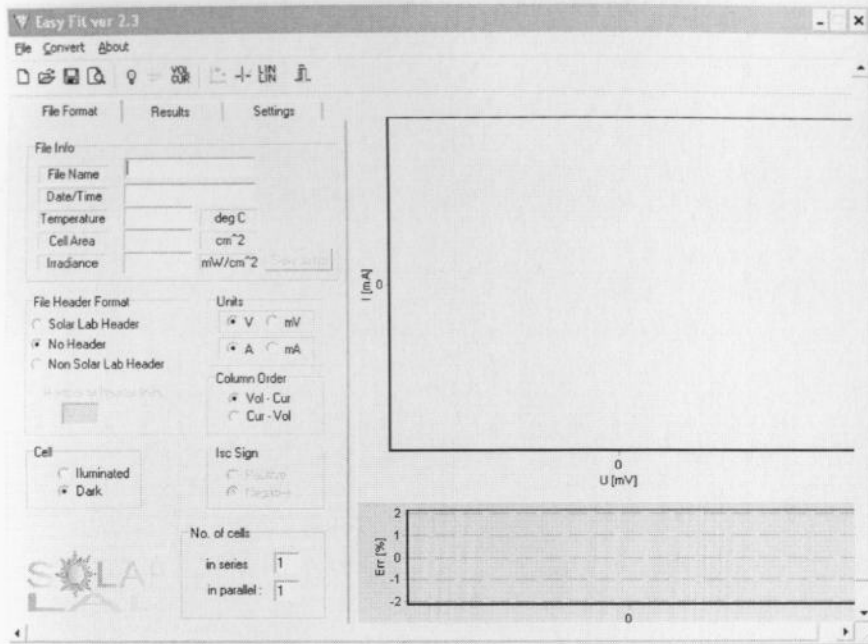
Calculation of band gap (E_g) energy and tail state (E_t) energy of a semiconductor



$$RPV = \sqrt{a^2 + b^2}$$

RPV is the resultant photovoltage where a is the in-phase and b is the 90° out of phase signals respectively.

APPENDIX B: SCREEN SHOTS FOR FITTING PROGRAM FOR PARASITIC RESISTANCE





ELSEVIER

Available online at www.sciencedirect.com

SCIENCE @ DIRECT®

Solar Energy Materials & Solar Cells 89 (2005) 13–25

Solar Energy Materials
& Solar Cells

www.elsevier.com/locate/solmat

Highly structured $\text{TiO}_2/\text{In}(\text{OH})_x\text{S}_y/\text{PbS}/$ PEDOT:PSS for photovoltaic applications

R. Bayon¹, R. Musembi, A. Belaidi, M. Bär, T. Guminskaya,
M.-Ch. Lux-Steiner, Th. Dittrich*

Hahn-Meitner-Institut, Abteilung SE2, Glienicker Str. 100, D-14109 Berlin, Germany

Received 9 July 2004; accepted 20 November 2004

Available online 18 January 2005

Abstract

A system of highly structured $\text{TiO}_2/\text{In}(\text{OH})_x\text{S}_y/\text{PbS}/\text{PEDOT:PSS}$ has been developed and investigated by photovoltage spectroscopy, X-ray photo- and Auger electron spectroscopies, electron microscopy, and photovoltaic response. TiO_2 , $\text{In}(\text{OH})_x\text{S}_y$, PbS, and PEDOT:PSS serve as electron conductor, buffer layer, absorber, and hole conductor, respectively. Both buffer and absorber layers were prepared by chemical bath deposition. The band gap of as-prepared $\text{In}(\text{OH})_x\text{S}_y$ varied between 2.4 and 3.5 eV depending on the pH-value of the solution. In addition, the band gap of the PbS could be widened to about 0.85 eV making the application as absorber for solar cells feasible. At present, corresponding solar cell devices reach short-circuit current densities of about 8 mA/cm^2 and open-circuit voltages of about 0.3 V.

© 2004 Elsevier B.V. All rights reserved.

Keywords: Highly structured TiO_2 ; PbS; Photovoltage spectroscopy

1. Introduction

The development of alternative photovoltaic systems and solar cell materials is important from both the fundamental and technological viewpoints. An example of

*Corresponding author. Tel.: +49 30 8062 2090; fax: +49 30 8062 3199.

E-mail address: dittrich@hmi.de (T. Dittrich).

¹Present address: IMRA-EUROPE, 220 rue Albert Caquot, Sophia-Antipolis Cedex, 06904 France.



Preliminary communication / Communication

Highly structured $\text{TiO}_2/\text{In}(\text{OH})_x\text{S}_y/\text{PbS}/\text{PEDOT:PSS}$ to be used in photovoltaic applications

Rocío Bayón*, Robinson Musembi, Abdelhak Belaidi, Marcus Bär, Tatjana Guminskaya, Christian Herbert Fischer, Martha Christina Lux-Steiner, Thomas Dittrich

Hahn-Meier-Institut, Glienicke Str. 100, D-14109 Berlin, Germany

Received 7 September 2004; accepted after revision 4 February 2005

Available online 13 September 2005

Abstract

A new highly structured system based on $\text{TiO}_2/\text{In}(\text{OH})_x\text{S}_y/\text{PbS}/\text{PEDOT:PSS}/\text{Au}$ has been developed for photovoltaic applications. In this device, TiO_2 , $\text{In}(\text{OH})_x\text{S}_y$, PbS and PEDOT:PSS serve as electron conductor, buffer layer, absorber and hole conductor, respectively. Both buffer and absorber layers have been prepared by chemical bath deposition. For annealed $\text{In}(\text{OH})_x\text{S}_y$, an optical band gap of 2.2 eV has been obtained and for PbS the bulk value is widened to about 0.85 eV due to the presence of oxide in the film composition. At present stage, solar cells with such configuration have reached up to about 1% efficiency with $J_{sc} = 8 \text{ mA/cm}^2$ and $V_{oc} = 0.3 \text{ V}$. **To cite this article:** R. Bayón et al., C. R. Chimie 9 (2006).

© 2005 Académie des sciences. Published by Elsevier SAS. All rights reserved.

Résumé

Une nouvelle cellule photovoltaïque fondée sur le système ultra-structuré $\text{TiO}_2/\text{In}(\text{OH})_x\text{S}_y/\text{PbS}/\text{PEDOT:PSS}/\text{Au}$ a été développée. Dans ce dispositif TiO_2 , $\text{In}(\text{OH})_x\text{S}_y$, PbS et PEDOT:PSS servent de conducteur d'électrons, couche tampon, absorbeur et conducteur de trous respectivement. La couche tampon ainsi que celle d'absorbeur ont été préparées par dépôt chimique en solution. Pour les couches de $\text{In}(\text{OH})_x\text{S}_y$ recuites, une énergie de gap de 2.2 eV a été obtenue et, pour celle de PbS, la valeur correspondant au matériau massif a atteint 0.85 eV, en raison de la présence d'oxyde dans la composition de la couche. À présent, les cellules photovoltaïques de cette configuration ont atteint presque 1% de rendement de conversion ($J_{sc} = 8 \text{ mA/cm}^2$ et $V_{oc} = 0.3 \text{ V}$). **Pour citer cet article :** R. Bayón et al., C. R. Chimie 9 (2006).

© 2005 Académie des sciences. Published by Elsevier SAS. All rights reserved.

Keywords: Highly structured TiO_2 ; $\text{In}(\text{OH})_x\text{S}_y$; PbS; PEDOT:PSS; Photovoltage spectroscopy

Mots clés : TiO_2 très structuré ; $\text{In}(\text{OH})_x\text{S}_y$; PbS ; PEDOT : PSS ; Spectroscopie de photovoltage

* Corresponding author: Ciemat, Division de Energías Renovables, Avenida Complutense 22, 28040 Madrid, Spain.

E-mail address: rocio.bayon@ciemat.es (R. Bayón).

Intensity and temperature dependent characterization of eta solar cell

Robinson J. Musembi¹, Marin Rusu², Julius M. Mwabora¹, Bernard O. Aduda¹,
Konstantinos Fostiropoulos², and Martha Ch. Lux-Steiner²

¹ Department of Physics, School of Physical Sciences, University of Nairobi, P.O. Box 30197, 00100 Nairobi, Kenya

² Hahn-Meitner Institute, Glienicker Straße 100, 14109 Berlin, Germany

Received 27 September 2007, revised 2 April 2008, accepted 9 May 2008

Published online 19 June 2008

PACS 73.40.Ei, 73.40.Lq, 73.50.Gr, 73.50.Pz, 84.60.Jt

Temperature-dependent electrical characterization of a highly structured $\text{TiO}_2/\text{In}(\text{OH})_x\text{S}_y/\text{Pb}(\text{OH})_x\text{S}_y/\text{PEDOT}:\text{PSS}$ eta solar cell has been carried out. The transport mechanism in this type of solar cell has been investigated. A schematic energy band diagram which explains the photoelectrical properties of the device has been proposed. The solar cell has been characterized in the temperature range 200–320 K at illumination intensities between 0.05 mW/cm^2 and 100 mW/cm^2 . The diode ideality factor A under illumination has been found to vary

between 1.2 and 1.6, whereas in the dark $6.9 \leq A \leq 10.1$. The device has been found to undergo a thermally activated recombination under illumination, while tunnelling enhanced recombination has been established to dominate the current in the dark. The solar cell efficiency shows a logarithmic dependence on illumination in the whole temperature range investigated, achieving its maximum at an illumination of $\sim 45 \text{ mW}/\text{cm}^2$.

Phys. Status Solidi (a) 205, No. 7, 1713–1718 (2008) / DOI 10.1002/pssa.200723466

SOLAR CELL WITH $\text{Pb}(\text{OH})_x\text{S}_y$ EXTREMELY THIN ABSORBER (ETA) BASED ON NOVEL ETA CONCEPT

R.J. Musembi¹, B.O. Aduda¹, J.M. Mwabora¹, R. Bayon²

¹Department of Physics, School of Physical Sciences, University of Nairobi,
P.O. Box 30197 – 00100 Nairobi Kenya

²Ciemat, Division de Energias Renovables, Avenida Complutense 22, 28040 Madrid, Spain

ABSTRACT: A new highly structured $\text{In}(\text{OH})_x\text{S}_y/\text{Pb}(\text{OH})_x\text{S}_y/\text{PEDOT:PSS}$ solar cell has been developed based on the novel eta concept, and characterized by photovoltage spectroscopy, X-ray photoelectron spectroscopy, scanning electron spectroscopy, photovoltaic response and quantum efficiency spectroscopy. In this system, $\text{In}(\text{OH})_x\text{S}_y$, PbS and PEDOT:PSS serve as electron conductor, light photon absorber material and hole conductor respectively. The electron conductor and absorber layer were prepared by chemical bath deposition, while the hole conductor was prepared by spin coating technique. The band gap of as prepared $\text{In}(\text{OH})_x\text{S}_y$ has been found to vary with pH of the solution; furthermore the bandgap of $\text{Pb}(\text{OH})_x\text{S}_y$ can be engineered to make it suitable as absorber material. At present, a solar cell device has been realized with efficiency up to over 1%, $J_{sc} = 11.7 \text{ mA/cm}^2$ and $V_{oc} = 3.0 \text{ V}$.

INTRODUCTION

One of the most important intentions in photovoltaic research is to reduce the cost of solar cell production. The concept of extremely thin absorber (eta) solar cells is closely related to the concept of dye sensitized solar cell. In eta solar cell, an extremely thin layer of absorber material is sandwiched between two wide bandgap materials, one n-type and the other p-type, thus the process of light absorption followed by charge separation and carrier transport are separated in space, similar to dye sensitized solar cells [1 - 3]. In this paper we report a new type of solar cell based on novel eta concept with planar structure of $\text{SnO}_2:\text{F}/\text{In}(\text{OH})_x\text{S}_y/\text{Pb}(\text{OH})_x\text{S}_y/\text{PEDOT:PSS}$ with overall thickness of approximately 100 nm. In this solar cell, Indium hydroxyl sulphide, $\text{In}(\text{OH})_x\text{S}_y$, is being used as the electron conductor, lead hydroxy sulphide, $\text{Pb}(\text{OH})_x\text{S}_y$, and Poly (3,4) ethylenedioxythiophene doped with polystyrene sulfonic acid, PEDOT:PSS are used as the light photon absorber and hole conductor respectively.

In this study the thin films of $\text{In}(\text{OH})_x\text{S}_y$ and $\text{Pb}(\text{OH})_x\text{S}_y$ were characterized by scanning electron microscopy, spectral surface photovoltage and X-ray photoelectron spectroscopy in order to get insight on surface and structural morphology and the layers composition. Current

- voltage (I - V) and quantum efficiency analyses were also done to provide understanding of the performance of the solar cells.

EXPERIMENTS

The samples were fabricated on TEC 15 $\text{SnO}_2:\text{F}$ (Pilkington) glass. Thin films of indium hydroxyl sulphide and lead sulphide were deposited by chemical bath deposition using the following methods: $\text{In}(\text{OH})_x\text{S}_y$ was prepared using the following precursor materials, 0.025 M InCl_3 , 0.1 M thioacetamide (TA), and varying concentration of hydrochloric acid (HCL) at GmbH by spin coating technique.

The surface morphology of the sample was studied using Carl Zeiss Leo 1540 scanning electron microscopy, while X-ray photoelectron spectroscopy analysis was done using VG CLAM 4 electron spectrometer. The surface photovoltage study was done using a parallel plate capacitor arrangement with illumination provided by a 250 W halogen lamp. The current - voltage characterization both in the dark and under illumination were performed at room temperature using a Keithley 237 high voltage source meter, and a halogen lamp from General Electric calibrated to give 100 mW/cm^2 was used as source of illumination.

Light soaking induced increase in efficiency in solar cells based on $\text{In}(\text{OH})_x\text{S}_y/\text{Pb}(\text{OH})_x\text{S}_y$

R J Musembi¹, B O Aduda¹, J M Mwabora¹, M Rusu², K Fostiropoulos², M Ch Lux-Steiner²

¹Department of Physics, School of Physical Sciences, University of Nairobi, P.O. Box 30197, 00100 Nairobi, Kenya

²Solarenergieforschung (SE2), Lise-Meitner Campus, Hermholtz-Zentrum Berlin für Materialien und Energie, Glienicker Strasse 100, D-14109 Berlin, Germany

PACS 73.40.Ei, 73.40.Lq, 73.50.Gr, 73.50.Pz, 84.60.Jt

Email: musembirj@uonbi.ac.ke

Abstract

Light soaking characterization on complete $\text{SnO}_2:\text{F}/\text{TiO}_2/\text{In}(\text{OH})_x\text{S}_y/\text{Pb}(\text{OH})_x\text{S}_y/\text{PEDOT}:\text{PSS}/\text{Au}$, eta solar cell structure as well as on devices which do not include one or both TiO_2 and/ or $\text{PEDOT}:\text{PSS}$ layers has been conducted. Additionally, studies of $\text{SnO}_2:\text{F}/\text{In}(\text{OH})_x\text{S}_y/\text{Pb}(\text{OH})_x\text{S}_y/\text{PEDOT}:\text{PSS}/\text{Au}$ solar cell have been performed. The power conversion efficiency and the short circuit current density have been found to increase with light soaking duration by a factor of about 1.6 - 2.7 and 2.1 - 3 respectively. The increase in these two parameters has been attributed to filling up of trap states and / or charge – discharge of deep levels found in $\text{In}(\text{OH})_x\text{S}_y$. These effects take place at almost fill factor and open circuit voltage being unaffected by the light soaking effects.

Keywords: eta solar cell, TiO_2 , $\text{Pb}(\text{OH})_x\text{S}_y$, $\text{In}(\text{OH})_x\text{S}_y$, light soaking

=====
Submitted: Semiconductor Science and
Technology Journal, Institute of Physics, UK.

UNIVERSITY OF NAIROBI
LIBRARY